A STEP TOWARDS INTEGRATED SAFETY SIMULATION THROUGH PRE-CRASH TO IN-CRASH DATA TRANSFER

Abdulkadir Öztürk
Christian Mayer
Daimler AG
Germany

Hemanth Kumar G
Pronoy Ghosh
Atul Mishra
Ravi Kiran Chitteti
Mercedes-Benz Research and Development India Pvt. Ltd
India

Dirk Fressmann
DYNAmore GmbH
Germany

Paper Number 19-0257

ABSTRACT

Occupant simulation methods in the area of passive safety address usually the investigation and prediction of crash dummy behavior after the time of collision. The development and optimization of active and also pre-triggered passive safety systems [1] require new simulation methodology including improved occupant models [2][3] and data transfer possibility between pre-crash and crash phase of a crash event. Prediction of occupant behavior in the pre-crash phase is one important enabler for such a new occupant simulation methodology dealing with optimization of integrated safety systems.

In this work, a semi-automated method is developed for posture and velocity data transfer between pre-crash Active Human Body Model (AHBM) and in-crash Human Body Model (HBM) or dummies. In one use case the application of the developed method is shown.

INTRODUCTION

Two questions are becoming more and more important to be answered with the increasing market penetration and number of functions from PRE-SAFE® and driver assist systems. The first one is how to capture the occupant kinematics and predict it in a pre-crash phase and the second one is how to evaluate its influence on a crash result. A PRE-SAFE®[1] system in general serves for pre-conditioning of the vehicle occupant and partly also of the car in a critical driving situation. Driver assist systems can perform driving maneuvers to mitigate a critical driving condition, e.g. undertaking a braking or steering action to avoid a suddenly appearing obstacle. During such PRE-SAFE® or/and assist system actions the occupant position may change depending on the occurring low-g loading condition.

The classical occupant simulation method deals with the occupant behavior in crash phase. However, it is becoming considerably important to predict the occupant behavior prior to a crash event because most countermeasures performed on a vehicle or/and occupant are prior to this event. These countermeasures may influence the occupant initial position at the start of an unavoidable crash phase. Therefore, coupling the pre-crash phase with crash phase would capture the vehicle and occupant dynamics in the crash simulation. Such a procedure enables the evaluation of the influence of e.g. PRE-SAFE® parameters like triggering times and belt force levels and further optimizations of those parameters.

[1] PRE-SAFE® activates e.g. the reversible belt pretensioner, inflatable multi-contour seat bolsters for side support, seat movement as pre-conditioning (for passenger)

METHOD

Method overview

The simulation process chain consists of three main steps (cf. Figure 1). In the first one a reduced pre-crash model is created to provide a robust and fast base to simulate the pre-crash phase. The second step contains the pre-crash data processing and data creation for the in-crash phase. In the last step a crash model with the inputs from the previous step is created containing the pre-crash dynamics and geometric requirements.

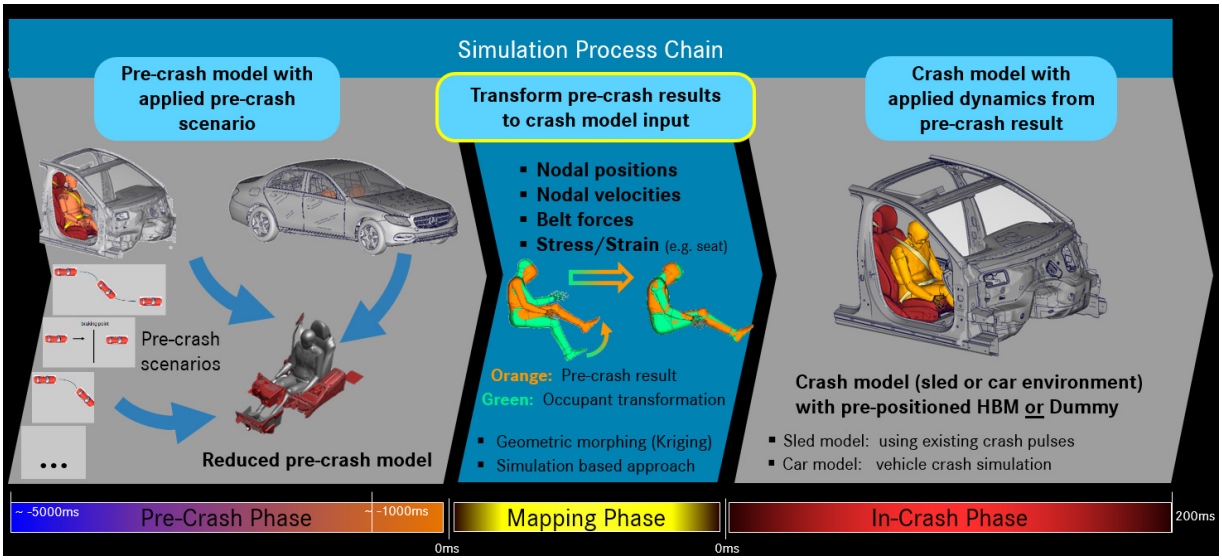

Figure 1: Overview of the Simulation Process Chain.

Due to the fact that simulation is not running in just one shot from pre-crash until the end of crash phase, it is possible to use different, optimized or suitable occupant models in each phase and also set up the crash configuration in a flexible way. That means by using the same pre-crash input it is possible to run different crash configurations.

Model setup of the pre-crash model

The pre-crash vehicle model is reduced as much as possible containing only the important surroundings of the occupant. Depending on the interaction possibility, parts having only slight contact with the occupant model are also switched to rigid material.

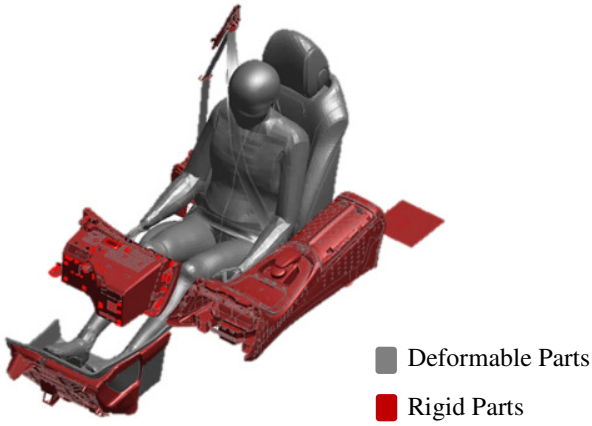

Figure 2: Pre-crash model set-up

The model contains mainly the seat, footwell area, parts of the instrument panel, center console & belt system. If needed the door trim could also be integrated. As occupant model the A-THUMS-D [4] model with active muscles is included.

The boundary conditions representing the pre-crash maneuver could be derived from vehicle test data or from simulation data (e.g. accident reconstruction, vehicle dynamics simulation, etc.). This data could be imposed as acceleration, velocity or displacement boundary condition on the pre-crash model.

The main focus by setting up the pre-crash model is to reduce the CPU time and ensure the robustness since the required time frame is much longer (up to 5sec.) than the common used time duration for crash simulation. Due to long simulation time usage of the double precision version of the FE solver could be necessary.

Occupant Models for crash and pre-crash phase
For each phase a different version of the THUMS-D occupant model is used.

THUMS-D Human Body Model The HBM used in this study is the THUMS-D 50th percentile occupant model. The THUMS-D model represents a mid-size adult male occupant model, whose height and weight are 175 cm and 73.5 kg, respectively. The model is derived from THUMS® [5] classical version 1 & 3. This model was previously modified for in-house Daimler AG usage. The modifications conducted on this model involved mesh refinement in several body regions, connections in lower extremities and implementation of a new shoulder model. This model is henceforth, in the study is referred as THUMS-D as it was developed for the crash phase ("in-crash"). Figure 3 (a) below illustrates the THUMS-D model.

Active THUMS-D Human Body Model The *Active THUMS-D* human body model is developed based on "relaxed" THUMS-D which is derived from the THUMS-D explained above. Initial investigations made obvious that available HBM models and therefore also THUMD-D validated under high g loading conditions, are not applicable under low g conditions. There general behavior is too stiff and muscle control cannot be implemented directly. The details of relaxed THUMS-D model development are discussed in our research conducted previously [6]. Relaxed THUMS-D is then integrated with active muscles [4] to create *Active THUMS-D*. Figure 3(b) below illustrates the *Active THUMS-D* model ("A-THUMS-D").

(a) THUMS-D (b) Active THUMS-D

Figure 3: In-crash & Active pre-crash Human Body Models

Data Transfer

As described in the previous sections, the pre-crash simulations are performed using a modified THUMS model that involves also active muscles to reflect the physical behavior of the human body during the low-g pre-crash phase and which also has been validated accordingly. On the other side, the in-crash phase requires a (mostly passive) model, which has been validated against in-crash (high-g) load cases. For the most general case, the pre-crash and in-crash models could be totally different in terms of meshing, materials and geometry, e.g. Active THUMS-D model for pre-crash and dummy model for the in-crash phase. Thus, no direct (one-to-one) relation between the two model meshes is available.

At the end of the pre-crash phase, the model's posture is obviously different from the initial standard posture (actual nodal positions) and also is in motion (actual nodal velocities), according to the pre-crash situation, e.g. lane change and/or braking maneuver. This requires a transfer of the nodal positions and velocities from the pre-crash to the in-crash phase. The latter is necessary to reflect the initial motion at the start of the in-crash phase. At the same time, a decent mesh quality has to be ensured to enable a stable simulation process of the in-crash phase and aspects of automation also have to be considered to include the data transfer method into a process chain with as little user interaction as possible.

AdaPT3 - Adjustment and Positioning Tool for Human Models To achieve this, a generic software tool is being developed by the authors to simplify and automate positioning and scaling processes with special applications to human body models (cf. Figure 4). Multiple geometric transformation procedures, like e.g. translations or rotations of model regions, are implemented, which are solely based on nodal relocations. The mesh smoothing of interfacial parts can be realized by simulations or interpolation methods like for instance the kriging or radial basis function methods.

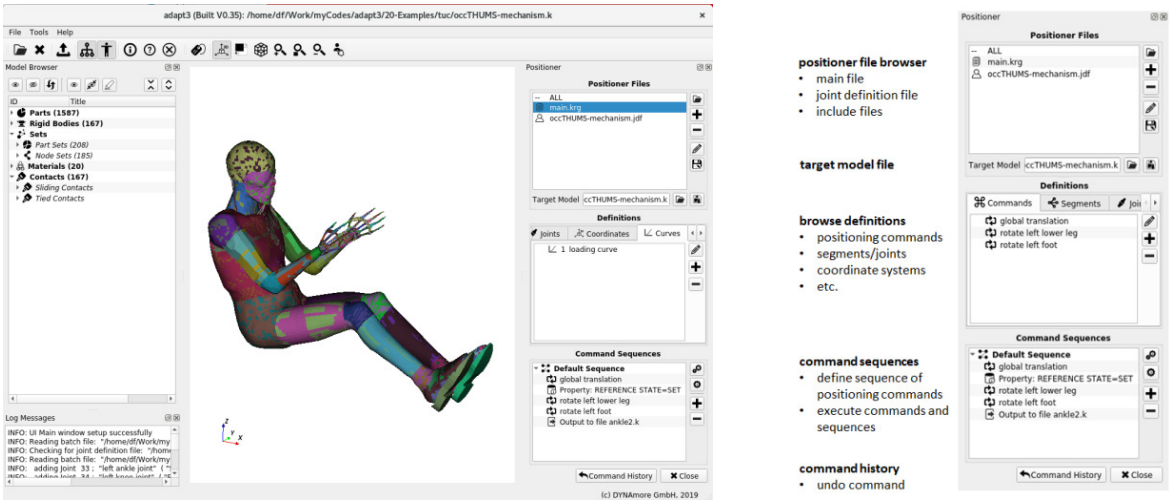

Figure 4: Main GUI of AdaPT3 showing the THUMS human model (left) and the positioner widget (right)

The tool is a generic tool which is not bound to a specific human model. The model dependency is rather realized by positioning and configuration files. Here model-specific definitions are given in terms of body segments (cf. Figure 5), joints, local coordinate systems or curves and task-specific definitions in terms of rotations, translations or scaling commands are specified to achieve a specific positioning task. These commands can be organized in positioning sequences and automatically run in a batch mode or interactively in the graphical user interface (GUI). Other features of the tool are for instance a browser for the positioning files, a command overview and history (UNDO) widget, a special-purpose positioner file editor, import/export capabilities and the possibility to interactively position the model or generate simulation decks.

Furthermore, functionalities have been implemented into *AdaPT3* to realize the posture transfer and the velocity mapping from the pre-crash to the in-crash models.

Data Transfer Approach In the following, the pre-crash model is also denoted as the source model, while the in-crash model will be referred to as the target model. Since in the most general case, no direct relations are present between the source and target occupant models, both models are divided into segments which will act as basic common properties. The segmentation might be realized as depicted in Figure 5 and includes the left foot, left lower leg, left patella, left upper leg, pelvis, etc.

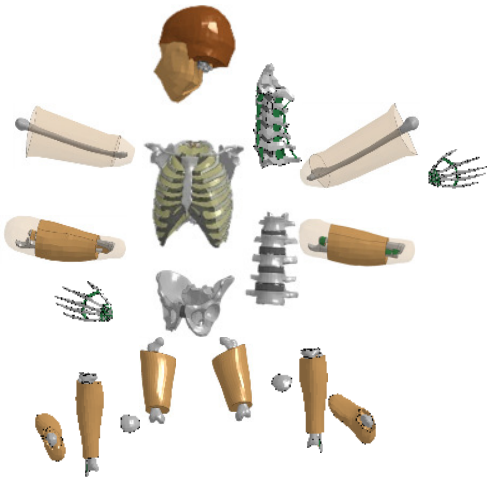

Figure 5: THUMS Model Segmentation

Based on this segmentation, the general mapping approach can roughly be defined using the following three steps

1. averaging of quantities within segments of the source model (pre-crash model)
2. transfer of averaged values between the models
3. distribution of averaged values to mesh of the target model (in-crash model)

The special implementations for the posture transfer and the velocity mapping are described in the following.

Posture Transfer

For the posture transfer, nodal positions have to be transferred from the source to the target models. Since no direct link is available between both meshes, the body segments of the target model are aligned to the segments of the source model. Therefore, local coordinate systems are defined on the body segments in the source and in the target model. To ensure a good model integrity and decent joint connections, the location and orientation of these local coordinate systems have to match the main features and the direction of the body segments. To perform the posture transfer, the local system of the target model is aligned with the local system of the source model and the nodes of the corresponding segment are updated accordingly. This implies that possible deformations of the segments are ignored which is acceptable since the segment deformations in low-g acceleration cases are mostly small in the pre-crash phase.

Please note that this step only repositions the body segments and the deformation of the joints and interfacial parts (e.g. knee flesh and ligaments, pelvis flesh) is entirely ignored. To adapt these interfacial parts, a model smoothing step is also required. This step can be based on geometric transformations or on simulations.

Simulation based positioning The most straightforward and mostly used approach is based on simulations (cf. Figure 6). A simulation deck is generated by the *AdaPT3* tool to move the body segments of the target model into the position of the source model. This is usually realized using the *string-pulling* or *marionette* technique, where string and damper elements pull the body parts towards the target position. The main advantage is that the physics, i.e. the material stiffness distribution and also contact interactions is accounted for during the simulation. However since current human models are still simplified in terms of representing real human anatomy and flexiblity, and this might lead to unphysiological motions also to unacceptable mesh quality. Another problem is that simulations can be very time consuming and postprocessing in terms of mesh smoothing and corrections might still be necessary.

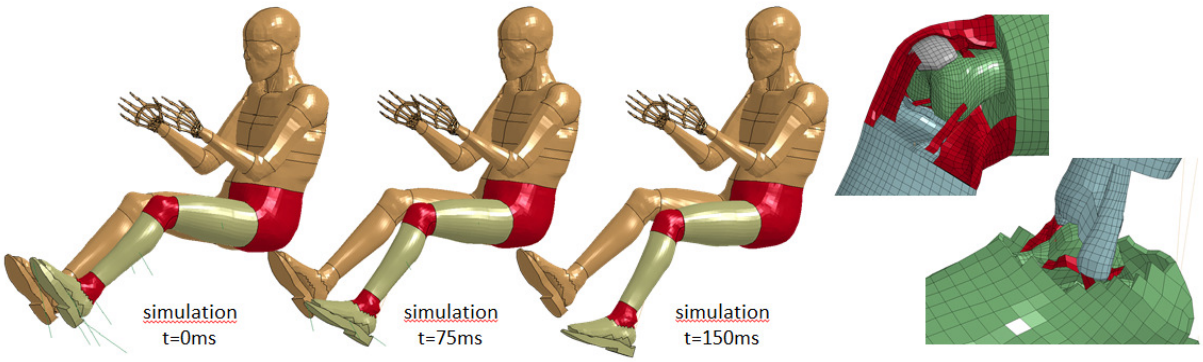

Figure 6: Posture adaptation using simulations

Positioning via geometric transformations Another approach is based on purely geometric mesh transformations using a kriging or radial basis function approach . Here the kriging method [7] is used to smooth the interfacial joint parts, e.g. the knee flesh or ligaments (cf. Figure 7). This requires the definition and decent choice of control points which define the basis for the interpolation approach. These control points are derived from the connected and prepositioned parts, like the upper and lower legs or the patella. The most important advantage of this method is the very fast execution time which is only a few seconds or minutes, depending on the number of control points. The mesh quality is also often better compared to the simulation results. However this method does not account for the physics of the model and might lead to problems in case of large posture changes. Thus the method should be restricted to small or moderate motions.

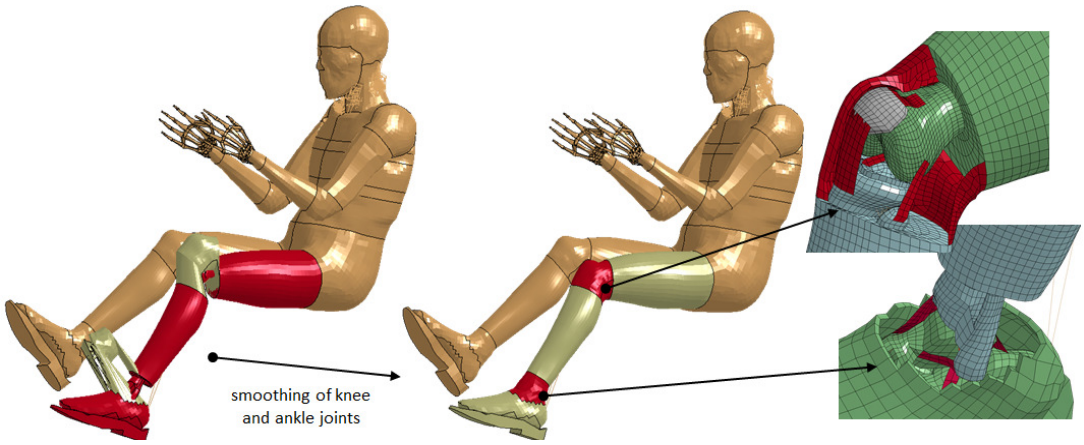

Figure 7: Smoothing of the prepositioned leg using the kriging method

Velocity Transfer

For the velocity transfer, again no direct link is available between the source and target models. Therefore the velocity mapping is again done on the body segment level where for each segment a representative set of nodes is selected. The nodal positions and velocities at the end of the pre-crash simulation are evaluated from the simulation result files. To compute the segment translational and rotational velocity, the nodal translational velocities are averaged over the source segment, the rotation center and the rotational velocities w.r.t. to the rotation center have to be computed on the source segment first. These quantities are then transferred to the target model and distributed to the nodes of the target segments using appropriate FE solver keyword cards. Finally, the simulation can be started using the initial segment velocities

Model setup of the crash model

The crash model setup comprises of standard decks either a sled model or a full vehicle model. The selection of the type of simulation deck depends on type of the load case. The methodology discussed above ensures the transfer of both the vehicle/sled model. Moreover, the flexibility offered by the tool chain is that it enables transfer of occupant data from pre-crash phase from Active HBM-to-HBM or Active HBM-to-Dummy.

APPLICATION IN COMBINED MANEUVER SCENARIO

The semi-automated methodology discussed above has been used for evaluating integrated safety – pre-crash and in-crash as a continuous event.

Pre-Crash maneuver

The present use case represents a simple conflict scenario. The ego vehicle is assumed to be travelling at 50kmph into another road, as shown in Figure 8a, having green traffic lights. The opponent vehicle e.g. ignores its red traffic light and, therefore, hits the ego vehicle from the side driving with a speed of 50kmph. The driver in the ego vehicle starts emergency breaking after becoming aware of the opponent car and decelerates from 50kmh to 31kmph at the time of impact.

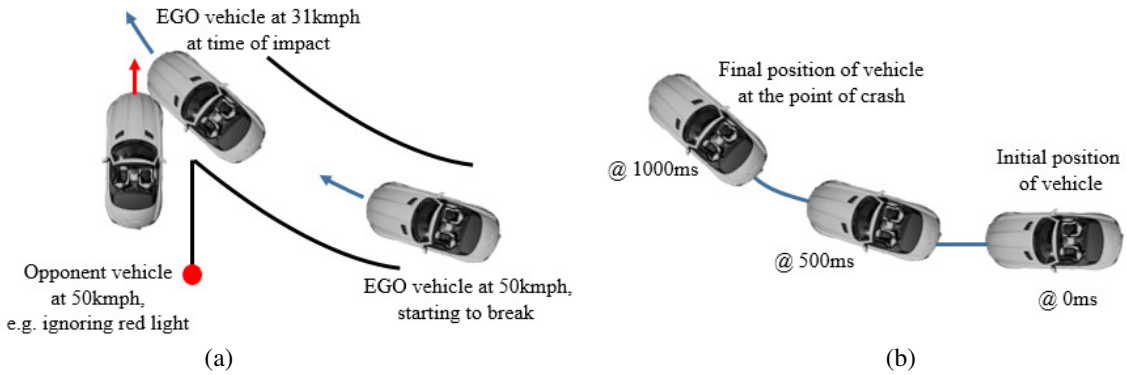

Figure 8: (a) Conflict scenario combined maneuver setup and (b) Vehicle trajectory during combined maneuver

Figure 9 illustrates the combined maneuver vehicle dynamic profile which was used to simulate pre-crash maneuver is based on the work conducted in OM4IS2 project [9].

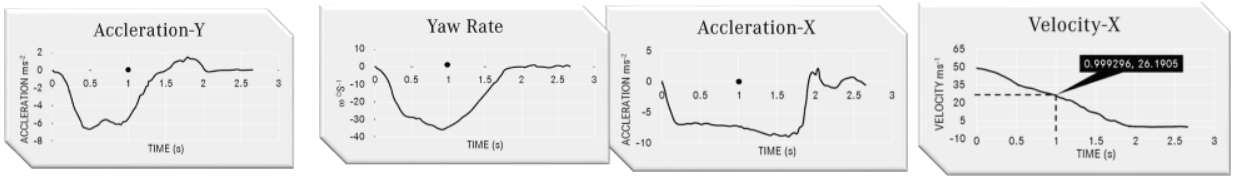

Figure 9: OM4IS2 combined maneuver dynamic profile [9]

The time duration of the pre-crash maneuver considered in this study is 1000ms. Figure 8b illustrates the vehicle trajectory and orientation at the end of pre-crash phase. The occupant under investigation is the passenger.

In-crash pulse generation

The crash pulse for conducting this study was generated from a vehicle to barrier impact (MDB-to-vehicle). The simulation was performed with position and velocity inputs from pre-crash end state. Figure 10 shows the full vehicle model and MDB configuration used for pulse generation. The vehicle FE model includes detailed BIW parts, engine compartment, doors, wheels and the suspension assembly etc.

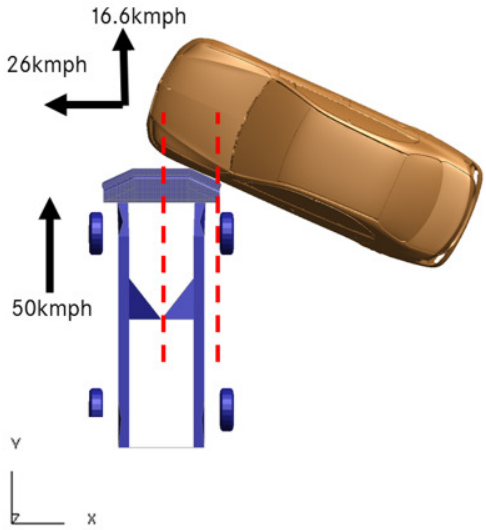

Figure 10: Final position of models for the full vehicle simulation

The motion pulse was generated based on vehicle kinematics using three nodes were minimal deformation was observed in structure. The displacement data from these three nodes were extracted and applied to the respective nodes in the sled to impart motion to the sled model. The sled simulation was overlaid over full vehicle simulation as illustrated in Figure 11 to verify transfer of displacement data which were now used in the FE sled model.

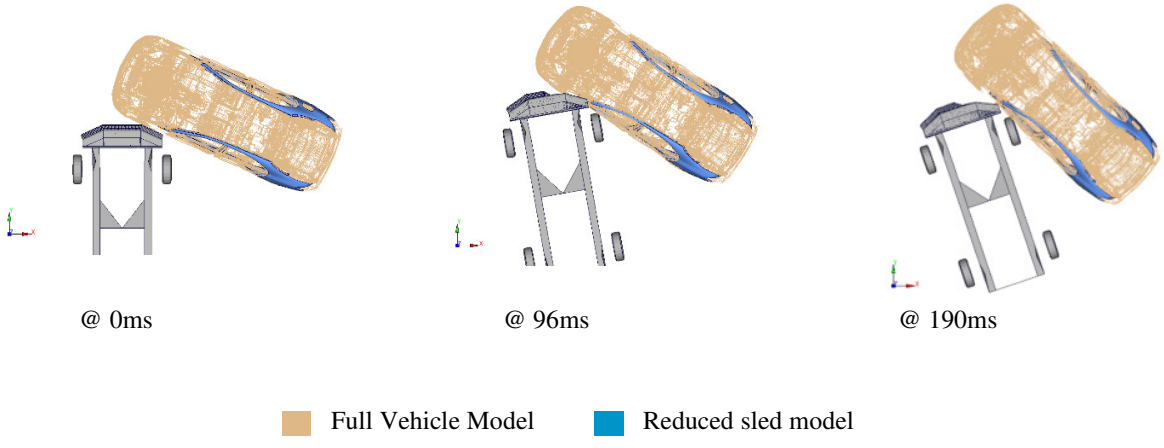

Figure 11: Sled model simulation overlaid over full vehicle simulation for extraction of motion pulse

Dynamic Occupant Data Transfer

The dynamic data at the end of the pre-crash phase was then transferred to in-crash phase model using the methodology above. The data transfer involved posture and velocity data transfer for the occupant. The in-crash HBM posture was generated using simulation approach (ref. Method section). Figure 12 shows the comparison of initial and final posture of the in-crash THUMS-D. The quality of the generated posture was evaluated by overlaying the initial state of in-crash and final state posture of pre-crash model as illustrated in Figure 12(b). The velocity data was transferred for individual body segments by estimating the average velocity of individual body region.

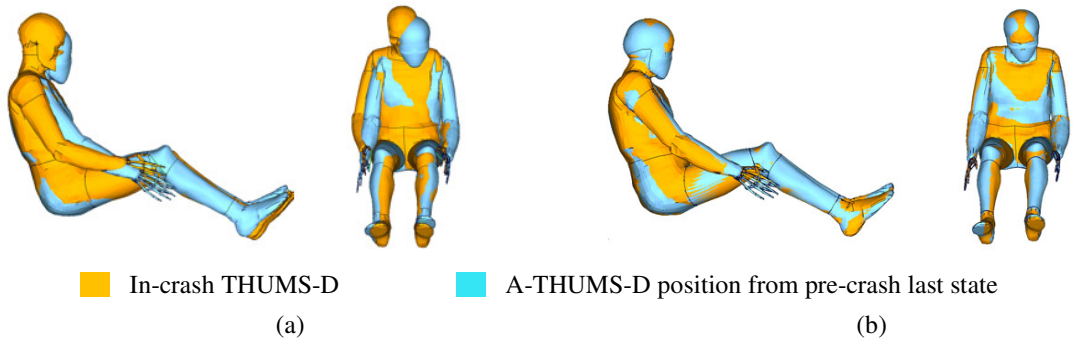

(a) (b)

Figure 12: (a) Initial position of the in-crash occupant (b) Final position of the in-crash occupant after pre-simulation

In-crash simulation carried out in sled model

The pre-crash vehicle response alters the occupant kinematics inside the vehicle. The occupant inside the vehicle starts reacting to the situation which is accomplised using A-THUMS-D for studying the effect of pre-safe system.

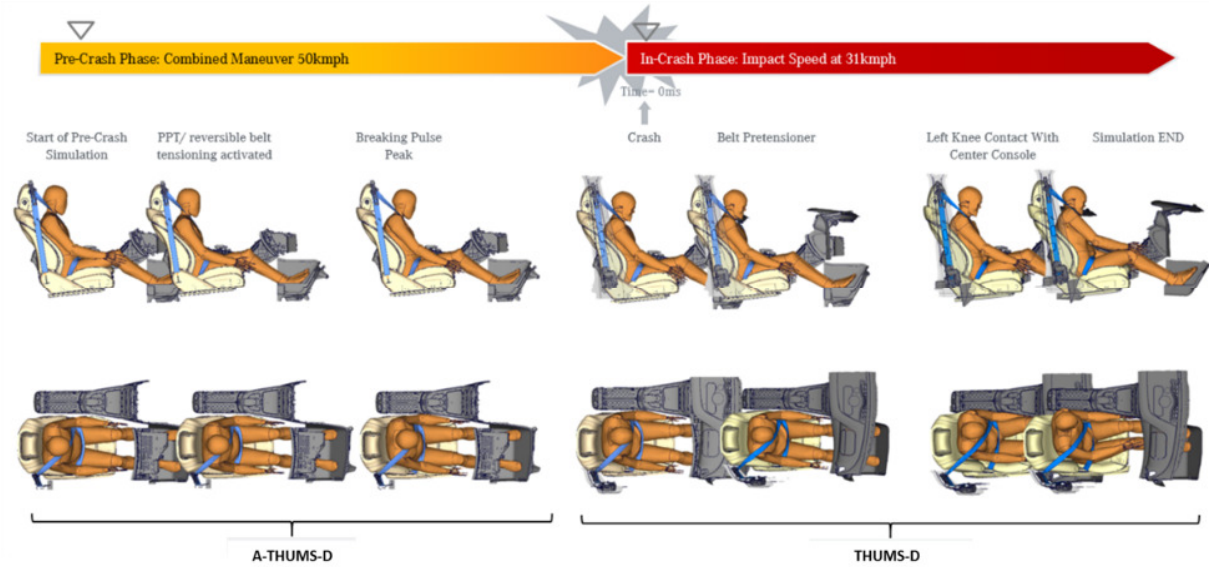

Figure 13: Occupant kinematics in pre-crash and in-crash scenario

In the current study, at 1000ms prior to impact brake assistant system is activated to avoid crash. The crash reversible pretensioner is activated to hold the occupant in seat at a given time point prior to crash. The influence of pre-crash vehicle dynamics moves the occupant closer to center console and instrument panel at the time of impact. The last state of pre-crash is the input for in-crash phase. In addition to the dynamic occupant data stresses in the seat were

also transferred to the in-crash environment. The passenger airbag is not triggered and only the belt pre-tensioner is activated. Complete occupant kinematics from pre-crash to in-crash is illustrated in Figure 13.

DISCUSSION AND LIMITATIONS

The two methods developed for posture data transfer have their own strengths and limitations. The 'geometric method' is fast but is suitable only for small changes in posture while the simulation approach though relatively more time consuming can be used for cases with large posture difference commonly observed when doing pre-crash to in-crash data transfer. Local deformations on the pre-crash occupant are currently not considered in the posture creation for the crash occupant, since those are in generall small.

Velocity data is currently transferred through averaging for body regions where small velocity gradients cannot be captured.

CONCLUSIONS

Integrated safety evaluation for the vehicle occupants in the simulation environment raises the demand to cover and couple the pre- and in-crash phases with a suitable simulation methodology. The presented tool chain offers the use of optimized occupant and vehicle models for each phase and the transfer of the needed pre-crash dynamics as initial condition for the in-crash model. Since both phases running separately in the simulation, it is possible to run different crash configurations with the same pre-crash phase and vice versa. The required posture for the occupant in the crash model can be achieved by using the simulation approach or the faster geometric transformation with automatic smoothing steps.

The presented simulation method is a step towards the development of a seamless integrated safety tool chain.

REFERENCES

[1] Hartlieb,M., Mayer, C., Richert, J., Öztürk, A., Mayer, F., Pal, S., Chitteti, R., „Implementation of new rib material model to a FE-Human Body Model for evaluation of the PRE-SAFE® Impulse Side Restraint System for side impact protection", *ESV Conference 2015*, Gothenburg

[2] Ghosh, P., Andersson, M., Mendoza Vazquez, M., Svensson, M., Mayer, C., Wismans, J. 2015. "A proposal for integrating pre-crash vehicle dynamics into occupant injury protection evaluation of small electric vehicles". *Proceedings of IRCOBI conference*, IRCOBI Conference, IRC-15-88, France.

[3] Teibinger, A., Krzysztof, M., Andersson, M., Wismans, J., Mayer, C., Ghosh, P., Luttenberger, P., D'Addetta, G. 2014. Report on definitions of requirements for a consistent safety analysis for occupant protection (including compatibility). *Reports of SafeEV Project, Grant Agreement No. 314265*, Austria.

[4] Martynenko, O., Neininger, F., Schmitt, S. 2019. "Development of a hybrid muscle controller in LSDYNA for an active Finite Element Human Body Model capable of occupant kinematics prediction in frontal and lateral maneuvers". *Proceeedings of ESV Conference,* Netherlands.

[5] Iwamoto, M., Kisanuki, Y., Watanabe, I., Furusu. K., Miki, K., Hasegawa, J. 2002. "Development of a finite element model of the total human model for safety (THUMS) and application to injury reconstruction". *Proceedings of IRCOBI conference*, IRCOBI Conference, Germany.

[6] Shelat, C., Ghosh, P., Chitteti, R., Mayer, C. 2016. "Relaxed HBM – an Enabler to Pre-Crash Safety System. Evaluation." *Proceedings of IRCOBI conference*, IRCOBI Conference, IRC-16-34, Spain.

[7] Trochu, F. A contouring Program based on Dual Kriging Interpolation", *Engineering with Computers, 9, 160-177*, 1993.

[8] Desai, C., Sharma, G., Shah, P., Ageorges, C., Mayer, C., Fressmann, D. 2012. "A generic Positioning Tool for Human Body FE Models", *Proceedings of IRCOBI Conference,* IRCOBI Conference, Ireland.

[9] Huber, P., Kirschbichler, S., Prüggler, A., Steidl T. 2015. "Passenger kinematics in braking, lane change and oblique driving maneuvers." *Proceedings of IRCOBI Conference*, IRCOBI Conference, IRC-15-89 France.

BRIC AND FIELD BRAIN INJURY RISK

Erik G. Takhounts
National Highway Traffic Safety Administration
USA

Vikas Hasija,
Bowhead (Systems & Technology Group)
USA

Matthew J. Craig
National Highway Traffic Safety Administration
USA

Paper Number 19-0154

ABSTRACT

This study investigates the adequacy of comparing the risk of brain injuries based on the available National Automotive Sampling System/Crashworthiness Data System (NASS/CDS) field data to the risk predicted by Brain Injury Criterion (BrIC) measured from an Anthropomorphic Test Device (ATD) in NHTSA's Research Moving Deformable Barrier (RMDB) oblique tests (fleet). Finite Element (FE) analysis was utilized to simulate crashes with a given range of Principal Direction of Force (PDOF) and change in velocity (Delta-V) to illustrate their effect on the field vs. fleet risk comparison. The simulation based results indicate that BrIC is highly dependent on PDOF and Delta-V. The methods applied for estimating brain injury risk from the simulation results demonstrate the importance of accounting for the distributions of both PDOF and Delta-V when comparing brain injury risk estimates from the field data versus those calculated from fleet testing.

KEYWORDS: BrIC, field data analysis, fleet data analysis, head/brain injury

INTRODUCTION

In this study, we computed the risk of brain injuries based on the available NASS/CDS field data and compared it to the risk predicted by BrIC in FE simulations of various PDOF and Delta-Vs representing a range of frontal crash conditions. Previous analyses of the field data (for example, Laituiri et at., 2016; Prasad et al., 2014) included crashes at PDOFs 11, 12, and 1 o'clock (that is spanning from -40^0 [near side oblique] to $+40^0$ [far side oblique] for the drivers) and the damage extent 3-6 (Delta-V ranging from under 25 mph [approximately 66% of the cases with the 3-6 damage extent] to around 35 mph). The fleet data (NHTSA's RMDB oblique tests) have the PDOF range between $20\text{-}30^0$ for both near and far sides, and the Delta-V span of 31-37 mph.

The purpose of this study is to investigate the adequacy of such comparisons between field and fleet risks when neither PDOF nor Delta-V ranges are comparable between the two datasets. Because of such incompatibility of the Delta-V and PDOF ranges between the two datasets, FE analysis of various frontal crash Delta-V and PDOF was utilized together with PDOF and Delta-V ranges/distributions from fleet and field data to derive adjusted simulation based estimates of brain injury risk.

METHODS

The efforts of this study can be separated into three distinct phases: (1) estimation of brain injury risk from field data; (2) application of a vehicle model and simulation to measure BrIC over a wide range of frontal crash Delta Vs and PDOF values; and (3) application of different filtering/calculation techniques to estimate brain injury risk from simulation data from (2) while considering the range of Delta V observed in fleet testing and the distribution of PDOF in frontal crashes from field data. The third step was done specifically for the purpose of demonstrating limitations that can be present when comparing field and fleet data while not considering the associated ranges and distributions of Delta-V and PDOF in the two data sets.

Field Data Analysis: The inclusion criteria for the ranges of PDOF and Delta-V in the field data analyses in previous studies were rather wide due to a small sample size for the specific PDOF and Delta-V. For the current study, the "field" data is referred to as all NASS/CDS passenger car, light truck and van frontal crash cases with a PDOF of -40^0 to $+40^0$ and Delta-V range between 31 and 37 mph. The brain injury field risk of AIS 2+, 3+, and 4+ (AIS – abbreviated injury scale) was calculated from weighted 2000-2015 NASS/CDS age 15+ belted drivers involved in frontal crashes with a Delta-V range of 31-37 mph and deployed frontal airbags. The case vehicles were restricted to passenger cars, light trucks and vans. Cases with rollovers were excluded. The risk at each AIS level was calculated as the ratio or percent of injury cases to the total weighted case count for the target population described above.

Frontal Crash FE Simulation: An FE model of a mid-size sedan was created and the GHBMC-OS (Global Human Body Modeling Consortium Simplified 50th Percentile Male, v1.8) FE model was utilized to simulate crashes at various PDOFs and Delta-Vs (Figure 1).

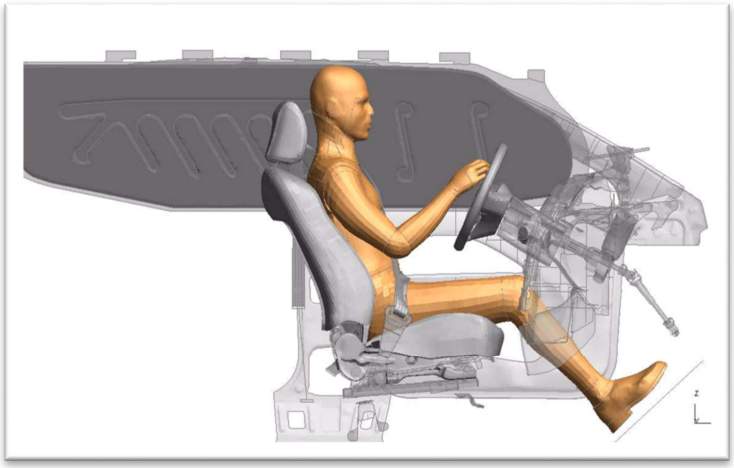

Figure 1: GHBMC-OS 50th % male FE model in a mid-sized sedan.

BrIC values were calculated for each combination of the investigated parameters (Table 1). The simulations were done without any structural deformation of the vehicle model (i.e. were run similar to a model of a sled test). No attempts were made to recreate/reconstruct actual field cases nor replicate the results of a specific crash test. Instead, the model was developed to represent an average passenger car. The range of Delta-V and PDOF values that were simulated overlap what was observed in NHTSA's RMDB oblique fleet testing, where PDOF ranges from 20^0 to 30^0 for both near and far sides, and the Delta-V spans from 31 mph to 37 mph. The simulated PDOF range covers what would normally be defined as a frontal crash in NASS-CDS when considering 11 o'clock to 1 o'clock frontal crashes.

Table 1. Investigated parameters in FE simulation of frontal crashes (MFR is Mass Flow Rate).

Parameters	Baseline value	Range
Delta-V	35 mph	25 mph - 47 mph
PDOF (degrees)	0	-40 (320) to +40
Frontal airbag friction	0.5	N/A
Frontal airbag MFR (scaling factor)	1	N/A
Frontal airbag firing time (ms)	18	N/A
Load limiter (N)	3000	N/A
Side airbag friction	0.5	N/A
Side airbag MFR (scaling factor)	1	N/A
Side airbag firing time (ms)	18	N/A

Estimation of Brain Injury Risk: Using a single set of FE simulation results over a range of applicable frontal crash Delta-V and PDOF (per Table 1), simulation based brain injury risks were calculated while considering the PDOF and Delta-V ranges associated with the respective field and fleet data. Brain injury risk was calculated from the simulated BrIC values using the CSDM based risk functions described in Takhounts et al. (2013).

Three simulation based estimates of brain injury risk were calculated. The first was based on a simple average of BrIC for all simulations from 31 to 37 mph. The second version limited the average risk calculation to the PDOFs observed in NHTSA's RMDB oblique fleet testing (20-30^0). The final method used to estimate risk using the simulated BrIC data considered all simulation data over Delta-Vs of 31-37 mph (same as the first version), but with weighting applied based on the distribution of PDOFs obtained from the NASS/CDS field data for the Delta-V range of 31-37 mph.

RESULTS

Field Data Analysis: The distribution of PDOFs obtained from the NASS/CDS field data was very close to normal with the maximum at 0^0 (full-frontal crashes) representing approximately half of all the crashes (Figure 2). The NASS/CDS filter used to produce Figure 2 was the same as described above for the calculation of brain injury field risk.

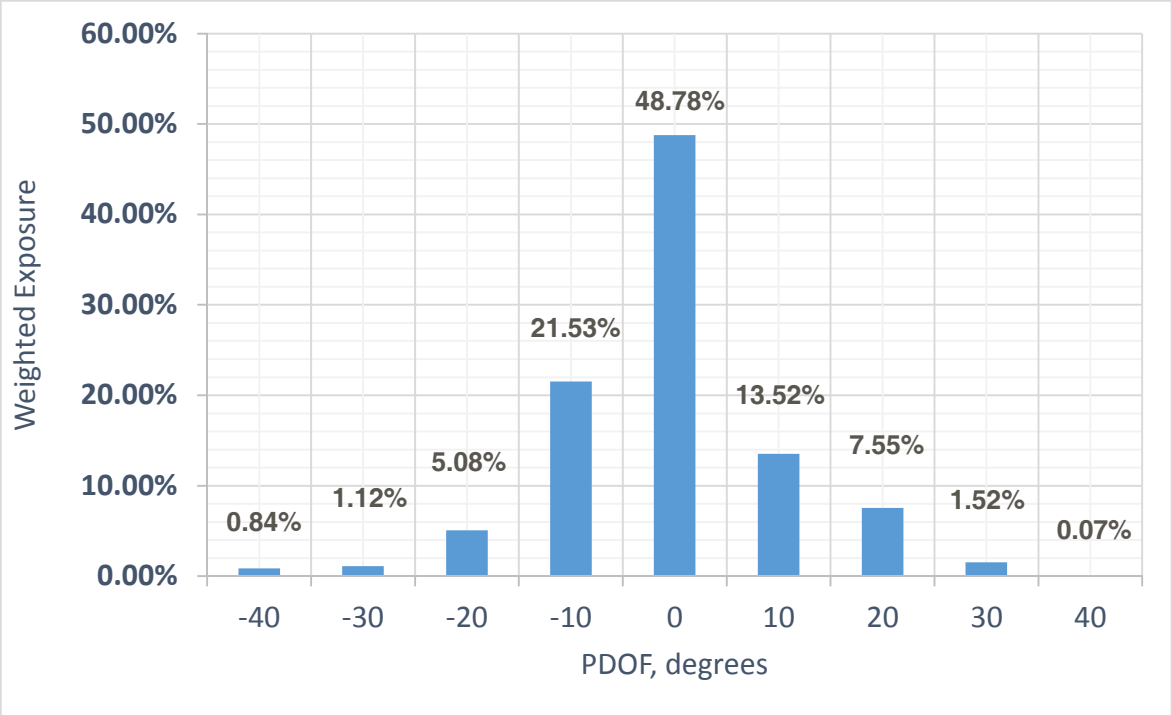

Figure 2: Weighted distribution of PDOF at Delta-V range 31-37 mph from the NASS/CDS field data.

The brain injury field risk from NASS/CDS of AIS2+, 3+, and 4+ for the Delta-V range of 31-37 mph (and PDOF of -40^0 to +40^0) was 7.59%, 3.34%, and 2.40% respectively. All brain injury cases at the three AIS levels were included in the respective risk calculations regardless of whether there was an accompanying skull and/or facial fracture.

Frontal Crash FE Simulation: Table 2 lists the values of BrIC from the simulation results for the parameters and ranges described in Table 1.

Table 2. Values of BrIC computed from the simulations for various Delta-V and PDOF.

DeltaV	PDOF=-40	PDOF=-30	PDOF=-20	PDOF=-10	PDOF=0	PDOF=10	PDOF=20	PDOF=30	PDOF=40
DV 25	0.553	0.688	0.534	0.524	0.462	0.482	0.625	0.699	0.707
DV 27	0.635	0.664	0.506	0.502	0.448	0.485	0.661	0.756	0.747
DV 29	0.713	0.683	0.498	0.481	0.469	0.497	0.661	0.821	0.824
DV 31	0.814	0.784	0.561	0.498	0.505	0.508	0.627	0.896	0.899
DV 33	0.855	0.784	0.619	0.536	0.527	0.519	0.71	1.066	0.9597
DV 35	0.959	0.759	0.593	0.615	0.555	0.548	0.986	1.268	1.008
DV 37	1.07	0.769	0.617	0.796	0.609	0.563	1.29	1.334	1.05
DV 39	1.196	1.05	0.738	0.883	0.62	0.571	1.465	1.3	1.13
DV 41	1.53	1.31	0.872	1.06	0.657	0.609	1.53	1.256	1.3
DV 43	1.693	1.098	0.989	1.23	0.697	0.607	1.61	1.39	1.765
DV 45	1.668	0.948	1.175	1.379	0.698	0.621	1.71	1.768	2.698
DV 47	1.824	1.074	1.31	1.147	0.654	0.651	1.81	2.26	3.95

Estimation of Brain Injury Risk: As previously noted, estimation of brain injury risk given the simulation results presented in Table 1 was done in three different ways.

The first version simply takes the average BrIC from the simulation results (Table 2) across all PDOFs for the Delta-V range of 31-37 mph (as was done by other researchers such as Prasad et al., 2014; Laituiri et at., 2016). The resulting average BrIC of 0.78 corresponds to 48.00%, 24.00%, and 17.00% risk of AIS2+, 3+, and 4+ brain injury (CSDM based injury risk from Takhounts et al. 2013).

The second version considers the same Delta-V range as above but limited to PDOFs of -30 to -20 and 20 to 30 degrees. As previously noted, this represents the range of PDOF observed in NHTSA RMDB oblique crash testing. The resulting average BrIC of 0.854 corresponds to 64.60%, 34.70%, and 25.80% for AIS 2+, 3+ and 4+, respectively, which is approximately an order of magnitude higher than that calculated from the NASS/CDS field data and in the same range obtained directly from the ATDs in NHTSA's RMDB oblique tests. This calculation was made by taking a simple average of BrIC values (from Table 2) for the Delta-V and PDOF ranges noted above (see bold rectangles in Table 2).

The prior two simulation based risk estimates did not consider the frequency or exposure of the respective PDOF/Delta V combinations in the field. Discrepancies in prediction among various studies can occur when the distribution of PDOF in the field is not considered in the calculation of averages. The formula for the average BrIC that includes the distribution of PDOF in the field is:

$$BrIC_{Ave} = \sum_{-\theta}^{+\theta}(\alpha_i BrIC_i), \quad (1)$$

where θ is the PDOF angle ranging from -40 to +40 degrees, α_i is the field exposure for each PDOF given in Figure 2, $BrIC_i$ is the average BrIC for 31-37 mph for each PDOF given in Table 2. For example, for a full-frontal case at 0 degree PDOF, the α_0 = 48.78% = 0.4878, and $BrIC_0$ = (0.505 + 0.527 + 0.555 + 0.609)/4 = 0.549. Average BrIC values for each PDOF at 31-37 mph are given in Table 3.

Table 3. Average values of BrIC (in bold) for the 31-37 mph Delta-V range.

	PDOF (degrees)								
	-40	-30	-20	-10	0	10	20	30	40
Delta-V = 31-37	**0.925**	**0.774**	**0.598**	**0.611**	**0.549**	**0.535**	**0.903**	**1.141**	**0.979**

Taking PDOF exposure from Figure 2 and corresponding values of BrIC from Table 3, the average BrIC calculated from equation 1 is:

$BrIC_{Ave} = \sum_{-\theta}^{+\theta}(\alpha_i BrIC_i)$ = 0.925*0.0084 + 0.774* 0.0112 + 0.598*0.0508 + 0.611*0.2153 + 0.549*0.4878 + 0.535*0.1352 + 0.903*0.0755 + 1.141*0.0152 + 0.979*0.0007 = 0.605.

Note that the sum of α_i in the formula above equals to 1 indicating that all possible PDOF exposures in Figure 2 are accounted for.

The risks of AIS 2+, 3+, and 4+ brain injury for BrIC = 0.605 are 8.08%, 3.40%, and 2.39% respectively. All the presented above values of BrIC (based on CSDM per Takhounts et al. 2013) are tabulated below in Table 4.

Table 4. Risks of AIS2+, 3+, and 4+ brain injury based on the field data and various BrIC values.

	AIS 2+	AIS 3+	AIS 4+
Average Field Weighted Risk for Delta-V 31-37 mph – NASS/CDS	7.59%	3.34%	2.40%
BrIC = 0.78 - simulation based average BrIC for Delta-V 31-37 mph and all PDOF	48.00%	24.00%	17.00%
BrIC = 0.854 - simulation based average BrIC for Delta-V 31-37 mph and PDOFs -30^0 to -20^0 and $+20^0$ to $+30^0$	64.60%	34.70%	25.80%
BrIC = 0.605 - simulation based average BrIC at Delta-V 31-37 mph weighted by the probability of occurrence of crash at each PDOF from -40^0 to $+40^0$	8.08%	3.40%	2.39%

When the average BrIC is calculated per equation 1, i.e., considering the actual PDOF exposure in the field given in Figure 2, as given in the last row in Table 4, the simulation based brain injury risks at various severities are comparable to those taken directly from the field (first row in Table 4).

Other formulas calculate such risks by simply lumping together all the risks at various PDOFs into one simple average without considering the PDOF exposure. Such calculations implicitly assume that the field PDOF exposure is uniform, i.e., a rectangular rather than normal distribution of PDOF given in Figure 2, with equal exposure coefficients in equation 1. However, when PDOF exposure is considered, the risks of brain injury calculated by BrIC are comparable to those obtained directly from the NASS/CDS field data.

Similar considerations are applicable when the range of Delta-V becomes wider (as in Prasad et al., 2014). In this case the Delta-V distribution in the field must be accounted for and equation (1) for calculating average BrIC should be modified (equation 2) to include an additional coefficient representing the Delta-V exposure in the field:

$$BrIC_{Ave} = \sum_{-\theta}^{+\theta}\sum_{dv1}^{dv2}(\alpha_i \beta_j BrIC_{ij}), \quad (2)$$

where βj is the Delta-V exposure at each PDOF, dv_1 and dv_2 are the lowest and highest Delta-Vs under consideration (for example, if all the values of BrIC were used from Table 2, then dv_1 = 25 mph and dv_2 = 47 mph), and $BrIC_{ij}$ is the value of BrIC at a given PDOF and Delta-V. Similarly, for the analysis of the field (and/or fleet) data based brain injury risk, the risks at each PDOF and Delta-V should be weighted according

to equation (2). In the case when such field data resolution is not available (due to small sample size), some averaging may be assumed as was demonstrated above using equation (1). However, when 66% of the cases are under Delta-V of 25 mph (such as the case when considering the damage extent range of 3 to 6 used in Prasad et al., 2014), which corresponds to much lower values of BrIC compared to those at 35 mph (see Table 2), then lumping all the data together and taking a simple average will predictably lead to incorrect assessment of the brain injury risk.

If a brain injury risks comparison between field and fleet data is to be made, then both PDOF and Delta-V ranges in the field and fleet datasets should be the same and the distributions of PDOF and Delta-V that occur in the field must be accounted for in the fleet data.

CONCLUSIONS

Simulation based results indicate:

1. BrIC is highly dependent on Delta-V and PDOF (Table 2).
2. When overall field risk of brain injury is compared to that calculated by BrIC from the fleet data, both Delta-V and PDOF ranges should be comparable between the two datasets and the distributions of PDOF and Delta-V that occur in the field data must be accounted for in the fleet data.
3. When conclusion 2 is satisfied, the brain injury risks for field and fleet are comparable (Table 4).

REFERENCES

[1] Laituri, T.R., Henry, S., Pline, K., Li, G., Frankstein, M., Weerappuli, P (2016) New risk curves for NHTSA's Brain Injury Criterion (BrIC): Derivations and Assessments. Stapp Car Crash Journal, Vol 60; pp 301-362.

[2] Prasad, P., Dalmotas, D., German, A. (2014) The Field relevance of NHTSA's oblique research moving deformable barrier tests. Stapp Car Crash Journal, Vol 58; pp 175-195.

[3] Takhounts, E.G., Craig, M.J., Moorhouse, K., McFadden, J., Hasija, V. (2013) Development of brain injury criteria (BrIC). Stapp Car Crash Journal 57:243-66.

DEVELOPMENT OF A HUMAN FE MODEL FOR ELDERLY FEMALE OCCUPANTS IN SIDE CRASHES

Hisaki Sugaya, Yukou Takahashi, Yasuaki Gunji, Yasuhiro Dokko
Honda R&D Co., Ltd. Automobile R&D Center
Japan

Murthy Ayyagari, Bryant Whitcomb, Craig Markusic
Honda R&D Americas, Inc.
United States

Amanda Agnew, Yun-Seok Kang, John Bolte IV
Injury Biomechanics Research Center (IBRC), The Ohio State University
United States

Paper Number 19-0052

ABSTRACT

A high fatality rate of the elderly in traffic crashes is an important issue to consider when facing an aging society in the future. Left side impacts have been found to be the most frequent when considering severe crashes involving elderly people that resulted in Abbreviated Injury Scale (AIS) 4+ injuries in the United States. Additionally, the frequency of rib fractures in female occupants is significantly higher than males in those over sixty years in a side impact. Therefore, there is a need to reduce rib fractures in elderly females in side impacts, which should significantly decrease the number of fatalities in these types of crashes. Currently there are no evaluation tools for elderly female occupants with increased fragility. The objective of this study was to develop a Human Body Model (HBM) of an elderly female with increased fragility to use in simulations which focus on side impacts.

The material properties of rib cortical bone were determined using average data from published literatures. A rib bending simulation was conducted to compare force-deflection response with published experimental data. The rib cortex model included thirty-two sections of a rib, in which the thickness of each section was determined by comparing to published precise cross-sectional data. The evaluated rib model was then applied to the full-body HBM of an elderly male which was developed in a past study. Using the full body model geometrically scaled to elderly female, published side impact sled tests at 28 km/h of delta-V with post mortem human subjects were simulated to compare kinematics, rib fracture locations, and thoracic deflection obtained from chest band data. Comparison of the force-deflection response of the rib in bending showed that the simulation result fell within the overall experimental range. In the side impact sled simulations, the predicted trajectories of T1, T12, and the pelvis were found to be similar to those from the experiment. The number of rib fractures, fracture timing, fracture locations and overall thoracic deflection in the simulation exhibited a similar trend to the experimental data.

The HBM developed by applying rib material properties and geometrical scaling for an elderly female well represented upper body kinematics, rib fractures and thoracic deflection in a side impact when compared to published PMHS experiments.

INTRODUCTION

The National Highway Traffic Safety Administration (NHTSA) reported the elderly population, age 65 or older, in the U.S. reached 47.8 million in 2015; this is nearly 15 percent of the total U.S. population [1]. Also, the number of licensed elderly drivers increased by 33% from 2006 to 2015, reaching 40.1 million. Furthermore, Ortman et al. [2] predicted that the elderly population will expand to 83.7 million by the year 2050. NHTSA also reported the number of elderly fatalities increased by 3% from 2006 to 2015, even though the overall number of fatalities decreased by 19%. [1] Therefore, it is possible that the number of fatalities of elderly people in traffic crashes will further increase due to an aging society. As a result, protection for the elderly in traffic crashes is critical.

A previous study done by NHTSA analyzed the National Automotive Sampling System Crashworthiness Data System (NASS-CDS) and found that the percentage of drivers sustaining Maximum Abbreviated Injury Scale (MAIS) 4+ injuries relative to the number of drivers involved in crashes is significantly larger for the elderly population (greater than 65 years old) compared to occupants between 25 and 44 years old, 1.85% compared to 0.76%, respectively [3]. Specifically, for left-side impacts without rollover the percentage of elderly occupants becomes even larger and is the largest percentage of all crash modes. This suggests that the protection of elderly drivers involved in left-side impacts is important.

One of the factors that likely contributes to the high probability of severe and fatal injuries to elderly occupants is the increased fragility of their bones. For example, Agnew et al. [4] showed that in whole rib bending tests, the tensile failure strain in the rib significantly decreases with age. This group also showed that body height had a positive relationship with both peak force and total fracture energy. [5] Therefore, shorter occupants, such as small elderly females, may have a higher probability of severe and fatal injuries. Ramachandra et al. [6] revealed that the probability of AIS3+ injury in side impact crashes also depends on sex. According to the study, in near-side impacts, the probability of injury to the thorax and the ribs were significantly higher for females than for males within the elderly population, (over 60 years of age). All of these studies suggest that small, older female drivers in near-side impacts are more susceptible to thoracic injuries, particularly rib fractures.

Despite the growing importance to better understand how to protect elderly females in near-side impacts, few studies have investigated this impact configuration. A recent study by Shurtz et al. [7] conducted side impact sled tests using two small elderly female post-mortem human subjects (PMHS). These sled tests included realistic boundary conditions of a typical near-side impact including: seat-belt with a pretensioner, side airbag and intruding car door. In addition, there has only been one validated Human Body Model (HBM) representing an elderly female published to date [8]. This elderly female HBM was validated against a side sled test with rigid wall, which is not a realistic boundary condition. Unfortunately, at this time there is not a validated small elderly female HBM that could be used to test safety systems in near side impact scenarios. Therefore, the objective of this study was to develop a HBM of a small elderly female occupant under realistic boundary conditions in the near side.

METHOD

A two-phase approach, model creation and model validation, was taken to achieve our goal as shown in Figure 1. During the model creation phase, a three-step approach was taken including: (1) scale a whole body model from a 50th male (AM50) to a 5th female (AF5), (2) create a single rib model to match previous rib experimental testing, and (3) create an average elderly female rib model using literatures. The modeled fragile female ribs were then used in the creation of the AF5 model and validated. Validation was accomplished in terms of prediction of rib fractures and thoracic injury severity using three different experiments: (1) single rib experimental bending test, (2) a whole-body thoracic impact test series and (3) whole-body PMHS side sled test using realistic boundary conditions.

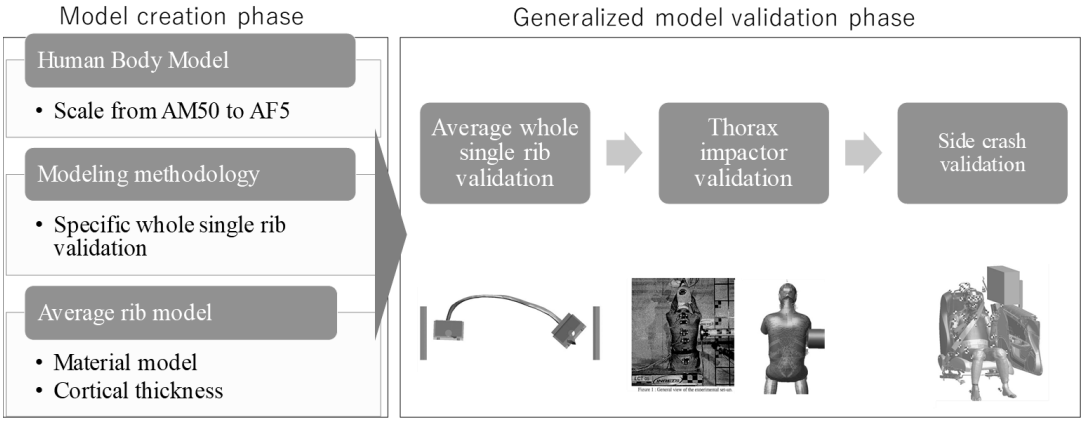

Figure 1. Scheme of development of HBM for elderly female

Model Creation Phase (Whole Human Body Model)
The Human Body Model (HBM) AM50 was evaluated as an elderly occupant by Dokko et al.[9]. This model served as the baseline model that was then adapted with finite element capable software, LS-DYNA (version R7.1 LSTC, Livermore, CA, USA) to convert it into the AF5 model. The thorax of the AM50 model had been developed based on a CT of a single elderly male with average body size, 175 cm in height and a mass of 77kg. The material properties used to represent the cortical bone located in the ribs were determined using tensile test results reported by Kemper et al. [10][11]. The AM50 elderly model was validated against thoracic impact tests documented in ISO-TR9790 (1997) [12] along with side and frontal sled tests conducted by Lessley et al. [13] and Shaw et al. [14]. The biofidelity score for these validation tests ranged from 0.23 - 1.18 based on the assessment scheme proposed by Rhule et al. [15].

The AM50 HBM was scaled to that of a small female body size (AF5). The model was scaled to 0.86 times relative to the x, y, and z axes equally to accomplish a stature of 151 cm. In addition, the densities of the internal organs were adjusted to match the target total body mass which was 47 kg based on a dataset published by Robbins et al. [16]. The skeletal model of the thorax of the AF5 was then compared with a statistical small female model published by Wang et al. [17]. It was found to be close to the statistical rib-cage geometry as shown in Figure 2. The AF5 thorax was approximately7% larger in width and 0.5% larger in depth.

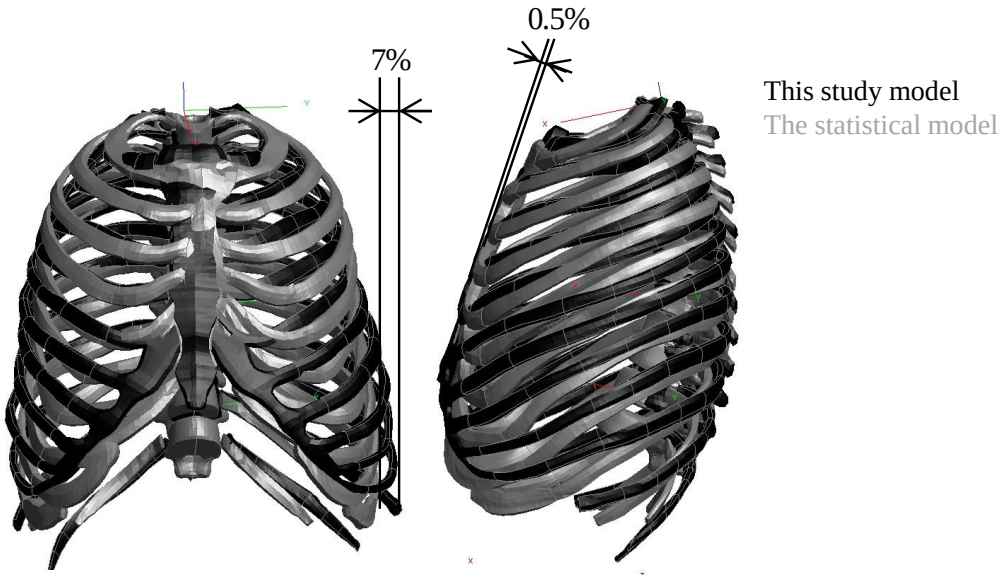

Figure 2. Comparison between thoracic skeletal morphology in the simulation and in the statistical model for the small elderly female

Model Creation Phase (Determination of modeling methodology for whole single rib – Parametric study)
As stated one of the validation parameters for the AF5 model is intended to be the number and location of rib fractures. Therefore, it was critical to model the correct material property for rib cortical bone and validate a whole single rib against published experimental testing. Whole single rib tests were simulated to determine the most appropriate rib modeling methodology; variables investigated included: number of sections along the length of the rib, cortical thickness of each section and the best material properties to use for cortical bone. Experimental bending tests using a whole 6th rib published by Agnew et al. [4] were simulated and the results were compared with the experimental results to determine the best modeling methodology.

Two ribs from two different female subjects used in the published whole bone experimental tests were selected to model and simulate. The two selected experimental ribs, subject 1 and subject 2, were scanned using both a FARO laser scanner, as well as computed tomography (CT). The images were used to create computer-aided design (CAD)

models of the surface of the ribs using Mimics (Ver. 12.0, Materialise, Leuven, Belgium). Cortical bone models were then developed with shell mesh and filled in with solid mesh to reproduce the trabecular bone from the CAD models. Cortical thicknesses of each rib was measured using both CT data and histological rib cross-section data. Each rib was sectioned into 8 cross-sections equally divided along the length of the rib. For each of the 8 cross-sections, four thicknesses were calculated: cutaneous, pleural, superior and inferior. The cortical thicknesses were measured for all 8 cross-sections from the CT images. However only one cross section of each rib, located 67% along the length of the rib, underwent histological analysis. The CT scan had an in-plane resolution of 0.146 mm, while the histological analysis had a resolution of 1,446 pix/mm (0.000692 mm/pix) as published by Agnew et al. [4]

The test set-up of the whole-rib simulation tests matched the experimental tests. The vertebral and sternal ends of the rib model were constrained in pots which were oriented perpendicular to the rib as it entered the pot. The pots on both ends were allowed to rotate about the z-axis. In addition, the sternal end could be moved posteriorly along the x-axis, representing a frontal crash. The reaction force was measured at the vertebral end of the rib in the experimental tests by Agnew et al. [4] and also in the simulation along with the displacement of the sternal end of the rib for a direct comparison to calibrate the model. As mentioned, a parametric study was conducted using this simulation changing three key parameters: number of sections along the length of the rib, cortical thickness of each section and the best material properties to use for cortical bone. The parametric study matrix is shown in Table 1.

Table 1.
Parametric study matrix of bending simulation and results

Case ID		Model 1	Model 2	Model 3	Model 4
Parameter	Number of total divisions in the rib	16	32	32	32
	Thickness source	CT	CT	Function between microscope and CT	Function between microscope and CT
	Material properties	MAT24 Tension	MAT24 Tension	MAT24 Tension	MAT124 Tension & Compression

Parameter 1 – Number of divisions in the rib: As stated earlier, the two modeled ribs were portioned into 8 sections longitudinally along the length of the rib. For each longitudinal section, the cortical bone was then broken into 4 sections circumferentially. The first variable the parametric study evaluated was how many divisions of cortical bone were needed to adequately model the experimental ribs. A comparison between a simplified model with 16 cortical bone divisions (Model 1) and a more detailed model of 32 cortical bone divisions (Model 2, Model 3 & Model 4) as shown in Figure 4. The simplified model only looked at using 4 of the longitudinal cross-sections versus all 8.

Parameter 2 – Cortical bone thickness source: Two types of cortical bone thickness values were applied. As mentioned previously, thickness values came from both the CT scans, in all 8 longitudinal cross-sections, and a histological measurement, at a single cross-section. On the cross-section that had both a CT measurement and a histological measurement, a correlation between the two measurement techniques was calculated. The relationship between the measured histological cortical thickness, which is considered the gold standard for measuring cortical bone thickness, and the CT thicknesses was calculated as shown in Table 2, Equation 1 and Figure 3. The relationship as defined in equation (1) had a R square value of 0.83 certifying good correlation between the data when using a linear approximation based on a least-squares fit. Model 1 and Model 2 used cortical bone thicknesses as measured using the CT scans only, while Model 3 and Model 4 used the function as defined in Equation 1 to calculate the thickness of each cortical bone segment.

$$D_{mod} = 1.2253 * D_{ct} - 0.6302 \quad \text{(Equation 1)}$$

Table 2.
Cortical thickness measurement between CT and Histological measurement

	Thickness source	CT (mm)	Histological measurement (mm)
Subject 1	Superior cortex	0.77	0.21
	Cutaneous cortex	0.86	0.25
	Inferior cortex	0.74	0.14
	Pleural cortex	1.00	0.63
Subject 2	Superior cortex	0.49	0.19
	Cutaneous cortex	1.17	0.81
	Inferior cortex	0.66	0.47
	Pleural cortex	1.24	0.97

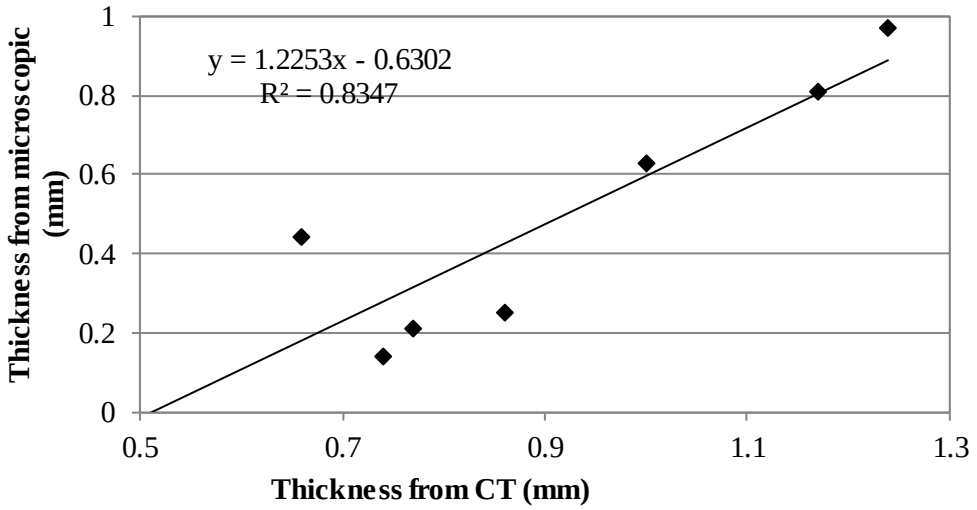

Figure 3. Relationship between measurements scanned from CT and from microscope

Parameter 3 – Cortical bone material property: The material properties of the two tested experimental ribs were calculated from experimental coupon tests conducted by Albert et al. [18]. After the ribs were tested in the whole-rib experimental set-up, the ribs were taken to Virginia Tech University where the coupon tests were completed. The material property of the trabecular bone was applied using the same value from Dokko et al. [9]. In addition, the strain rate of cortical bone and trabecular bone was applied according to a previous study by Takahashi et al. [19] The material properties for each subject was obtained from the coupon testing published by Albert et al. [18]. Compression property was determined as 1.2 times tension property from Kemper et al. [11] For Model 1, Model 2 and Model 3, these values were all the same as shown in Table 1 as MAT24 PIECEWISE_LINEAR_PLASTICITY specifying only tension. However, in Model 4, MAT124 PLASTICITY_COMPRESSION_TENSION were applied specifying tension and compression, respectively.

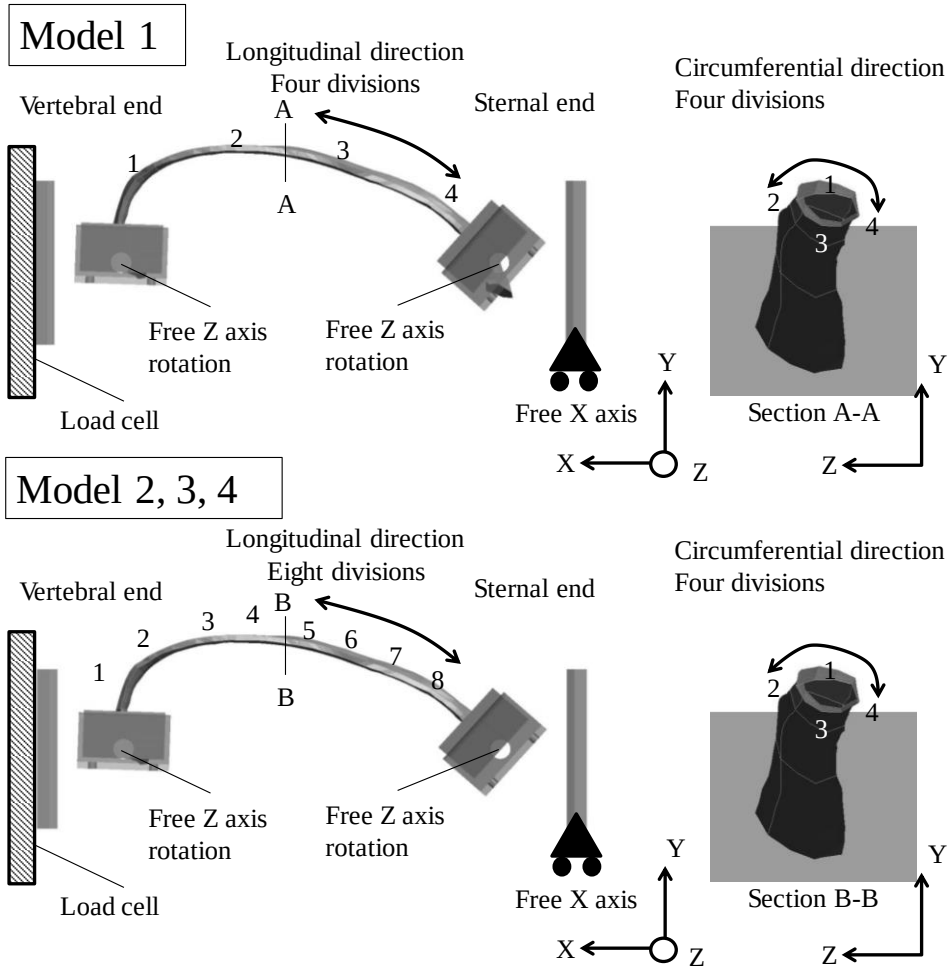

Figure 4. Bending test equivalent

Parametric Study – Method used to select the best model; As mentioned, the simulated reaction force time histories at the vertebral end of the rib were compared to the experimental data from Agnew et al [4]. The 4 versions of the model were evaluated both in terms of fracture reproducibility and force-displacement correspondence to determine the best method to model the whole-rib impact tests. The total energy, which was the total area under the force-displacement curve up to the time of fracture, was calculated and compared between each of the four parametric models and the experiment, and was used to evaluate the fracture accuracy. Also, the ratio of maximum force between simulation and experiment was used to evaluate the reaction force accuracy. Finally, the best modeling methodology was determined by averaging these two ratios. The average ratio closest to 1.0 indicated a good correlation between the simulation and the experiment.

Model Creation Phase (Determination of average material properties and cortical thicknesses for elderly female)

The representative material properties of the rib cortical bone for elderly female were determined using literatures. There are two human models for elderly female developed by Kalra et al. [20] and Iwamoto et al. [21] et al. They used the material properties for cortical thickness of rib as shown in Table 1A in Appendix. Our study used average material properties of two model. Young's modulus, Yield stress, Ultimate strain, and Ultimate stress were set by 11.1 GPa, 78.0 MPa and 0.022, respectively. The average cortical thickness was applied to median thickness value between two subjects of the bending test. Cortical thicknesses were used with average cortical thicknesses of two subjects as shown in Table.2A in Appendix. Average whole single rib were developed. Then, the average HBM were validated in next phase.

Model Validation Phase (Validation of whole rib bending test)

A whole-rib simulation test was validated using the rib bending test published by Agnew et al. [4] as detailed in the parametric methods section. The reaction force of the simulation was compared with the range of reaction forces documented in the experimental results. Simulation results were evaluated using the acronym of CORelation and Analysis (CORA) system. [22] The CORA rating is a method to evaluate the time-history signals, the reference curve (experimental result) and the predicted response (simulation result). CORA uses two methods to calculate the signals correlation: the corridor method calculates the deviation of the signal between two curves automatically created by the CORA software, while the cross-correlation method evaluates the characteristics of the signal such as phase shift, size, shape and progression. The total CORA score sums up the results of both metrics by using individual weighting factors from 0 to 1 for each metric. According to the rating stipulated in ISO/TR 18571 the resultants of the CORA score are classified into four categories: values above 0.94 are considered excellent, values between 0.94 and 0.8 are good, values between 08 and 0.58 are considered as a fair correlation and values below 0.58 are treated as a poor correlation.

Model Validation Phase (Validation of the HBM thorax in a side impact component test)

The evaluated whole-rib model was then applied to the full-body HBM for an elderly female. To validate the full-body HBM in a component level test, a lateral chest impact conducted by Talankinte et al. [23] was adopted to compare the thoracic impactor reaction force time histories. The thorax of the HBM was impacted in a lateral direction with a 150 mm diameter impactor, weighing 16 kg at a speed of approximately 6 m/s, matching the experimental conditions defined by Talankinte et al. [23] Only two female subjects (LCT02, LCT03) over 53 years old were tested in these experimental conditions. The geometric and inertial scaling method proposed by Mertz et al.[24] was performed on both subjects in order to better compare their results with the simulation. Force and time normalizing factors were calculated by Equations (2) and (5).

$$\mathrm{Rf} = (\mathrm{Rm}\ \mathrm{Rk})^{1/2} \qquad \text{(Equation 2)}$$

$$\mathrm{Rt} = (\mathrm{Rm})^{1/2}(\mathrm{Rk})^{1/2} \qquad \text{(Equation 3)}$$

where

$$\mathrm{Rm} = \mathrm{Ms}\ \mathrm{Mi}^{-1} \qquad \text{(Equation 4)}$$

$$\mathrm{Rk} = 308/L \qquad \text{(Equation 5)}$$

The mass ratio (Rm) was calculated using the total mass of the HBM (Ms), which was 47kg and the total mass of each experimental subject (Mi) as shown in equation 4. The stiffness ratio (Rk) uses a characteristic length ratio, in this scenario it is defined using chest width. Equation 8 defines RK to be the chest width of the 5th percentile elderly female HBM (308 mm) divided by chest width of each subject (L). Simulation results were then evaluated versus the experimental thoracic impacts using CORA as described in the validation of the whole-rib model.

Model Validation Phase (Validation of the HBM in a side impact sled test with realistic boundary conditions)
The published side impact sled tests with post mortem human subjects (PMHS) at an impact velocity of 28 km/h using a side airbag and simulating door intrusion (Shurtz et al.) [7] were simulated using the defined 5th percentile HBM. Comparisons between the simulation and the PMHS experiments were then conducted considering all of the following: spinal and pelvis kinematics, number of rib fractures and thoracic deflection from chest bands. The initial position of the HBM was set to match the experimental position data of each body segment and/or landmark including: head, sternal notch, olecranon and greater trochanter as shown in Figure. 5. The two PMHS responses were normalized to compare to the simulation responses using a length scale factor λz (seated height of the subjects) and a mass scale factor λm (total body mass). This normalization technique assumes equal density throughout each PMHS, so that the lateral displacement scale factor is defined by equation (6) proposed by Mertz et al.[25]

$$\lambda_y = Rm^{1/2}/\lambda z^{1/2} \qquad \text{(Equation 6)}$$

As with the whole-rib test and the thorax component test, the PMHS sled test simulation was evaluated using CORA. In addition, both the timing and location of the rib fractures predicted in the simulation were compared with those from the experimental results, when the fracture times were available in the PMHS tests.

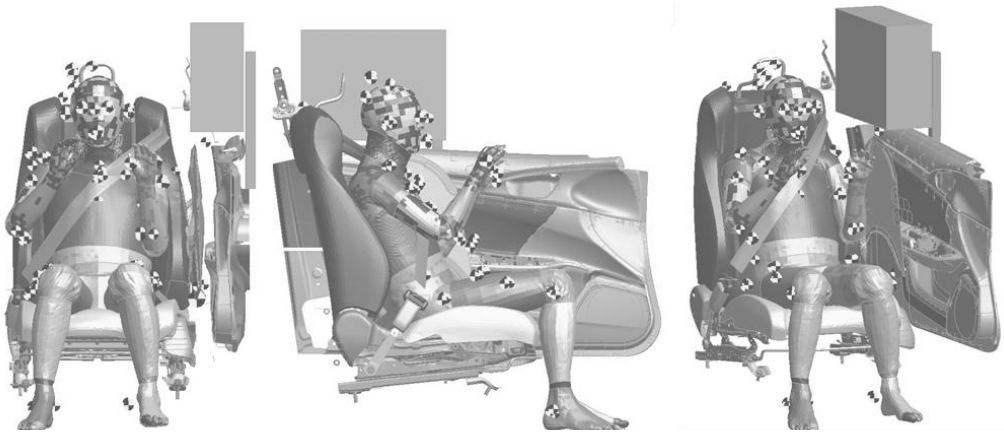

Figure 5. Comparison of seating position in the simulation with the experimental FARO data. Target mark indicates the experimental FARO data

RESULTS

Results of Parametric Study – Model Calibration
The parametric study parameters and evaluation results such as total energy ratio and max force ratio are shown in Table 4. The reaction force at the vertebral end of the rib is compared with the experimental data and shown in Figure 6. Based on the results, Model 4 appeared to be best represent the rib bending test given it has the values closest to 1.0 for both the total energy ratio and the max force ratio in this parametric study. Therefore, the modeling methodology for Model 4 was determined to be used for the validation phase of the models moving forward.

Table 4.
Parametric study matrix of bending simulation and results

		Case ID	Model 1	Model 2	Model 3	Model 4
Parameter		Number of divisions in the rib	16	32	32	32
		Thickness source	CT	CT	Function between Microscope and CT	Function between Microscope and CT
		Material properties	MAT24 Tension	MAT24 Tension	MAT24 Tension	MAT124 Tension & Compression
Evaluation	Subject1	Max force ratio	1.18	1.02	0.66	0.77
		Energy ratio	1.86	1.54	1.05	1.09
		Average ratio	1.52	1.28	0.86	0.93
	Subject2	Max force ratio	1.01	0.94	0.75	0.89
		Energy ratio	2.06	1.89	0.97	1.09
		Average ratio	1.54	1.42	0.86	0.99

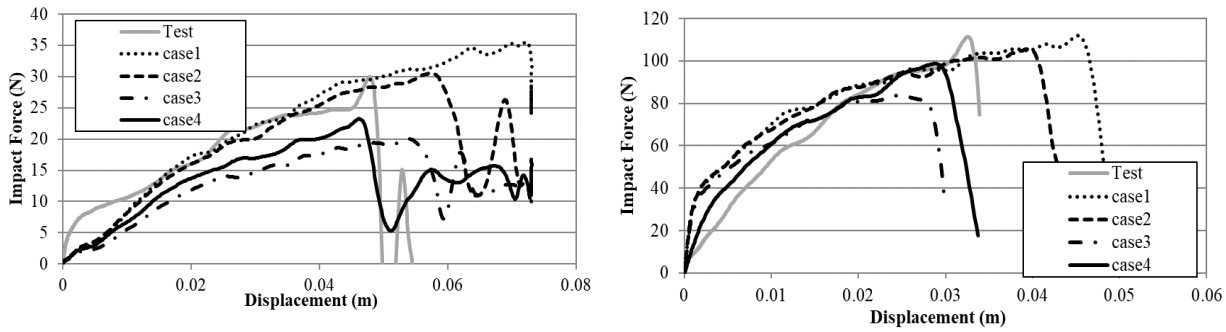

(A) (B)

Figure 6. Comparison of impactor force time history in parametric study ((A) subject1 results, (B) subject2 results)

Validation of Whole-Rib Model in Single Rib Bending Test

Figure 7 shows the comparison of the resulting force at the vertebral end of the whole rib and the total rib displacement between both experimental subject tests and the simulation with average material properties model. Peak force, which was 63 N was within the experiment results range of subject1 and subject2.

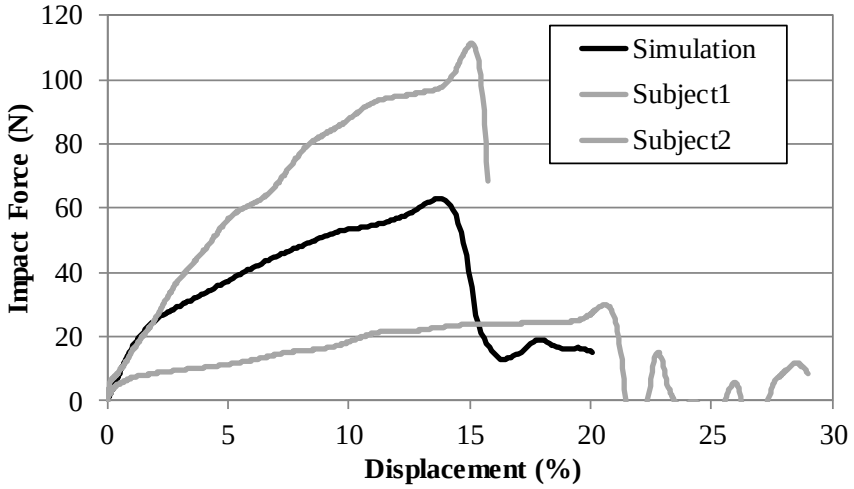

Figure 7. Comparison of bending impactor force displacement history in average rib model

Validation of Chest Side Impact Test

The modeling methodology for Model 4 was then applied to the thorax model of the HBM. Figure 8 shows the comparison of the chest impact force time history between the normalized experimental tests and simulation results. A standard deviation was calculated from the results of the normalized experiment results using two subjects. A CORA score of 0.885 is ranked "Good".

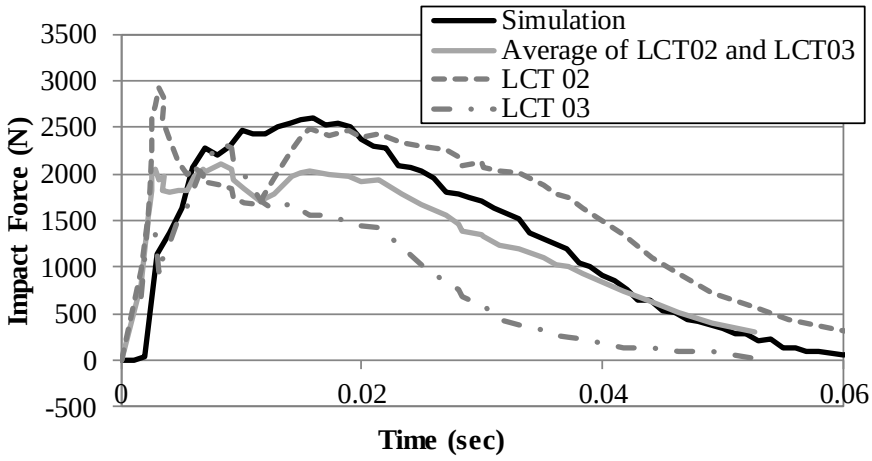

Figure 8. Comparison of impact force time history in simulation with the chest impact experiment

Validation of Side Impact Sled with Airbag

The seating position of the representative HBM showed good agreement with the experiential position point dataset as shown in Figure 5. Table 4 shows a summary of the CORA score regarding lateral displacement time histories of T1, T4, T12 and pelvis in the global coordinate system. The CORA score for lateral displacement indicates Excellent or Good, due to the range of CORA scores between 0.87-0.98. The lateral displacement time histories in the global coordinate system for each body region are also presented in Figures 9.

Table 4.
CORA Score and evaluation of lateral displacement at measurement points in sled test

Lateral displacement of body region	Corridor method	Correlation method	Total score
T1	0.99	0.89	0.95
T4	1.00	0.95	0.97
T12	1.00	0.97	0.98
Pelvis	0.86	0.87	0.87

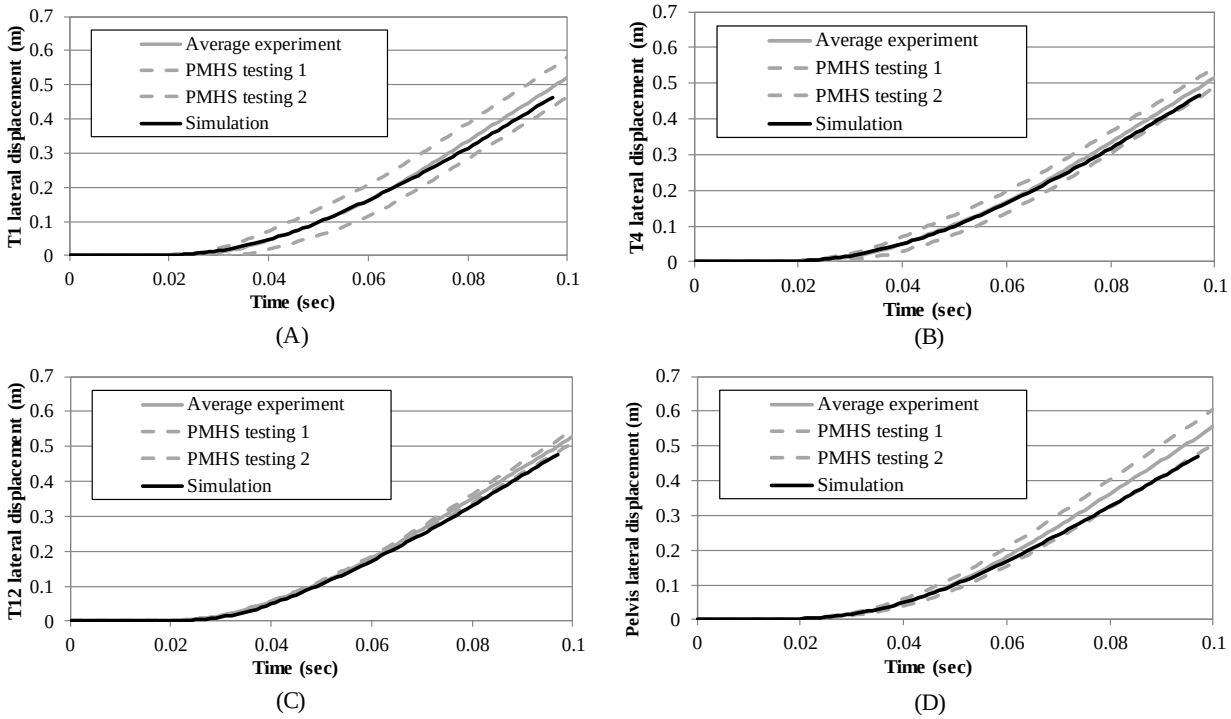

Figure 9. Comparison of lateral displacement of T1, T4, T12, and Pelvis between simulation and experiment ((A) T1 displacement, (B) T4 displacement, (C) T12 displacement, (D) Pelvis displacement)

Table. 5 shows the comparison between the fracture locations in the experiment with the simulation. In the simulation, shells of rib cortical bone were considered fractured when they reached 0.022 strain as defined by literatures. Fractures on the struck side occurred across the whole thorax, while fractures on the non-struck side occurred only in the upper and mid- thorax for both cases. The timing of rib fractures is also presented in Table 5. The first fracture occurred to the 7th anterior rib on the struck side of PMHS2 at 20 msec in both the experiment and

the simulation. Fractures on the non-struck side occurred later than fractures on the struck side. Thoracic deflection at the level of the axilla measured by the chestband were compared with the simulation results in both lateral and anterior-posterior (A/P) direction as shown in Figure 10. Maximum lateral thoracic deflection in the simulation and experiment were 14% and 15%, and both occurred at approximately 36 msec. Maximum anterior-posterior deflections were 5% and 6%, with both occurring approximately 19 msec.

Table 5.
Fractured rib location and timing in the sled test

Rib #	**PMHS1**		**PMHS2**		**Simulation**	
Fracture side	Struck	Non struck	Struck	Non struck	Struck	Non struck
Rib1						
Rib2	Fx:Ant(N/A)				Fx:Ant(28)	
Rib3	Fx:Ant(N/A)		Fx:Ant(26)	Fx:Ant(26)	Fx:Ant(23)	Fx:Ant(44)
Rib4	Fx:Ant(N/A)	Fx:Ant(47)	Fx:Ant,Post(27)	Fx:Ant(31)	Fx:Ant(28)	
Rib5			Fx:Ant.Post(21)	Fx:Ant(38)	Fx:Ant(44)	Fx:Ant(46)
Rib6	Fx:Ant(39)		Fx:Ant,Post(20)	Fx:Ant(39)	Fx:Ant(22)	
Rib7			Fx:Ant,Post(19)	Fx:Ant(N/A)	Fx:Ant(20)	
Rib8			Fx:Post(29)		Fx:Ant(28)	
Rib9					Fx:Ant(22)	
Rib10					Fx:Ant(20)	
Total number of fractured ribs	4	1	6	5	9	2

Fx=fracture, Ant=anterior, Post=posterior, ( ) = time of fracture msec, N/A= unknown

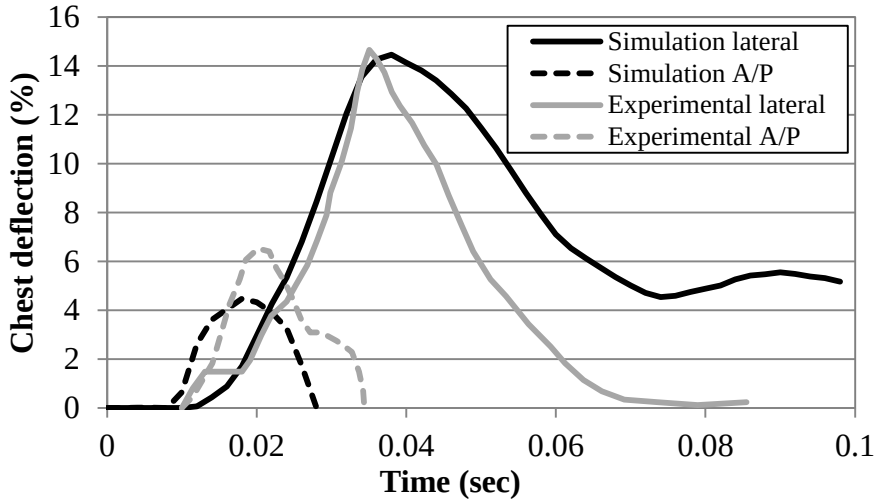

Figure 10. Comparison of thoracic deflection at the level of the axilla in side impact sled tests

DISCUSSION

In the parametric study, model 4 was more accurate than the other models for both subjects. It was found that number of rib divisions, thickness and material properties were significant parameters to predict rib fracture. Maximum force ratios were not effected in the parametric study. On the other hand, energy ratios were significantly effected in this parametric study. Therefore, these parameters were crucial to predict rib fractures, which means strain distribution of the rib were changed. As shown in Figure 11, increasing the number of rib divisions (Model 2) leads to more accurate energy ratios compared to in Model1. Similarly, Li et al. [26] found that use of variable cortical thickness distribution slightly decreased the failure displacement compared to the mode with constant cortical thickness. A more realistic cortical thickness distribution was crucial to predict the rib strain distribution.

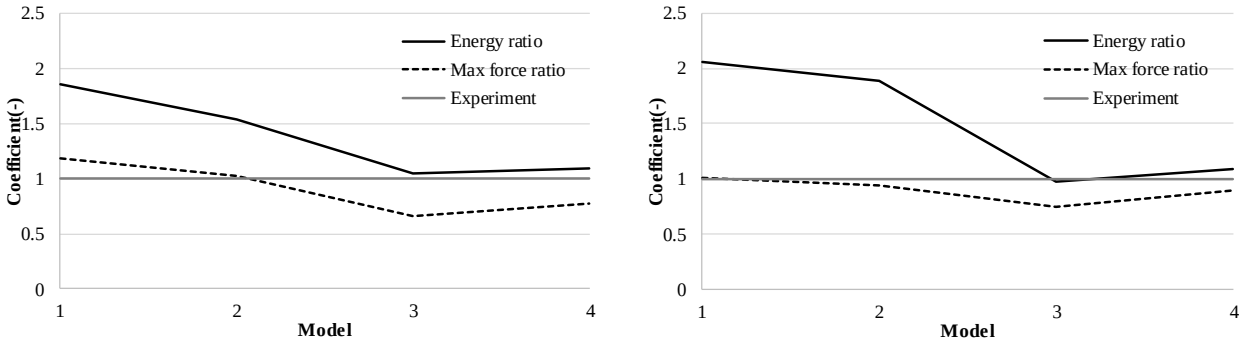

Figure 11. Comparison of max force ratio and energy ratio in parametric study ((A) subject1 results, (B) subject2 results)

Cortical thickness from the function between CT and histological measurement (Model 3) was more precise than both Model 1 and 2 in terms of energy ratio as shown in Figure 12. Actually, cortical thickness from histological measurement had a range of 0.14mm - 0.97mm. Because thresholding was used to reconstruct CT scans, cortical thickness from CT may overestimate the rib cortical thickness as can be seen in Table 2. Then rib strain may decrease so that the energy ratio was greater than the experiment. In a previous study, Perz et al. [27] found that utilizing CT images to result in greater than 100% error in cortical thickness. That difference of thickness affected mechanical response under antero-posterior loading to a single whole rib. In addition, Li et al also suggested that using for cortical thickness from a high-resolution CT data such as a micro CT would improve predicted fracture location. [26] Therefore, the resolution of the image based on cortical thickness is significant parameter for predicting rib fractures.

Considering compression (Model 4) helps to be more accuracy in this study. Kemper et al. found that cortical bone in the tibia has tension/compression asymmetry when looking at the stress-strain properties [11]. Fertschej et al. got more accuracy considering not only tension, but also additional properties (compression and shear, etc.) in the 3 point bending test using thermoplastics. [28] Shell strains-time history on the superior and inferior aspects of a middle of the rib in model 4 of parametric study were compared with those in model 3 as shown in Figure 12. Shell strain on the superior aspect of the rib in Model 4 was increasing earlier than in Model 3. Considering material asymmetry (Model 4), tensile strain distribution on the superior shell is higher than the symmetry material (Model 3) due to less the compression strain. Therefore, it is assumed strain distribution of the rib was changed when considering the compression property. It leads to be more accuracy.

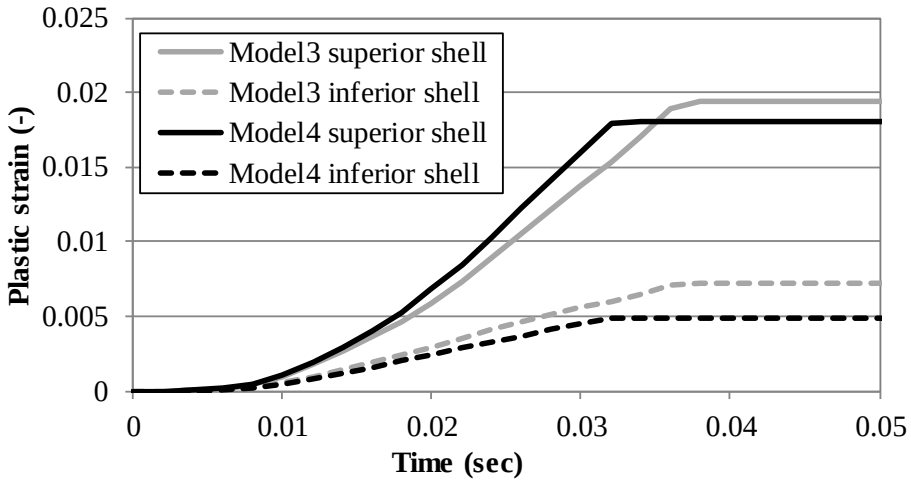

Figure 12. Comparison of plastic strain of the rib during the bending test (superior portion; inferior portion)

Regarding the whole-rib simulation validation results, the results were compared with the literature published by Agnew et al. [4] The experimental study showed peak force and peak displacement % were predicted using the following equations:

Peak force for female: FPeak = 133.58 - 0.950*Age (Equation 7)

Peak displacement for female: δPeak = 42.26 - 0.2724*Age (Equation 8)

If we assume an age of 75 years old was used for the simulation, the resulting Fpeak and δPeak would be 62.3 N and 21.3% respectively. The Average simulation results shows 68.5 N and 14% respectively, which reveal this rib model could be representative of a 75 years old of female.

This HBM showed fairly good agreement with the experiment results. A CORA score of kinematic response in the HBM is approximately 1.0, ranking Excellent. In addition, the location and timing of the fractured ribs in the simulation were compared with the experimental results. Fractures in both struck and non-struck side occurred in both simulation and in the experiments. Therefore, the simulation predicted not only the number of fractures, but also the fracture location using the deterministic method. However, humans have individual differences such as body type and varying material properties, so it should be further investigated to predict rib fractures using the probabilistic method.

CONCLUSION

The improved model for rib cortical bone was developed using thirty-two divisions of each rib, a cortical bone thickness value estimated from histological data, and material properties considering tension and compression.

The HBM developed by applying rib material properties along with geometrical scaling for an elderly female well represented the upper body kinematics, rib fractures and thoracic deflection in a side impact sled test from a published PMHS experiment.

ACKNOWLEDGEMENTS

Authors would like to grateful acknowledgement Dr. Jingwen Hu from University of Michigan Transportation Research Institute Department of Mechanical Engineering, University of Michigan (UMTRI), and Dr. Andrew Kemper from Virginia Tech-Wake Forest University for supporting their data through this study.

REFERENCES

[1] NHTSA-National Highway Traffic Safety Administration., 2017. “Traffic Safety Facts 2015.” DOT HS 812 372: 1-5

[2] Ortman, M., Jennife, R., Velkoff, V., Hongan, H., 2014. “An Aging Nation: The Older Population in the United States. Current Population Reports.”: 25-1140

[3] NHTSA-National Highway Traffic Safety Administration., 2005. “Characteristics of Crash Injuries Among Young, Middle-Aged, and Older Drivers.” DOT HS 810 857: 44-45

[4] Agnew, A., Murach, M., Dominguez, V., Sreedhar, A., Misicka, E., Harden, A., Bolte, J., Kang, Y., Stammen, J., Moorhouse, K., 2018.” Sources of Variability in Structural Bending Response of Pediatric and Adult Human Ribs in Dynamic Frontal Impacts.” Stapp Car Crash Journal, Vol.62, November: 119-192.

[5] Agnew, A., Murach, M., Misscka, E., Moorhouse, K., Bolte, J., Kang, Y., 2017. “The Effect of Body Size on Adult Human Rib Structural Properties.” In Proceedings of the IRCOBI Conference (Antwerp, Belgium, Sep. 11-13)

[6] Ramachandra, R., Kashikar, T., Bolte, J., 2017. “Injury Pattern of Elderly Occupants Involved in Side Crashes.” In Proceedings of the IRCOBI Conference (Antwerp, Belgium, Sep. 11-13)

[7] Shurtz, B., Agnew, A., Kang, Y., Bolte, J., 2018. “Application of Scaled Deflection Injury Criteria to Two Small, Fragile Female in Side Impact Motor Vehicle Crashes.” SAE International Technical Paper, April: 2018-01-0542

[8] Jin, X., Kalra, A., Hammad, A., Khandelwal, P., Porwal, V., Shen, M., Yang, K., 2018. “Development and Validation of Whole-Body Finite Element Occupant and Pedestrian Models of a 70-Year-Old Female” In Proceedings of the IRCOBI Conference (Athens, Greece, Sep. 12-14)

[9] Dokko, Y., Yanaoka, T., Ohashi, K., 2013. “Validation of Age-Specific Human FE Models for Lateral Impact.“ SAE International Technical Paper: 2013-01-1242.

[10] Kemper, A., McNally, C., Kennedy, E., Manoogian, S., Rath, A., Ng, T., Stitzel, J., Smith, E., Duma, S., Matsuoka, F., 2005. “Material Properties of Human Rib Cortical Bone from Dynamic Tension Coupon Testing.” Stapp Car Crash Journal, Vol.49, November: 199-230.

[11] Kemper, A., McNally, C., Kennedy, E., Manoogian, S., Duma, S., 2007. “The Material Properties Of Human Tibia Cortical Bone In Tension And Compression: Implacations For The Tibia Index.” In proceeding of International Technical Conference on the Enhanced Safety of Vehicles Conference (ESV) (Lyon, France, June. 18-21)

[12] ISO/TC22/SC12/WG5., 1997. “Road Vehicles - Anthropomorphic Side Impact Dummy – Lateral Impact Response Requirements to Assess the Biofidelity of the Dummy.” Document N455-Revision 4

[13] Lessley, D., Shaw, G., Parent, D., Arregui-Dalmases, C., Kindig, M., Riley, P., et al. 2010. “Whole-Body Response to Pure Lateral Impact.” Stapp Car Crash Journal, Vol.54: 289-336

[14] Shaw, G., Parent, D., Purtsezov, S., Kerrigan, J., Shin, J., Crandall, J., Zama, Y., Ejima, S., Kamiji, K., Yasuki, T., 2009. “Frontal Impact PMHS Sled Tests for FE Torso Model Development.” In Proceedings of IRCOBI Conference (York, United Kingdom, Sep. 9-11)

[15] Rhule, H., Maltese, M., Donnelly, B., Eppinger, R., Brunner, J., Bolte, J., 2002. “Development of a New Biofidelity Ranking System for Anthropomorphic Test Devices.” Stapp Car Crash Journal. Vol 46: 477-512

[16] Robbin, D., 1983. “Anthropometric Specifications For Small Female And Large Male Dummy, Volume3.” FINAL REPORT Oct: UMTRI-83-53-3

[17] Wang, Y., Cao, L., Bai, Z., Reed, M. Rupp, J., Hoff, C., Hu, J., 2016. "A Parametric Ribcage Geometry Model Accounting for Variations Among the Adult Population." Journal of Biomechanics. Vol 49: 2791-2798

[18] Albert, D., Kang, Y., Agnew, A., Kemper, A., 2017. "A Comparison of Rib Structural and Material Properties from Matched Whole Rib Bending and Tension Coupon Tests." In Proceedings of the 2017 IRCOBI Conference (Antwerp, Belgium, Sep. 11-13)

[19] Takahashi, Y., Kikuchi, Y., Konosu, A., Ishikawa, H., 2000. "Development and Validation of the Finite Element Model for the Human Lower Limb of Pedestrians." Stapp Car Crash Journal. Vol 44: 2000-01-SC22

[20] Kalra, A., 2017 "Development of an Elderly Female Torso Finite Element Model for Restraint System Research and Development Applications." Doctoral thesis. Wayne State University.

[21] Iwamoto, M., Nakahira, Y., Kimpara, H., Min, K., 2013. "Development of a Finite Element Model of 5th Percentile Female with Multiple Muscles and Its Application to Investigation on Impact Responses of Elderly Females." In Proceeding of the 23rd International Technical Conference on the Enhanced Safety of Vehicles (ESV) (Seoul, Republic of Korea, May 27-30)

[22] Gehre, C., Gades, H., Wernicke, P., 2009. "Objective Rating of Signals Using Test and Simulation Responses." In Proceedings of the 21st International Technical Conference on the Enhanced Safety of Vehicles Conference (ESV) (Stuttgart, Germany, June. 15-18)

[23] Talantikite, Y., Bouquet, R., Ramet, M., Guillemot, H., Robin, S., Voiglio, E., 1998. "Human Thorax Behaviour for Side Impact: Influence of Impact Masses and Velocities." In Proceedings of International Technical Conference on the Enhanced Safety of Vehicles Conference (ESV) (Ontario, Canada, May31-June 4)

[24] Mertz, H., 1984. "A Procedure for Normalizing Impact Response Data." In Proceedings of SAE International Congress and Exposition.: 840884

[25] Mertz, H., Irwin, A., Melvin, J., Stalnaker, R., Beebe, M., 1989. "Size, Weight and Biomechanical Impact Response Requirements for Adult Size Small Female and Large Male Dummies in Automotive Frontal Impacts." SAE, Warrendale, PA, : 133-144

[26] Li, Z., Kindig, M., Subit, D., Kent, R., 2010. "Influence of Mesh Density, Cortical Thickness and Material Properties on Human Rib Fracture Prediction." Medical Engineering & Physics, Vol 32, November: 998–1008

[27] Perz, R., Toczyski, J., Subit, D., 2015. "Variation in the Human Ribs Geometrical Properties and Mechanical Response Based on X-ray Computed Tomography Images Resolution." Journal of the Mechanical Behavior of Biomedical Materials. Volume 41, January: 292-301

[28] Reithofer, P., Fertschej, A., Hirschmann, B., Jilka, B., Rollant M., 2018. "Material Models for Thermoplastics in LS-DYNA from Deformation to Failure." In Proceedings of International LS-DYNA User Conference (Michigan, United states, June 11-12)

APPENDIX

Table 1A.
Average rib cortical material properties for elderly female

Data source	Young Modulus [GPa]	Yield Stress [MPa]	Ultimate Strain [-]
This study (Average)	11.1	78.0	0.022
Kalra et al.	7.3	54.0	-
Kimpara et al.	14.8	101.9	0.022

Table 2A.
Cortical thickness measurement calculated to histological measurement from CT

	Thickness source	5%	13%	25%	38%	50%	67%	75%	88%
Subject 1	Superior cortex (mm)	2.18	1.44	1.80	0.56	0.44	0.24	0.49	0.41
	Outer cortex (mm)	1.94	1.49	0.90	0.49	0.29	0.36	0.46	0.44
	Inferior cortex (mm)	2.55	1.47	1.23	1.78	0.75	0.20	0.49	0.51
	Inner cortex (mm)	0.87	0.94	1.44	1.10	0.99	0.60	0.41	0.39
Subject 2	Superior cortex (mm)	0.41	1.59	0.92	1.35	1.15	0.14	0.54	0.39
	Outer cortex (mm)	1.28	0.28	1.46	1.35	0.61	0.14	0.38	0.49
	Inferior cortex (mm)	1.86	1.39	1.63	1.77	1.30	0.92	1.20	0.39
	Inner cortex (mm)	1.28	0.28	1.46	1.35	0.61	0.14	0.38	0.49
Average	Superior cortex (mm)	1.29	1.52	1.36	0.95	0.80	0.19	0.52	0.40
	Outer cortex (mm)	1.90	1.44	1.26	1.13	0.80	0.64	0.83	0.42
	Inferior cortex (mm)	1.91	0.88	1.34	1.57	0.68	0.17	0.43	0.50
	Inner cortex (mm)	1.26	1.26	1.87	1.74	1.32	0.87	0.88	0.44

DEVELOPMENT OF A HYBRID MUSCLE CONTROLLER FOR AN ACTIVE FINITE ELEMENT HUMAN BODY MODEL IN LS-DYNA CAPABLE OF OCCUPANT KINEMATICS PREDICTION IN FRONTAL AND LATERAL MANEUVERS

Oleksandr V. Martynenko
Fabian T. Neininger
Syn Schmitt
Institute for Modelling and Simulation of Biomechanical Systems,
Stuttgart Research Center for Simulation Sciences, University of Stuttgart
Germany

Paper Number 19-000215

ABSTRACT

Automotive safety has made a definite shift towards the continually increasing use of active safety systems in standard and highly automated vehicles (HAV) with a crucial need for the development of tools to supplement the assessment of such systems. Finite Element Human Body Models (FE HBMs) emerge as an innovative pre-requisite for this process in a virtual toolchain. Traditional passive HBMs were developed for in-crash simulations and are not suitable for straightforward use in the pre-crash phase because of inappropriate soft tissues response in low gravity scenarios and the absence of active muscle elements with a proper controller.

The current contribution covers some transformation issues from passive to active behavior for HBM and focuses on the development of a physiologically motivated controller for the whole HBM utilizing standard LS-DYNA keywords. The controller operates with the contraction dynamics of *MAT_MUSCLE material (also referenced as *MAT_156) through Hatze's activation dynamics and is capable of resembling a valid occupant response during maneuvers.

The proposed neural control model is a form of intermittent control and based on the assumption that the central nervous system governs the controlled motion through shifting between particular states of the musculoskeletal system – so-called "equilibrium points", where equilibrium of all acting external and internal forces is presumed for a resulting desired position. A hybrid formulation of the controller allows for taking closed-loop muscle stimulation (target muscle lengths "λ") as well as open-loop stimulation ("α") into account.

Previous to the whole body application, the equilibrium point hybrid controller (EPHC) approach was validated separately for some parts of the body only. Posture control capability was investigated by tracking motion speed, maximum muscles activation level and the effect of co-contraction. Subsequently, the full HBM simulations were carried out for lane change and 1g braking scenarios retrieved from the experimental database of the Occupant Model for Integrated Safety Project (OM4IS). A modified Total HUman Model for Safety (THUMS) model was correlated to a matched size volunteer with the comparison of head and torso excursions to appropriate experimental corridors.

Each single body region model was validated with in vivo kinematics and dynamics enabling an integration of the single body parts into the entire HBM. Measured maximal deviations for the whole HBM reside within the experimental corridors and correlate well with the volunteer.

The proposed approach permits modeling of active and reactive human responses with the help of an existing passive FE HBM after adequate adaptation of the model, muscle elements insertion and controller parameters tuning. Such model paves the way for the evaluation of new HAV interior concepts and the development of advanced vehicle safety systems.

INTRODUCTION

Crash tests with anthropometric test devices were historically inevitable for the design and test of automotive safety systems. However, stunningly fast development in simulation technologies not only increased computational power and simulation speed but also led to better, more valid digital models for studying the crash scenarios. The idea of using virtual human body models (HBM) emerged as a consequence of such advances realizing the benefits of virtual tests with higher biofidelity, compared to the commonly used virtual dummy models. Today, HBMs provide a vast application field in automotive safety system development, more and more penetrating from the in-crash phase studies into the pre-crash considering active human behavior, e.g., reflexes and simple movements.

As the primary simulation method nowadays in the automotive industry is the finite element (FE) analysis, regularly used state-of-the-art HBMs were implemented applying FE tools and validated for in-crash scenarios, basing mostly on the cadaver studies implying high loads during impact. Accordingly, such models are passive by their nature and are not suitable for straightforward application in the pre-crash phase for two main reasons: inadequate soft tissue response in low g scenarios and absence of active muscle elements with appropriate biological muscle controller. We hypothesize that it is possible to simulate active and realistic human motion with the currently available human body models after accurately solving these issues.

It is proven that muscle activity has a significant impact on the occupant kinematics during typical pre-crash events including braking or evasive maneuvers [1-3]. In recent years, there has been an increasing amount of literature on the aHBM development using different types of models and implementing different muscle activation strategies [4]. However, the number of the existing whole body FE aHBMs is still limited. THUMS v.5 model with a proportional-integral-derivative (PID) muscle controller including two controls for 16 three-dimensional joint angles and two reaction forces from a steering wheel and pedals was introduced in [5]. SAFER A-HBM model [6], which is based on the earlier THUMS v.3 [7], uses similar PID feedback controllers, but limited to seven relative angles between body parts. In contrast to mentioned models, λ-controller was adopted in reactive THUMS-VW model [8] to control around 600 muscles governed by 66 separate controllers. Despite the long development process and validation with many test cases these models still have some drawbacks in simulations of the whole crash sequence, with the main reason being lack of the omni-directionality. Consequently, there is a clear need for further developments of whole body aHBM with omni-directional controllers capable of combined maneuvers simulations.

The purpose of this study is the application of the macroscopic Hill-type [9] muscle modeling approach to activate a modified FE HBM also based on the THUMS v.3 [7]. Currently, such models reveal high joint and tissue stiffnesses which first have to be reduced. Henceforth this model was used with the aim to perform a simulation predicting occupant kinematics behavior according to the experimental data from the Occupant Model for Integrated Safety (OM4IS) project [1]. The hybrid equilibrium point controller (hybrid controller) proposed in [10] was adopted as a muscle control strategy including physiological Hatze's activation dynamics [11] interacting with contraction dynamics from the *MAT_MUSCLE in LS-DYNA R7.1.3 software [12]. All functions serving the controller needs were implemented inside LS-DYNA utilizing standard keywords to increase industrialization possibilities.

METHODS

Adaptation of the soft tissue response

One of the main prerequisites for active human body models (aHBM) is an adequate soft tissue response in low g load scenarios which are predominant in the pre-crash phase. As mentioned above, passive HBMs are found to be excessively stiff. Thus, 50^{th} percentile average occupant THUMS v.3 model was modified according to the procedure described in details in [13] to reproduce passive "relaxed" human occupant behavior with not active muscle elements included to fit experimental corridors given in [1]. According to the given study, "relaxed" state means fitting the corridor defined by displacement of the head center of gravity (CG) from volunteers with minimal muscle activity during 1 g braking loading pulse. The model adaptation includes mesh refinement in several body regions, a modification of connections between skin and some other parts, and the revision of the elastic modulus for specific soft tissues within physiological limits given in the literature.

Implementation of the biological muscle controller

Hybrid Equilibrium Point Controller: The neural control model used in this contribution is a form of intermittent control [14]. It is based on the assumption, that the controlled motion is governed by the central nervous system (CNS) through shifting between individual states of the musculoskeletal system (so-called "equilibrium points", EPs). In such an EP the equilibrium of external and internal forces acting on the body is reached resulting in the desired body posture. For the hybrid EP control approach [10,15], the motor command consists of two terms:

λ part – closed-loop feedback controller signal: Is based on the control of each of the body muscles target lengths. It could be known to the CNS by mapping of joint angles to associated muscles and could be stored in the memory as the magnitude of a respective signal from muscle spindles and Golgi tendon organs and obtained through learning process during an ontogenesis [16,17].

α part – open-loop feedforward controller signal: Could be generated directly by the CNS to compensate existing external loads, to hold the desired body posture or to reach a certain position in a specific manner, e.g. very fast, and could be governed via visual feedback or other internal sensors not directly associated with the muscle itself [18].

Herewith, the total neuronal stimulation signal from the CNS could be defined mathematically as a combination of the closed-loop signal and open-loop signal (Equation 1). Signal values are varying inside the interval [0...1], where "0" is no muscle stimulation at all and "1" is a fully stimulated muscle. It should be noted here, that full stimulation is a theoretical upper limit, and maximum voluntary stimulation is below "1".

$$u_{hybrid}^{total}\Big|_0^1 = u_{\lambda}^{closed} + u_{\alpha}^{open} \qquad \text{(Equation 1)}$$

To simplify the use of this method in industrial applications and to allow for intuitive and easy handling, the controller code was implemented within LS-DYNA software using standard keywords *DEFINE _FUNCTION, *DEFINE_CURVE and *DEFINE_CURVE_FUNCTION in combination with C programming language for missing functionality. Since LS-DYNA provides no capabilities presently to solve user specified differential equations directly inside the program code, a prescribed velocity of the specially created nodes (*BOUNDARY_PRESCRIBED_MOTION keyword) was used for retaining old variable values from the previous load step, which are needed for numerical integration over time and muscle neural delay implementation. A flowchart of the controller logic and its incorporation in combination with the LS-DYNA muscle material model *MAT_MUSCLE is presented in Figure 1, where α represents the open-loop part of the controller signal, and not the α motor neuron signals. Other corresponding symbols could be found in Table 1.

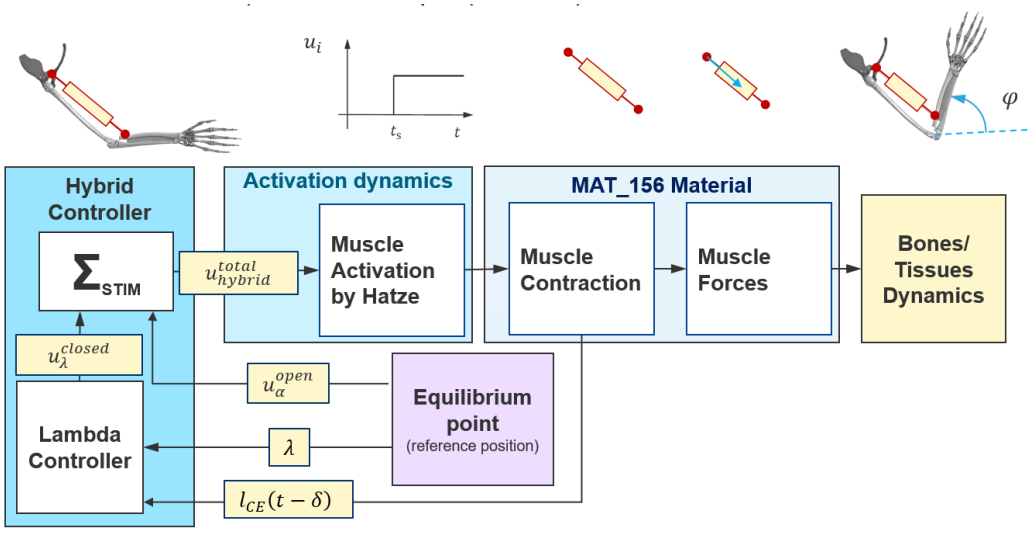

Figure 1. Flowchart of the muscle controller code shown for the single muscle element only.

As seen from the given chart, the implemented controller uses delayed actual muscle length value $l_{CE}(t-\delta)$ as a feedback signal compared to the target length of the muscle λ and a predefined stimulation u_{α}^{open} as a feedforward signal. Both inputted values of λ and u_{α}^{open} are defined by the equilibrium point (reference position) given in the simulation time and were retrieved from existing experimental data [1] a priori to simulation runtime.

Muscle length signal has a delay due to the time of sensory impulse traveling from muscle spindle through the nerve to the control center and back. The muscle spindle belongs to the group of proprioceptors and corresponds to the organ of perception inside the muscle belly. This organ has the functionality similar to a closed-loop PD-controller because muscle tissue itself shows visco-elastic behavior [10]. Thus, the equation of the λ-controller part could be written in the following form (Equation 2) with the corresponding symbols shown in Table 1.

$$u_{\lambda}^{closed}\Big|_0^1 = \frac{k_p}{l_{CEopt}} \cdot [l_{CE}(t-\delta) - \lambda] + \frac{k_d}{l_{CEopt}} \cdot v_{CE}(t-\delta) \qquad \text{(Equation 2)}$$

From the given relation it is evident that deviations in targeted and actual muscle lengths in connection with the contraction speed result in increased muscle stimulation. The main advantage of λ-control is that the forces needed to reach a target position are calculated during the motion, and no inverse problem has to be solved. Thus, switching between different intermediate postures during simulation time is done by changing the muscle's target lengths without any modifications in the controller code. This allows intuitive and easy handling in industrial applications.

Table 1.
List of the Parameters and Corresponding Symbols Used Within the Controller Code

Symbol	Parameter Definition	Value
t	Current simulation time	Calculated in runtime
δ	Neural delay of the muscle signal	Preset value
v_{CE}	Contraction velocity of the contractile element (muscle fiber)	Calculated in runtime
l_{CE}	Actual length of the contractile element (muscle fiber)	Calculated in runtime
l_{CEopt}	Optimal length of the contractile element (muscle fiber)	Preset value
λ	Target length of the muscle	Preset value
k_p	Proportional controller gain	Preset value
k_d	Differential controller gain	Preset value
γ	Free calcium ion concentration in the muscle	Calculated in runtime
$\dot{\gamma}$	Time derivative of free calcium ion concentration	Calculated in runtime
γ_{min}	Initial calcium ion concentration	Preset value
u_{hybrid}^{total}	Total muscle stimulation level from the controller	Calculated in runtime
u_{λ}^{closed}	Stimulation signal from closed-loop feedback controller part	Preset value
u_{α}^{open}	Stimulation signal from open-loop feedforward controller part	Preset value
a	Muscle activation level or activity	Calculated in runtime
a_{min}	Minimal muscle activation level	Preset value

Activation Dynamics: Physiological muscle activation dynamics introduced in [11] is used for a transfer of the total stimulation signal u_{hybrid}^{total} from the Hybrid controller into muscle activation level a, which could be directly inputted as a constant value or a continuous function (load curve) to LS-DYNA material *MAT_MUSCLE. The activation signal is calculated in the controller code in two steps: 1) the free calcium ion concentration is calculated by an integration of a first-order differential Equation 3 with an explicit Euler scheme (Equation 4); 2) this result is fed afterwards in an Equation 5 to calculate the resulting muscle activation with relation to renormalized factor for length dependency.

$$\dot{\gamma} = m \cdot (u - \gamma) \qquad \text{(Equation 3)}$$

where $m = 0.01\ (1/ms)$ – Hatze's activation frequency constant.

$$\gamma_{n+1} = \gamma_n + \dot{\gamma}_n \cdot dt \quad \text{(Equation 4)}$$

taking into account $\gamma(0) = \gamma_{min}$.

$$a(t) = \frac{a_{min} + [\rho(l_{CErel}) \cdot \gamma(t)]^{\nu}}{1 + [\rho(l_{CErel}) \cdot \gamma(t)]^{\nu}} \quad \text{(Equation 5)}$$

where $\rho(l_{CErel}) = \rho_c \cdot \frac{l_\rho - 1}{l_\rho / l_{CErel} - 1}$ is Hatze's length dependency function with respective constants $\rho_c = 9.10$, $l_\rho = 2.9$ and $\nu = 2.0$ taken from [19].

Contraction Dynamics: The muscle's contraction dynamics is incorporated into LS-DYNA material *MAT_MUSCLE [12] and generates active force from contractile element according to the law shown in the Equation 6.

$$F_{CE} = \sigma_{max} \cdot a(t) \cdot f_l(l) \cdot f_v(v) \quad \text{(Equation 6)}$$

where σ_{max} – is a generated peak stress for the muscle, $a(t)$ – is a muscle activation level calculated in the Equation 5, $f_l(l)$ – is a force-length relation in the exponential form taken from [15] and $f_v(v)$ – is a force-velocity relation in a hyperbolic form also from [15] (Figure 2). Additionally, the force generated by the muscle finite element is influenced by passive and damping components. The values of generic parameters used in *MAT_MUSCLE for all muscles along with appropriate references are reported in Table 2 below.

Table 2.
Generic Muscle Parameters for LS-DYNA Material *MAT_MUSCLE

Parameter	Description	Value (units)	Source
PIS	Peak Isometric Stress	0.001 (GPa)	[20]
SRM	Maximum Strain Rate	0.005 (ms-1)For Hand muscles	[21]
		0.0022 (ms-1) For Torso and Neck muscles	[21]
SVS	Force-Length Relation	Load curve Input	[15]
SVR	Force-Velocity Relation	Load Curve Input	[15]
SSP	Stress vs. the Stretch Ratio	Load Curve Input	[15]

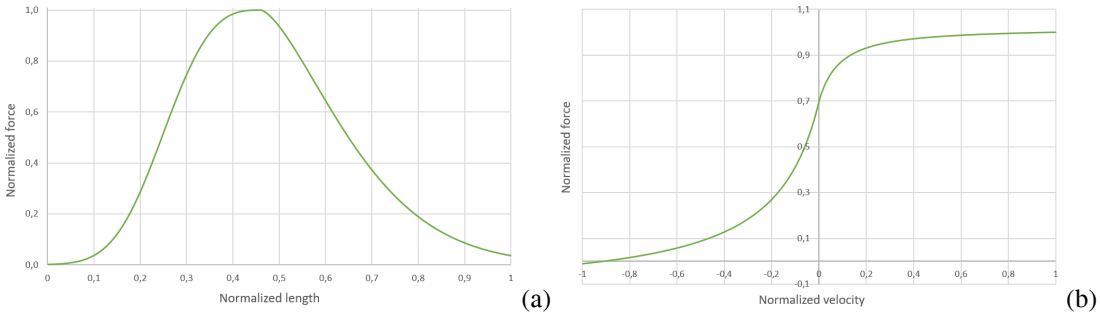

(a) (b)

Figure 2. Force-length (a) and force-velocity (b) relations used for all muscles according to [15].

Insertion of the muscle elements into the HBM

About 370 muscles from the human body were added subsequently into aHBM for the current study. Among them: 180 muscles were added to the neck, 150 – to the thoracic region and 40 – to upper extremities. All these muscles are represented by one-dimensional truss elements (*ELEMENT_BEAM, formulation ELFORM=3) with assigned material *MAT_MUSCLE. In order to give them the necessary anatomical and physiological properties such as origin and insertion nodes, optimal muscle length and physiological cross-sectional area (PCSA), these values were obtained from complementary literature sources [22-25].

Occupant Model for Integrated Safety Project Experimental Data

OM4IS project major objective was to gather a comprehensive collection of vehicle and occupant kinematic data based on results from human volunteers seated in the passenger position undergoing different driving maneuvers. Among them were emergency braking from two different speeds, lane change maneuvers to both sides and combined ones. This data was published in several sources prior to our study and represents an excellent base for the aHBM validation. Load□case results for emergency braking from 50 km/h and lane change, where a combination of lateral and frontal accelerations occurred, given in [1] are used in this contribution to validate the whole body model.

RESULTS

Validation at the body region level

To validate the proposed hybrid controller a simple multibody musculoskeletal model similar to the one proposed in [10] was built. This model consists of three rigid bodies including bones and eight truss elements representing muscles (4 flexors and 3 extensors) which actuate the elbow joint. The elbow flexion movement from 45deg to 145deg was simulated according to the given test set-up. This experimental source was taken because it offers a clear test setup, which is easy to reproduce in a simulation environment. Additionally, only one joint is actuated which allows a fine-tuning of the controller parameters. The resultant model was retrieved from THUMS model [7] by separating the bone parts and adding a revolute joint for the elbow with the stiffness of 0.6 kN·mm/rad specified according to [21] (Figure 3). A physiological muscle routing was not implemented, hence a supplementary rigid beam with the total length of 20mm was connected to the ulna bone to enable the triceps muscle elements connection.

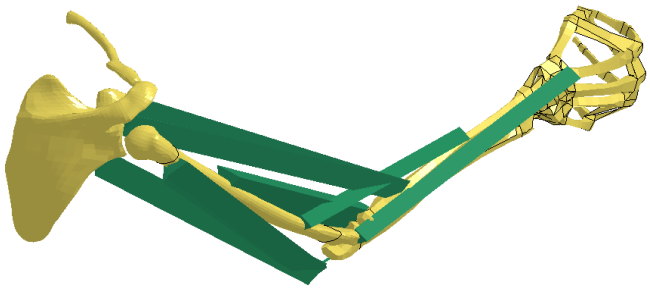

Figure 3. Multibody arm model with inserted muscles.

The structure of the hybrid controller includes feedforward and feedback components. Therefore, input signals for both have to be set.

Deriving control signals for the feedforward α part: Open-loop stimulation signal is governed directly by the CNS to switch between EPs and in current study intended mainly to hold the position or to compensate existing external loads by the muscle co-contraction. By definition, the static equilibrium is considered in any of the EPs resulting in constancy of the angular velocity and acceleration which should be equal to zero [15] (Equation 7).

$$\dot{\varphi}_i = 0 \text{ and } \ddot{\varphi}_i = 0 \quad \text{(Equation 7)}$$

These equalities could be rewritten in a form of moment equilibrium over the joint

$$\sum_{i=1}^{n} M_i = 0 \quad \text{(Equation 8)}$$

For the case when external loading is absent, taking into account definitions of the muscle moment $M_i = \vec{r}_i \cdot \vec{F}_i$, moment arm $r_i(\varphi) = \frac{\partial l_{Mus,i}}{\partial \varphi}$ and linear force from the element with *MAT_MUSCLE material $F_i = a_{i,\alpha} \cdot PCSA_i \cdot \sigma_{max} \cdot (\sigma_{SVS} + \sigma_{SSP})$ the equation for finding muscle activation levels $a_{i,\alpha}$ for α part of the hybrid controller could be derived:

$$\sum_{i=1}^{n} \left(\frac{\partial l_{Mus,i}}{\partial \varphi} \cdot a_{i,\alpha} \cdot PCSA_i \cdot \sigma_{max} \cdot (\sigma_{SVS} + \sigma_{SSP})\right) = 0 \text{ (Equation 9)}$$

This system of linear equation of n variables for muscle activation levels $a_{i,\alpha}$ could be solved for stimulation levels $u_{i,\alpha}^{open}$, which would be used as an input signal for the controller, by coupling it with the Equations 3 and 5. It results in a manifold of solutions, that could be constrained by applying additional conditions governed by the desired co-contraction in the muscles defining the respective joint stiffness. Higher co-contraction (muscle activation levels) leads to higher apparent joint stiffness slowing the movement velocities and vice versa. A list of all symbols with definitions used in the calculations is given in Table 3.

Table 3.
List of Symbols Used in Calculations

Symbol	Definition	Value
M_i	Moment generated by the muscle	Calculated in runtime
r_i	Instantaneous moment arm of the muscle	Calculated in runtime
F_i	Force generated by the muscle	Calculated in runtime
$l_{Mus,i}$	Length of the muscle	Derived in range of motion
φ_i	Joint angle	Preset value
$\dot{\varphi}_i$	Angular velocity of the joint	Calculated in runtime
$\ddot{\varphi}_i$	Angular acceleration of the joint	Calculated in runtime
$u_{i,\alpha}^{open}$	Muscle stimulation level from the feedforward α controller	Calculated in runtime
$a_{i,\alpha}$	Activation corresponding to the $u_{i,\alpha}^{open}$	Calculated in runtime
$PCSA_i$	Physiological cross sectional area of muscle	Calculated in runtime
σ_{max}	Peak isometric stress	Calculated in runtime
σ_{SVS}	Normalized stress generated by contractile element	Read from SVS curve
σ_{SSP}	Normalized stress generated by parallel elastic element	Read from SSP curve

Deriving control signals for the feedback λ part: The closed-loop stimulation signal in real muscle builds on the interaction of muscle spindles and Golgi tendon organs from the sensory side and α- and γ- motoneurons from the actuator side. From the technical perspective, such a system is based on the PD feedback control with the target to maintain the desired muscle length (Equation 2). Thus, before any analysis, it is crucial to preset the target muscle length as a variable for the controller to function. The straight forward way to find these values is to run the pre-simulation that brings the model into the desired state and measure the obtained muscle elements length knowing the attachment nodes. Such procedure was done for the arm model built and elbow flexion from 45deg to 145deg. Target length obtained and applied in the simulation for different muscles over time are shown in Figure 4.

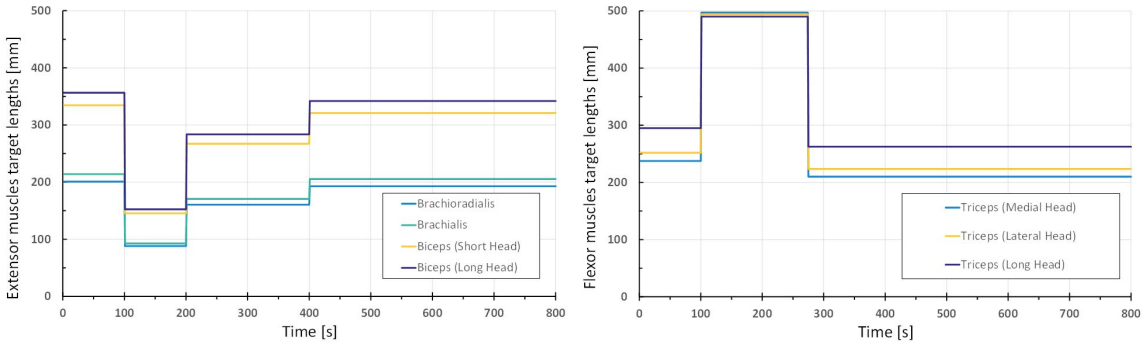

Figure 4. Muscle target lengths (feedback controller input signals λ) used for flexor and extensor muscles.

Simulation results for the arm model: FE arm model simulation results show a good correlation with the volunteer kinematics (Figure 5). A mismatch in a joint stiffness of the multi-body model compared to the human arm could explain small difference in a curve slope, thus higher speed of the simulated movement. Likewise, the lower joint stiffness in the model can also be a reason for a broader range of joint angles achieved.

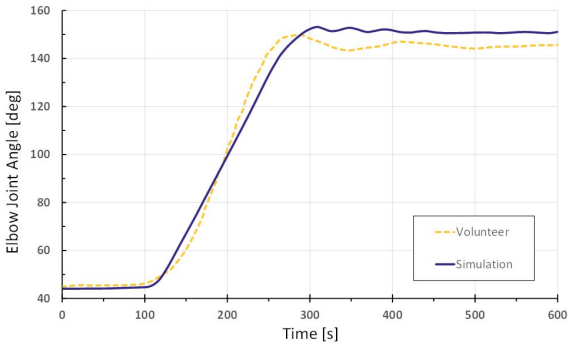

Figure 5. Comparison of elbow joint kinematics for the hybrid controller and volunteer response from [10].

Validation at the HBM level

After successful validation at the body region, the level of the study was extended to the whole HBM level. As a validation basis volunteer tests conducted in the OM4IS project [1] described shortly above was used. Braking and lane change scenarios were chosen for the current study. Data available for the comparison includes vehicle acceleration, head (at ear level) and torso (at T5 level) excursions. A model setup that is similar to the real world test was represented in the simulation environment. AHBM with seatbelt applied is seating in the reference seat in front passenger occupant position with the corresponding maneuver motion pulse applied (Figure 6).

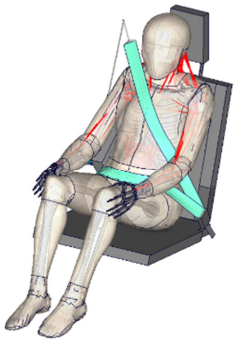

Figure 6. Simulation setup for the sled tests.

Open-loop stimulations $u_{i,\alpha}^{open}$ capable of maintaining the sitting posture with muscle co-contraction were determined and input, following by automatic calculation of closed-loop stimulation $u_{i,\lambda}^{closed}$ according to the procedure described above depending on the validation case.

Emergency braking: Following the experiment, a deceleration pulse to zero of the vehicle with the initial velocity of 50 km/h was applied to the sled. Feedback λ-controller was activated starting from the 10% of the peak pulse value and attaining 80-90% of the initial muscle length set as targets in the most distant body deflections. Choice of the muscle target lengths λ was performed according to suggestions given in [16].

Simulation results carried out for whole HBM with the functioning controller (referenced as active HBM) and without it (referenced as passive HBM) are shown in Figure 7. Head and torso centers of gravity (CG) excursions in the sagittal plane of the body were measured and compared to the experimental corridors. As seen from the results, almost for the whole observed maneuver time the aHBM excursions are lying inside the corridor measured for volunteers, being outside after HBM's contact with the seat on the ending phase. It could be explained by the influence of the contact parameters between the model's back and seat surface, which need to be tuned more precisely. Passive HBM is outside of the corridor for the initial phase and close to the margin later, having the same problem with a contact in the end.

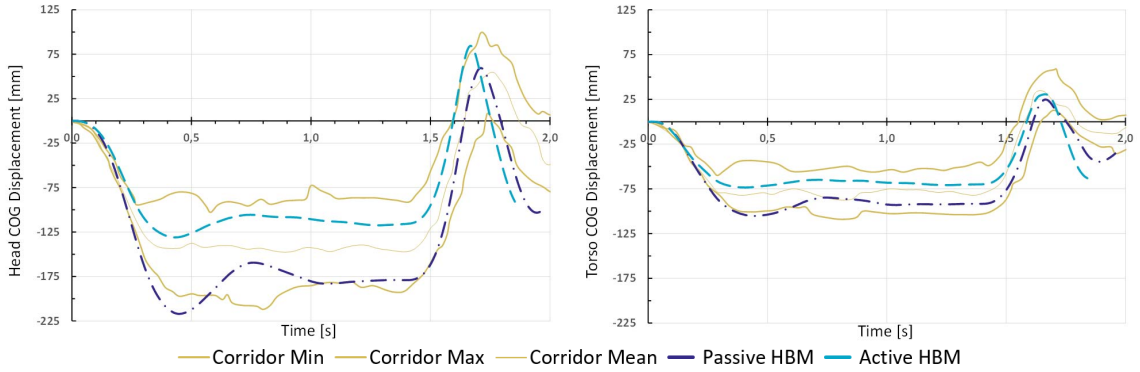

Figure 7. Comparisons of head and torso CG excursions during emergency braking maneuver and volunteer response corridor from [1].

Lane change: Lateral acceleration pulse of the vehicle with the longitudinal velocity 50km/h was applied to the sled. Feedback controller was active from the start and muscle target lengths λ were reversed at the point where the acceleration changes its direction with the pulse slope 0.

Simulation results are available in Figure 8, where head and torso CG excursions in the coronal plane of the body compared to the experimental corridors are given. In the same way, as observed for previous validation case, aHBM has less excursions with respect to the measurement corridor compared to a passive one. Due to the λ controller advantage to control each muscle length individually, additional volunteer muscle activity in order to avoid contact with the B-pillar was mimicked correctly. Head excursion being severely out of the corridor could be explained by the absence of physiological muscle routing in the neck, which is addressed in the DISCUSSION. Besides, more accurate assignment of target lengths to muscle groups responsible for neck flexion and lateral flexion of the lumbar spine could improve the aHBM kinematics. Further studies are needed in this direction.

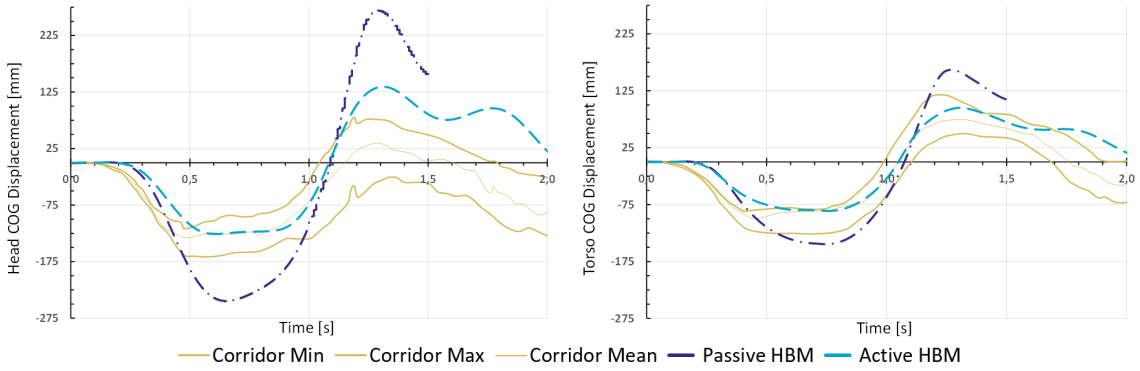

Figure 8. Comparisons of head and torso CG excursions during lane change maneuver and volunteer response corridor from [1].

DISCUSSION

The hybrid controller coupled with Hatze's activation dynamics represents physiological control of the muscle elements, which have been validated initially with an arm model. Obtained knowledge and original findings were extended to other body parts first and finally to the whole HBM. The suggested controller shows the capability to generate motion with appropriate muscle activation signals both in 1g braking and lane change scenarios, although the last one is considered to be a demanding task because of a switch in a muscle activity into opposite directions during the same event. This issue was successfully addressed with the proper combination of target lengths set to the muscles and governed by the hybrid controller, producing movements fast enough and similar to the volunteers.

As an additional outcome of the study, the importance of correct environment modeling according to the test protocol should be mentioned. The interior of the test vehicle should be replicated with all possible details since the seat and the seatbelt interact with the aHBM and produce additional contact forces and reactions, which affect the controller functioning.

Despite the good correlation with the experiments obtained, certain improvements need to be implemented in the aHBM and the hybrid controller. First of all, LS-DYNA material *MAT_MUSCLE that is currently used in a truss muscle elements lacks the serial elastic element representing elasticity of tendons, which was proven to have an important role for muscle modeling in some works [26,27]. Secondly, one of the current model limitations is the absence of muscle routing in some regions representing physiological muscle path including wrapping around joints. Such a modeling approach allows fulfilling of the correct line of action for the muscle, thus producing correct moment arms around the joints as shown in [28]. Thirdly, the current study does not include full activation calculation from the hybrid controller for the leg muscles, because the experimental data lacks the contribution of leg muscles in the motion studied in the study used [1]. Fourthly, the last conditionality applied in the current simulations is the absence of the gravity loading due to limitations of underlying passive HBM. Normally, due to the hybrid controller formulation, it would not affect the functioning itself, rather it will change the muscle activation levels produced and their correspondence for different muscle groups. These limitations designate trends for future work.

CONCLUSIONS

A further step towards an omnidirectional aHBM was made in this study. Such a model could be widely used for integrated safety systems development and accident whole sequence studies. Proposed physiological muscle activation hybrid controller is capable of resembling occupant kinematics in low-speed events, which was validated against experimental tests for 1g braking and lane change maneuvers from the OM4IS project. Besides, suggested control strategy allows to perform modeling of active and reactive human responses for other maneuvers by tweaking the controller parameters in conformity with the desired movement to be simulated. As a next ambitious goal one can set is a simulation of combined maneuvers where acceleration in two directions simultaneously is employed.

ACKNOWLEDGEMENTS

This work was supported by the German Research Foundation (DFG) within the Cluster of Excellence "Data-Integrated Simulation Science" (EXC 2075) at the University of Stuttgart and Tech Center i-protect.

The authors want to thank Atul Mishra, Pronoy Ghosh and Shubham Kulkarni for helpful discussions, useful advice, broad knowledge and valuable assistance with LS-DYNA simulations; Christian Mayer and Ravi Kiran Chitteti for comprehensive support and constructive collaboration.

REFERENCES

[1] Huber, P., Kirschbichler, S., Prüggler, A. and Steidl, T., 2015. “Passenger kinematics in braking, lane change and oblique driving maneuvers.” In Proceedings of the IRCOBI Conference (Lyon, France, September 9-11), 783-802.

[2] Muggenthaler, H., Adamec, J., Praxl, N. and Schönpflug, M., 2005. “The influence of muscle activity on occupant kinematics.” In Proceedings of the IRCOBI Conference, (Prague, Czech Republic, September 21-23), 313-323.

[3] Olafsdottir, J.M., Östh, J., Davidsson, J. and Brolin, K., 2013. “Passenger kinematics and muscle responses in autonomous braking events with standard and reversible pre□tensioned restraints.” In Proceedings of the IRCOBI Conference, (Gothenburg, Sweden, September 11-13), 602-617.

[4] Östh, J, Brolin, K, Ólafsdóttir, JM, Davidsson, J, Pipkorn, B, Jakobsson, L, Törnvall, F and Lindkvist, M., 2015. “Muscle activation strategies in human body models for the development of integrated safety.” In

Proceedings of the 24th International technical conference on the enhanced safety of vehicles (ESV), Gothenburg, Sweden.

[5] Kato, D., Nakahira, Y. and Iwamoto, M., 2017. "A study of muscle control with two feedback controls for posture and reaction force for more accurate prediction of occupant kinematics in low-speed frontal impacts." In Proceedings of the 25th International technical conference on the enhanced safety of vehicles (ESV), Detroit, USA.

[6] Östh, J., Brolin, K. and Bråse, D., 2014. "A Human Body Model with Active Muscles for Simulation of Pretensioned Restraints in Autonomous Braking Interventions." Traffic Injury Prevention, 16(3), 304–313.

[7] Iwamoto, M., Nakahira, Y., Tamura, A., Kimpara, H., Watanabe, I. and Miki, K., 2007. "Development of advanced human models in THUMS." In Proceedings of the 6th European LS-DYNA Users' Conference, Gothenburg, 47-56.

[8] Sugiyama, T., Weber, J., Sandoz, B. and Bensler, H.-P., 2018. "Validation of a Reactive Finite Element Human Body Model under Moderate Lateral Loading", In Proceedings of the 7th International Symposium on "Human Modeling and Simulation in Automotive Engineering," October 18-19, Berlin, Germany.

[9] Hill, A.V. "The heat of shortening and the dynamic constants of muscle" 1938. Proceedings of the Royal Society of London. Series B - Biological Sciences. The Royal Society, 126(843), pp. 136–195.

[10] Kistemaker, D. A., Van Soest, A. (Knoek) J. and Bobbert, M. F. 2006 ."Is Equilibrium Point Control Feasible for Fast Goal-Directed Single-Joint Movements?", Journal of Neurophysiology. American Physiological Society, 95(5), pp. 2898–2912.

[11] Hatze, H. 1977. "A myocybernetic control model of skeletal muscle." Biological Cybernetics. Springer Nature America, Inc, 25(2), pp. 103–119.

[12] LS-DYNA Keyword User's Manual Volume I, LS-DYNA R7.1 (r:5471). Livermore: Livermore Software Technology Corporation; May 26, 2014.

[13] Shelat, C., Ghosh, P., Chitteti, R. and Mayer, C., 2016. ""Relaxed" HBM–an Enabler to Pre-Crash Safety System Evaluation." In Proceedings of the IRCOBI Conference (Malaga, Spain, September 14-16), 239-247.

[14] Gawthrop, P., Loram, I., Lakie, M. and Gollee H., 2011. "Intermittent control: a computational theory of human control." Biological Cybernetics. Springer Nature, 104(1–2), pp. 31–51.

[15] Bayer, A., Schmitt, S., Günther, M. and Haeufle, D.F.B., 2017. "The influence of biophysical muscle properties on simulating fast human arm movements." Computer Methods in Biomechanics and Biomedical Engineering. Informa UK Limited, 20(8), pp. 803–821.

[16] Feldman, A. G. and Levin, M. F. 2009. "The Equilibrium-Point Hypothesis – Past, Present and Future." in Advances in Experimental Medicine and Biology. Springer US, pp. 699–726.

[17] Martynenko, O., Schmitt, S., Bayer, A., Blaschke, J. and Mayer, C., 2017. "A movement generation algorithm for FE Human Body Models." PAMM. Wiley, 17(1), pp. 201–202.

[18] Bizzi, E., Hogan, N., Mussa-Ivaldi, F.A. and Giszter, S., 1992. "Does the nervous system use equilibrium-point control to guide single and multiple joint movements?" Behavioral and Brain Sciences. Cambridge University Press (CUP), 15(4), pp. 603–613.

[19] Rockenfeller, R., Günther, M., Schmitt, S. and Götz, T., 2015. "Comparative Sensitivity Analysis of Muscle Activation Dynamics." Computational and Mathematical Methods in Medicine. Hindawi Limited, 2015, pp. 1–16.

[20] van der Horst, M.J., Thunnissen, J.G.M., Happee, R., van Haaster, R.M.H.P. and Wismans, J.S.H.M., 1997. "The Influence of Muscle Activity on Head-Neck Response During Impact." In: SAE Technical Paper Series, 12 November 1997. SAE International.

[21] Östh, J., Brolin, K. and Happee, R., 2012. "Active muscle response using feedback control of a finite element human arm model." Computer Methods in Biomechanics and Biomedical Engineering. Informa UK Limited, 15(4), pp. 347–361.

[22] Borst, J., Forbes, P. A., Happee, R. and Veeger, D., 2011. "Muscle parameters for musculoskeletal modeling of the human neck." Clinical Biomechanics. Elsevier BV, 26(4), pp. 343–351.

[23] Christophy, M., Faruk Senan, N.A., Lotz, J.C. and O'Reilly, O.M., 2011. "A Musculoskeletal model for the lumbar spine." Biomechanics and Modeling in Mechanobiology. Springer Nature, 11(1–2), pp. 19–34.

[24] Standring, S. Gray's anatomy: the anatomical basis of clinical practice. Philadelphia: Elsevier Limited, 2016.

[25] Östh, J., Brolin, K., Carlsson, S., Wismans, J. and Davidsson, J., 2012. "The Occupant Response to Autonomous Braking: A Modeling Approach That Accounts for Active Musculature." Traffic Injury Prevention. Informa UK Limited, 13(3), pp. 265–277.

[26] Kleinbach, C., Martynenko, O., Promies, J., Haeufle, D.F.B., Fehr, J. and Schmitt, S., 2017. "Implementation and validation of the extended Hill-type muscle model with robust routing capabilities in LS-DYNA for active human body models." BioMedical Engineering OnLine. Springer Nature America, Inc, 16(1).

[27] Günther, M., Schmitt, S. and Wank, V., 2007. "High-frequency oscillations as a consequence of neglected serial damping in Hill-type muscle models." Biological Cybernetics. Springer Nature, 97(1), pp. 63–79.

[28] Hammer, M., Günther, M., Haeufle, D.F.B. and Schmitt, S., 2019. "Tailoring anatomical muscle paths: a sheath-like solution for muscle routing in musculo-skeletal computer models." Mathematical Biosciences.

EVALUATION OF THORACIC DEFLECTION CRITERIA IN FRONTAL COLLISION USING THORACIC IMPACTOR SIMULATION WITH HUMAN BODY FE MODEL

Takayuki Kawabuchi, Yasuhiro Dokko
Honda R&D Co., Ltd. Automobile R&D Center
Japan

Paper Number 19-0068

ABSTRACT

When involved in vehicle accidents, the fatality rate of thoracic injury is high, following head injury, and the major causality is a rise of organ injury rates due to an increase in the Number of Fractured Ribs (NFR). Previous studies suggested a high correlation between thoracic deflection and NFR. However, the correlation was evaluated primarily using test data in frontal collisions with restraint systems such as seatbelts or airbags. Thus, it was not evaluated by local loading. The objective of this paper is to evaluate the correlation between the thoracic deflection criteria and NFR under local loading conditions by thoracic impactor loading.

In order to evaluate the relationship between thoracic deflection criteria and NFR by localized loading, thoracic impact is more proper than sled impact, in which loading location and direction depend on restraint systems. Impact simulations were conducted on 19 points to cover the whole right side of the thorax. The simulations were conducted with the Global Human Body Model Consortium (GHBMC) 50th percentile male model for LS-DYNA. Deflection of each rib was measured at its anterior tip and Rmax was calculated using the deflections on the 4th rib and the 7th rib to represent Anthropometric Test Dummy (ATD) measurement points. In addition, Average Deflection of All Ribs (ADAR) and Weighted Average Deflection of All Ribs (WADAR) were calculated as proposed criteria. Then the correlation between NFR and each of those criteria was evaluated using the correlation coefficient.

The results showed that some specific impact points lower the correlation between NFR and Rmax. Impacts around 1st through 3rd ribs incur rib fractures without deflection on the representative points because the sternum and costal cartilage do not transmit the force and deflection to other ribs. On the other hand, ADAR showed a higher correlation with NFR than Rmax, and WADAR further improved correlation with NFR.

The results showed that WADAR needs to be taken into account to improve correlation between NFR and thoracic deflection. It suggests that deflection of all ribs modified by homogeneity of each rib deflection need to be considered in order to properly evaluate rib fractures caused by localized loadings.

The thoracic deflection criterion using weighted average deflection of all ribs showed the highest correlation with NFR and it allows evaluating rib fractures even under localized loading conditions.

INTRODUCTION

Thoracic fatal injuries sustained by seatbelt-restrained occupants in frontal crashes appeared to be as equally frequent as, or following, head fatal injuries [1]. Kent et al. described that the percentages of drivers who died with Maximum Abbreviated Injury Score (MAIS) related to rib fractures increased with aging and suggested that rib fracture was associated with the significantly increasing fatality rate of thoracic injuries, especially on elderly drivers [2]. In addition, approximately 47% of elderly drivers died due to fatal thoracic injuries, while 24% of younger drivers did [2]. Furthermore, it is estimated that the population of adults over 65 years old would increase up to 83.7 million by the year 2050 in the United States [3] and it would result in increasing number of drivers sustaining severe injury on the thorax in traffic accidents. Hence, the necessity of consideration for thoracic protection is growing more than ever.

Kent et al. suggested that the risk of rib fractures increased with the level of thoracic compression and that thoracic injury risk was often described by the antero-posterior deflection of the thorax [4]. Most of the correlation between thoracic deflection criteria and thoracic injury risk was evaluated primarily using test data by Anthropometric Test

Dummy (ATD) and Post Mortem Human Subjects (PMHS) in frontal collisions with restraint systems such as seatbelt and/or airbag. However, rib fractures may often be likely to occur not only by restraint systems but also by contact with interior components. Small overlap or oblique collisions cause oblique motion to occupants and the thorax has contact with deformed interior components [5] [6]. Such a loading condition differs from the loadings by restraint systems and it may rather be similar to some localized loading than a broad loading.

The objective of this study was to evaluate the correlation between the thoracic deflection criteria and the number of fractured ribs (NFR) under localized loading using thoracic impact simulations with various impact locations and directions using a human body model.

METHOD

Human Body Model

Global Human Body Models Consortium's 50th percentile male occupant model (GHBMC M50-O) v4.5 for LS-DYNA was adopted as a baseline model and was modified to have a thorax with elderly features for evaluation of thoracic deflection criteria. Rib fracture was predicted by elements exceeding the failure strain threshold, thus it was needed to validate the relationship between loading and strain on rib cortical bones. Single rib and rib cage of GHBMC M50-O was validated against the relationship between rib fracture and deformation under various boundary conditions [7]. As a validation for single rib, the relationship between rib deflection and strain of each rib was validated by an anterior to posterior bending test. [8] And as a validation for rib cage deformation, thoracic response against localized loading was validated by the point loading at various locations [9]. Based on those validations, the GHBMC M50-O model was considered to be able to evaluate rib fractures caused by localized loadings at various points.

The representative age for the elderly was set at 75 years old based on Ito et al [10]. The material properties of rib cortical bone for the baseline model was modeled with piecewise linear plasticity material model with Young's modulus, yield stress, and a failure strain. The Young's modulus of the rib cortical bone was set at 11.5 MPa and yield stress was set at 88 MPa based on Li et al [11]. Failure strain was determined by the sum of yield strain and ultimate plastic strain. Yield strain was 0.0077, which was calculated by Young's modulus and yield stress. The ultimate plastic strain of the cortical bone had correlation with age as given in Equation 1 [12] and set at 0.0088. Thus, the failure total strain as a rib fracture threshold resulted in 1.65% and shell elements constituting rib cortical bone model were judged as a fracture when the strain on an element exceeds the threshold.

$$\text{Ultimate plastic strain [unitless]} = \frac{-383age[years] + 37514}{10^6} \qquad \text{(Equation 1)}$$

Rib cortical bone thickness was decreased from the baseline model based on the aging function of linear relationship between age and rib cortical bone thickness described by Ito et al [10]. Since the base age of GHBMC M50-O was not explicitly defined, it was assumed average, and the cortical bone thickness at 75 years old was presumed. Rib cortical bone thickness of GHBMC M50-O v4.5 was distributed on every shell element of the rib derived from CT scan data and its average thickness was 0.67 mm [8]. Thereby base age was assumed as roughly 60 years old and was decreased based on the aging function. The Young's modulus of the costal cartilage was set at 19.7 MPa based on Yamada [13]. Kent et al. showed upward geometrical change by aging and described those changes on rib cage influences on increasing stiffness of rib cage [14]. On the other hand, Ito et al compared the contribution of thorax characteristic change by aging and showed that the influence of the geometrical change of rib cage was smaller than change of cortical bone thickness or failure strain [15]. In addition, the aim of this study was to evaluate the relationship between rib cage deformation and NFR on same subject. Therefore, the authors decided that the rib cage geometry was not to be modified in this study. The model with those modifications was validated against frontal thorax impact tests and belted full body frontal sled tests [16].

Thoracic impact simulation

Thoracic impactor loading was conducted in order to represent localized loading and reconstruct thoracic deformation due to a localized loading by interior components such as door trims. Besides, the thoracic impactor was presumed to be able to comprehensively evaluate the relationship between thoracic deflection criteria and NFR since the impactor did not depend on the character of restraint systems.

A rigid impactor model with a small diameter was employed in order to generate localized loading on the thorax. The impactor was a cylindrical shape with a 75 mm diameter and its mass was 22 kg. The initial velocity was set at high and low velocity along the axis direction of the impactor, 6.7 m/s and 4.7 m/s respectively as boundary conditions. Low velocity was determined to be a half of the kinetic energy of high velocity in order to evaluate velocity dependence of the relationship between rib fracture and thorax deflection. Centers of impactor contact locations were set at 19 points on the whole right half of the thorax. The impact region was focused on the single side based on the assumption that the rib cage was symmetrical. A base contact point was set to match the center of the impactor on a point on the sternum 70 mm superior to the tip of the xiphoid. The point was approximately the same height as the 4th rib. The impact direction was determined to be perpendicular to the plane on the thoracic surface, which was defined as 63.5 degrees to the horizontal plane and depicted as Figure 1. The other 18 contact points were set on each place with each direction described in Table 1 and Figure 1. Each contact point was set at a point on position Y and Z defined as lateral and vertical coordinates from the base contact point. The impact direction seen from the impactor side view was same as that of base contact point. The Z angle shown in Figure 1, which defines an angle of the impactor around vertical axis, was set to be perpendicular to the thoracic surface and angles at each point were shown in Table 1.

Table 1.
Impactor contact positions

Point No.	Position Z [mm]	Position Y [mm]	Angle Z [deg]
1	0	0	0
2	125	0	0
3	125	75	30
4	125	125	50
5	75	0	0
6	75	75	20
7	75	125	50
8	75	150	60
9	0	75	20
10	0	125	40
11	0	150	65
12	-75	0	0
13	-75	75	20
14	-75	125	40
15	-75	150	60
16	-150	0	0
17	-150	75	20
18	-150	125	40
19	-150	150	60

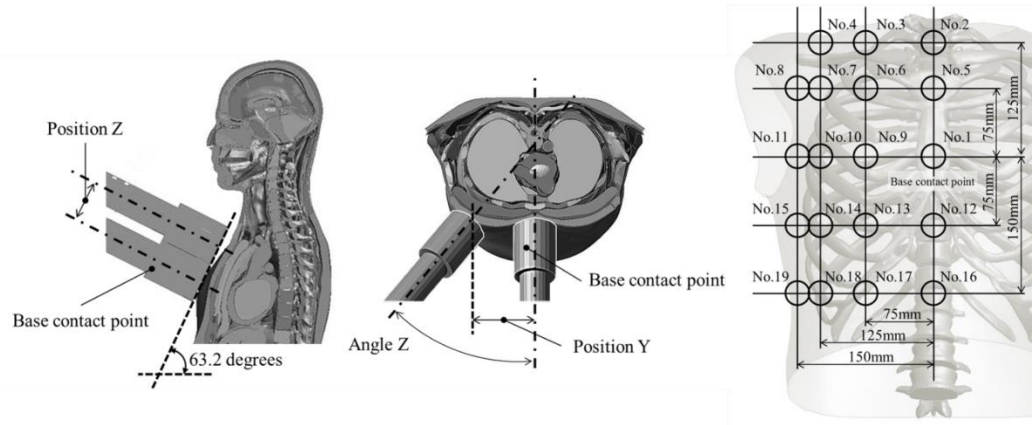

Figure 1. The definition of parameters and impact positions

Rib Deflection Measurement

Rib deflection in X, Y, and Z (XYZ) directions was measured at each rib anterior tip. The local coordinate system was defined at the costovertebral joint of each rib. The local x axis pointed anterior direction of the thorax, the local y axis pointed right-hand direction and the local z axis pointed upward. Since rib deformation caused by oblique loading was largely related to y deflection, resultant deflection was applied to criteria. Measurement results were processed and defined as a criterion and the correlation between the criteria and NFR were evaluated by the correlation coefficient defined as the R-squared values (R^2), which were calculated by linearization.

Rib deflection evaluation criterion

Two types of criteria were defined for rib deflection evaluation. One type was using a value of the largest deflection between all ribs and the other type was using an average value of normalized all rib deflections.

A. **Criterion using the largest rib deflection:** The criterion defined the larger one of maximum XYZ resultant deflections of the 4th Rib and the 7th Rib as a representative point. The representative ribs were determined to be similar to the measurement points of Infra-Red Telescoping Rod for the Assessment of Chest Compression (IR-TRACC) applied to Test device for Human Occupant Restraint (THOR) ATD. This criterion was defined as Rmax.

Furthermore, the largest one between the maximum XYZ resultant deflections of the 12 ribs was defined as a criterion. This was defined as Maximum Deflection of All Ribs (MDAR).

B. Criterion using average value of normalized all rib deflections: For a comparison with the criteria using maximum value, average value of the maximum XYZ resultant deflection of the 12 ribs was defined as a criterion. The amount of deflection to fracture is different among every rib since they have different shapes and lengths. Those differences should be taken into account to evaluate NFR by an average deflection of the 12 ribs. In order to remove the influences of that, each XYZ resultant deflection was normalized by initial length between a measurement point and the coordination origin of each rib. The definition of initial length and length of each rib were depicted in Figure 2 and Table 2, respectively. The criterion was defined as Average Deflection of All Ribs (ADAR) and given in Equation 2.

$$\mathrm{ADAR} = \frac{\sum_{i=1}^{n}(d_i/L_i)}{n} \qquad \text{(Equation 2)}$$

Where, di = normalized deflection of each rib

Li = rib initial length

n = Number of ribs. Here this is 12.

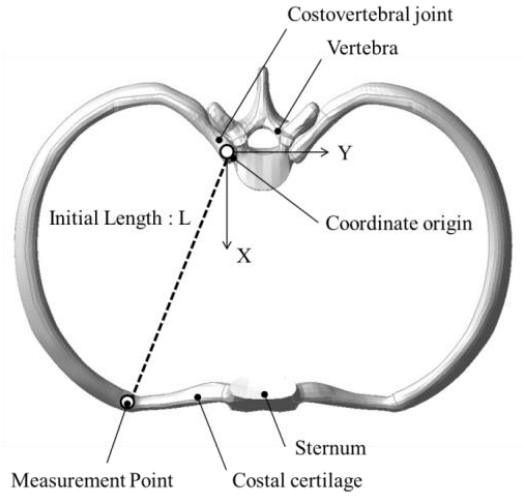

Figure 2. Rib measurement point and detail of the location

Table 2.
Initial length of each rib

Rib No.	Initial Length L [mm]
1	73.7
2	108.6
3	145.0
4	173.0
5	189.4
6	199.7
7	204.1
8	208.9
9	198.2
10	176.8
11	151.4
12	94.6

RESULTS

All results of evaluation criteria and NFR of each impact point were listed on Table A1 and Table A2.

The relationships between Rmax, MDAR, and NFR were shown in Figure 3(a) and 3(b). R^2 of Rmax was lower than that of MDAR. This is assumed because NFR were varied from 0 to 6 between Rmax 20 mm and 30 mm, while such a variance did not happen for MDAR. The relationship between ADAR and NFR was shown in Figure 3(c). The R^2 was higher than Rmax or MDAR and the scatter became smaller.

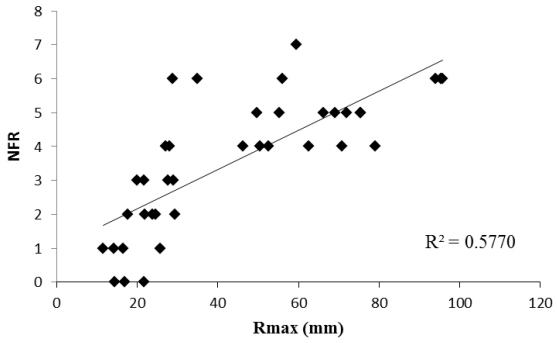

(a) Rmax vs NFR

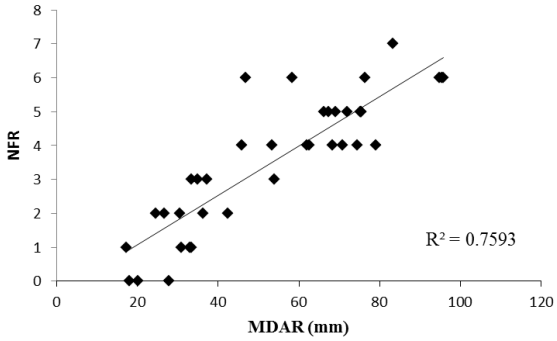

(b) MDAR vs NFR

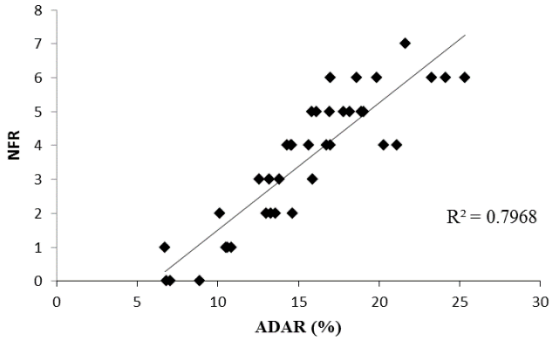

(c) ADAR vs NFR

Figure 3. Correlations between rib deflection criteria and NFR

However, some deformation patterns, which were provided in Figure 4(a) and 4(b), showed large different NFR even under the same ADAR. The impact point at No.6 incurred 4 fractured ribs while No.14 incurred 7 fractured ribs. It found that the difference of deformation shape affected NFR.

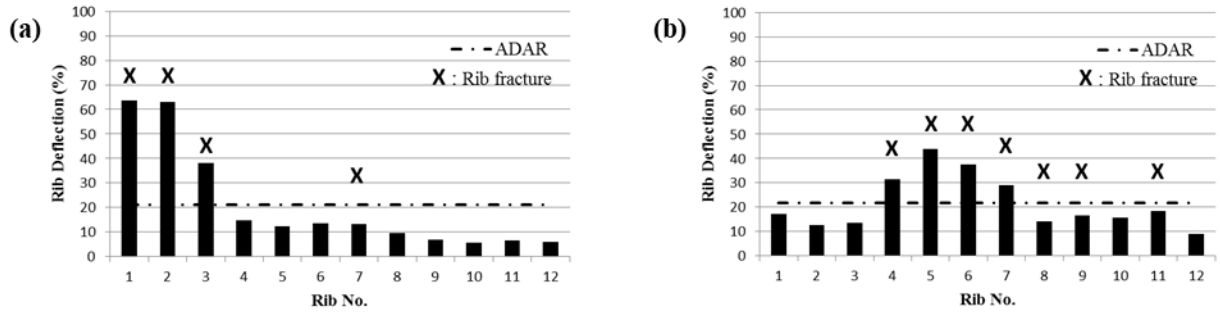

Figure 4. Each rib deflection: (a) at impact point No.6 and (b) at impact point No.14

Thus, a weighting factor was applied to ADAR in order to distinguish the deformation shape due to effects of impact point differences. Edwards et al suggested evaluating a degree of deformation of deformable barrier by homogeneity of deformation [17]. Based on this evaluation method, homogeneity of thoracic deformation shape was applied to a criterion adopting a weighting factor. The criterion was defined as Weighted Average Deflection of All Ribs (WADAR) as described in Equation 3. The weighting factor is the parentheses in the equation. The second term of the weighting factor, which indicates inhomogeneity, becomes large when the local deformation occurs largely on the thorax. In other words, the degree of local deformation, which has large ADAR and small NFR, is larger and WADAR becomes smaller. This weighting factor adjusts the inconsistency between ADAR and NFR as described above.

$$\mathrm{WADAR} = \left(0.2 - \frac{\sqrt{\sum_{i=1}^{n}(ADAR - d_i)^2}}{n}\right) \times ADAR \qquad \text{(Equation 3)}$$

Where, di = normalized deflection of each rib

n = number of ribs. Here, this is 12.

Further, the first term, 0.2, was empirically determined to make a correlation coefficient higher.

Figure 5 shows the relationships between WADAR and NFR. R^2 of WADAR is higher than that of ADAR. WADAR of No.6 and No.14 were 2.97% and 3.66%, respectively and they showed the differences although their ADAR was almost the same.

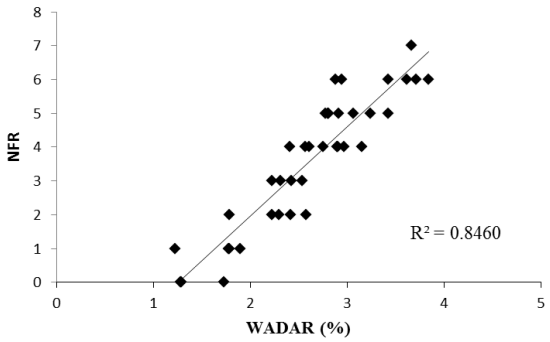

Figure 5. Correlation between WADAR and NFR

DISCUSSION

As mentioned above, WADAR indicated the highest R^2 between four criteria. Considering the fracture mechanisms, impact energy generated by a thorax impactor incurs thoracic deformation and rib fracture occurs when it becomes beyond the critical value. When larger energy is applied, NFR will increase. Since WADAR is based on ADAR, using the sum of all rib deflections as shown in Equation 2, it had a better correlation with NFR than those of criteria using maximum deflections as a representation. Impact on the upper region of the thorax concentrates the energy on one or a few neighboring ribs and incurs rib fractures around that limited region. Under such a condition, NFR increased without deformation at the representative point when remote region from representative points, such as around clavicle or upper part of rib cage, were impacted. Costal cartilage around the sternum deforms largely and just transmits little rib deformation to the 4th rib or the 7th rib, which was defined as a representative point for THOR's IR-TRACC. These results may suggest that the criterion using the deformation of representative points possibly has low sensitivity to evaluate rib fracture injury under localized loading conditions.

As indicated in Figure 4, large localized deformation of the thorax increases the average of rib deflection without NFR increase and results in overestimation of ADAR with R^2 reduction. This result indicates the necessity to distinguish deformation shape for NFR prediction. WADAR is possible to modify such overestimated ADAR by distinguishing such localized deformation from uniform deformation by a weighting factor. A weighting factor evaluates homogeneity of rib cage deformation shape. The weighting factors of the impact points at No.6 and No.14 were 0.141 and 0.169, respectively. As such, the value of the weighting factor is small for local deformation. The weighting factor modified overestimated ADAR, which shows large value although the NFR is small. Those modifications for distinguishing deformation patterns represented improvement of a correlation between the criterion and NFR.

This study proposed the criterion indicating high correlation with NFR. As future work, the accuracy and robustness should be improved in order for evaluation under same conditions as actual accidents with interior component and restraint systems, such as seatbelts and/or airbags. The criterion is currently based on the results under impact on a single side, thus, it should be improved to evaluate including the non-impacted side. Since this study did not show the physical meaning of coefficient in WADAR, the meaning of value should be considered in a future work.

In addition, the criterion was applied to only the human body, while the manner to apply to ATD should be considered. The THOR dummy is limited in evaluation for frontal collision mode and the thoracic deformation measurement device is currently only four IR-TRACCs. The alternative methods for these limitations should be considered to apply WADAR to the THOR dummy.

CONCLUSIONS

The thoracic deflection criterion using weighted average deflection of all ribs showed the highest correlation with NFR and it allows evaluating rib fractures even under localized loading conditions. Distinguishing deformation patterns improved the prediction of NFR by rib deflections. That suggested that the criterion using the deformation of representative points has possibly low sensitivity to evaluate rib fracture injury under localized loading conditions.

It is not possible to evaluate deflections of all ribs with the current ATD, thus a method to measure all rib deflections, or another alternative, is needed.

REFERENCES

[1] Kent, R.W., Henary, B., Matsuoka, F., 2005. "On the fatal crash experience of older drivers." Annu Proc Assoc Adv Automot Med. 49: 371–391.

[2] Kent, R.W., Woods, W., Bostrom, O., 2008. "Fatality risk and the presence of rib fractures." Ann Adv Automot Med. 52: 73–84.

[3] National Highway Traffic Safety Administration. 2017. "Traffic Safety Facts 2015." DOT HS 812 372, 1-5, Available at https://crashstats.nhtsa.dot.gov/#/DocumentTypeList/12. Accessed November 22, 2018

[4] Kent, R.W., Patrie, J., Poteau, F., 2003. "Development of an age-dependent thoracic injury criterion for frontal impact restrain loading." Proc. Int. Tech. Conf. Enhanced Safety Vehicles 2003; 12

[5] Iraeus, J., Lindquist, M., 2013. "Evaluation of chest injury mechanisms in nearside oblique frontal impacts." Ann Adv Automot Med. Sep; 57: 183–196.

[6] Brumbelow, M.L., Farmer, C.M., 2013. "Real-world injury patterns associated with hybrid III sternal deflections in frontal crash tests." Traffic Injury Prevention, vol. 14, issue 8

[7] Global Human Body Models Consortium, Available at http://www.ghbmc.com/publication/

[8] Li, Z., Subit, D., Kindig, M., Kent, R., 2010, "Development of a Finite Element Ribcage Model of the 50th percentile Male with Variable Rib Cortical Thickness." 38th International Workshop on Human Subjects for Biomechanical Research, National Highway Traffic Safety Administration, U.S. D.O.T.

[9] Poulard, D., Subit, D., 2015. "Unveiling the Structural Response of the Ribcage: Contribution of the Intercostal Muscles to the Thoracic Mechanical Response." Proc. Int. Tech. Conf. Enhanced Safety Vehicles 2015

[10] Ito, O., Dokko, Y., Ohashi, K., 2009. "Development of adult and elderly FE thorax skeletal models." SAE Technical Paper 2009-01-0381

[11] Li, Z., Kindig, M.W., Kerrigan, J.R., Untaroiu, C.D., Subit, D., Crandall, J.R., Kent, R.W., 2010. "Rib fractures under anterior–posterior dynamic loads: Experimental and finite-element study." Journal of Biomechanics, vol. 43, issue 2, 228 - 234

[12] Schoell, S.L., Weaver, A.A., Vavalle, N.A., Stitzel, J.D., 2015, "Age- and sex-specific thorax finite element model Development and Simulation." Traffic Injury Prevention, vol. 16, issue sup1

[13] Yamada, H., 1970. "Strength of biological materials." Williams & Wilkins

[14] Kent, R.W., Lee, S., Darvish, K., Wang, S., Poster, C.S., Lange, A.W., Brede, C., Lange, D., Matsuoka, F., 2005. “Structural and Material Changes in the Aging Thorax and Their Role in Crash Protection for Older Occupants.” Stapp Car Crash Journal, vol.49, 231-249

[15] Ito, O., Ito, Y., Dokko, Y., Mori, F., Ohhashi, K., 2010. “Successive development of adult and elderly FE thorax models (Japanese).” Paper presented at: Society of Automotive Engineers of Japan (JSAE), paper #20105713

[16] Kawabuchi, T., Takahashi, Y., 2018. “Verification of rib fracture prediction in frontal collision.” Paper presented at: International Research Council on Biomechanics of Injury (IRCOBI); September 12-14, 2018; Athens, Greece

[17] Edwards, M., Davis, H., Hobbs, A., Thompson, A., 2003. “Development of test procedures and performance criteria to improve compatibility in car frontal collisions.” Proceedings of the Institution of Mechanical Engineers Part D Journal of Automobile Engineering, 2003

APPENDIX A

Table A1.

Table of value of criteria at impactor speed 6.7m/s

Impact point No.	NFR	Rmax [mm]	MDAR [mm]	ADAR [%]	WADAR [%]
1	2	29.3	36.3	13.6	2.42
2	1	14.3	17.4	6.7	1.22
3	2	21.8	42.4	14.6	2.30
4	2	24.6	30.5	13.0	2.23
5	3	19.9	37.3	13.8	2.31
6	4	27.0	68.3	21.1	2.97
7	6	28.9	58.3	18.6	2.94
8	6	34.9	46.8	17.0	2.88
9	6	95.8	95.8	25.3	3.84
10	6	95.4	95.4	24.1	3.71
11	6	94.1	94.8	23.3	3.62
12	3	29.0	35.0	13.2	2.54
13	5	55.4	75.3	18.9	3.24
14	7	59.5	83.3	21.6	3.66
15	6	56.1	76.4	19.9	3.42
16	2	23.9	26.7	13.3	2.57
17	5	69.1	69.1	19.1	3.42
18	5	75.4	75.4	17.8	3.07
19	4	70.8	70.8	16.7	2.90

Table A2.

Table of value of criteria at impactor speed 4.7m/s

Impact point No.	NFR	Rmax [mm]	MDAR [mm]	ADAR [%]	WADAR [%]
1	1	25.7	31.0	10.6	2.42
2	0	14.5	18.1	7.1	1.22
3	1	16.5	33.1	10.8	2.30
4	2	17.7	24.5	10.1	2.23
5	1	11.5	33.5	10.5	2.31
6	3	21.7	54.0	15.9	2.97
7	4	28.0	45.8	14.6	2.94
8	3	27.7	33.5	12.6	2.88
9	4	79.1	79.1	20.3	3.84
10	5	75.4	75.4	18.2	3.71
11	5	71.9	71.9	16.9	3.62
12	0	21.8	27.9	6.8	2.54
13	4	46.3	62.0	15.7	3.24
14	4	50.6	74.5	17.0	3.66
15	5	49.8	67.4	16.1	3.42
16	0	16.9	20.2	8.9	2.57
17	4	52.6	53.3	14.3	3.42
18	5	66.2	66.2	15.8	3.07
19	4	62.6	62.6	14.5	2.90

SIMULATION ASSESSMENT OF INJURY TRENDS FOR 50TH PERCENTILE MALES USING POTENTIAL SEATING CONFIGURATIONS OF FUTURE AUTOMATED DRIVING SYSTEM (ADS) EQUIPPED VEHICLES

Vikas Hasija
Rohit Kelkar
Bowhead (Systems & Technology Group)
USA

Erik G. Takhounts
National Highway Traffic Safety Administration
USA

Paper Number 19-000345

ABSTRACT

Occupants in vehicles equipped with automated driving systems (ADS) may sit in various seating positions (e.g. forward facing, rear facing, oblique facing) and at different seatback recline angles. Since forward facing impacts have been studied in detail, the objective of this study was to: A) analyze rear impacts using finite element (FE) human and seat models; B) update the seat model based on lessons learned from part A and then analyze the injury metrics trend for the 50th percentile male occupant: i) at various seatback recline angles, and ii) in different carriage style seating configurations; and C) investigate a potential countermeasure for reducing injury metric values. For analyzing rear impacts, the Total Human Model for Safety (THUMS) FE model along with a FE driver seat model of a Toyota Yaris was used. Simulations were carried out at both low (Delta-V=15 mph) and high (Delta-V=35 mph) speeds to understand the effect of seat hinge stiffness on THUMS kinematics at both speeds. Other design changes such as integrated seat belts and active head restraints were also evaluated. Then injury metrics were analyzed for the 50th percentile male occupant at various seatback recline angles and in different carriage style seating configurations. For this part of the study, Global Human Body Models Consortium (GHBMC) 50th percentile simplified (M50-OS) male FE model was used along with a Honda Accord FE driver seat model. Head Injury Criterion (HIC) and Brain Injury Criterion (BrIC) were used as injury metrics for the head/brain, while max chest deflection was used as the chest injury metric. A potential countermeasure for reducing BrIC was investigated for the seating configuration with the highest BrIC value. From the rear impact study, it was found that having a rigid seat hinge, an integrated seatbelt, and an active head restraint help in reducing the injury metrics. Higher BrIC values were observed at higher seatback recline angles for both frontal and rear impacts. Chest deflection was also higher at higher seatback recline angle for frontal impact but showed an inverse trend for rear impact. For occupants experiencing frontal/oblique-frontal impacts, the BrIC and chest deflection values ranged from 0.75 to 0.81 and from 33 to 45 mm respectively whereas for occupants experiencing rear/oblique-rear impacts, the BrIC and chest deflection values ranged from 0.23 to 0.93 and from 17 to 24 mm respectively. HIC_{15} values were below 300 for the various recline angles and seating configurations investigated except one instance where the head contacted the knee. The potential countermeasure (redesigned head restraint) investigated was effective in reducing BrIC by a third for the case with the highest BrIC value (0.93).

KEYWORDS: Automated driving systems (ADS), human models, head/brain injury, chest injury, carriage style seating configurations

INTRODUCTION

The development of vehicles equipped with automated driving systems (ADS) or self-driving cars is one of the most exciting and important innovations in transportation history. ADS equipped vehicles give occupants the ability to travel from one place to another with minimal or no human intervention depending on the automation level. SAE [1] specifies six automation levels which vary from 0 (no automation) to 5 (full automation). ADS focus on levels 3 through 5, in which human driver can give control to the ADS and is not expected to perform any driving related task for a period of time or it may include no human driver at all [2]. By combining advanced technology with minimal or no human intervention, ADS have the potential to reduce collision incidence. However, there will be

vehicles on the public roadways that will not be equipped with ADS. These vehicles can still crash into ADS equipped vehicles, which makes occupant protection very important.

The occupant compartment of ADS equipped vehicles has been dubbed as the "next living space." These vehicles may have non-traditional seating configurations such as front seats that can rotate to face the rear seat occupants, like a carriage style seating configuration. In addition to having forward-facing and rear-facing occupants, ADS equipped vehicles can have occupants sitting oblique to the length of the vehicle because of the flexibility to orient the front seats by various angles. Also, the occupants in these vehicles do not have to sit up right, they can sit at different recline angles of the seatback. A study [3] was conducted to explore and identify possible seating positions and desired activities in future highly automated cars. They observed that for long drives, with several occupants in the car, there was a desire to rotate the seat to a living room position (like carriage style seating) and for short drives, there was a preference to maintain forward-facing position but with seat reclined to a more relaxed position. The flexibility to rotate and recline the seats to many different positions makes occupant protection for ADS equipped vehicles particularly challenging. Current test procedures and Anthropomorphic Test Devices (ATD) might not be sufficient to evaluate injury risk for all these scenarios. Human FE models are an important tool that can allow assessment of occupant protection for new car interiors with flexible seat arrangements.

In ADS equipped vehicles, occupants may experience different types of impact depending on how they are seated. For example, if occupants are seated in a carriage style seating configuration, an impact to the front of the vehicle will cause occupants in the rear seats to experience frontal impact and occupants in front seats to experience rear impact. Currently, most of the high-speed vehicle impact tests are conducted for frontal impacts (e.g. New Car Assessment Program (NCAP) [4]), where all occupants are seated forward-facing. Low speed rear impact tests are presently conducted, however, for occupant protection in ADS equipped vehicles, high speed rear impact tests need to be conducted as well to evaluate the seats, seatbelt, and to understand the occupant kinematics.

It is the purpose of this paper to use FE human and seat models to:

- evaluate occupant kinematics in both low and high speed rear impacts to identify potential injury modes;
- analyze injury metrics trend at different seatback recline angles;
- analyze occupant kinematics and injury metrics trend in carriage style seating configuration using two occupants in different orientations of the front seat;
- evaluate a possible countermeasure for reducing BrIC.

METHODS

Injury Metrics

The following injury metrics are used in this study:

a) $$\text{BrIC} = \sqrt{\left(\frac{\omega_x}{\omega_{xC}}\right)^2 + \left(\frac{\omega_y}{\omega_{yC}}\right)^2 + \left(\frac{\omega_z}{\omega_{zC}}\right)^2} \qquad (1)$$

where, ω_x, ω_y, and ω_z are the max angular velocities computed at any time about x-, y-, and z-axes respectively. ω_{xC} *(66.25 rad/s),* ω_{yC} *(56.4 rad/s)*, and ω_{zC} *(42.87 rad/s)* are the corresponding critical angular velocities [5]. The time limit for calculation of BrIC was the entire duration of the simulation (150 ms).

b) $$\text{HIC}_{15} = \left\{ \left[\frac{1}{t2-t1} \int_{t1}^{t2} a(t)dt \right]^{2.5} (t2 - t1) \right\}_{max} \qquad (2)$$

where, *t2* and *t1* are any two arbitrary times during the acceleration pulse [6].

c) Chest deflection: It was computed as the absolute maximum of the X displacement of the sternum.

Measurements at the neck have proven to be an issue in both the M50-OS and THUMS model because of the modeling techniques used. Therefore, neck injury criterion (N_{ij}) is not reported in this study.

Crash Pulse

The crash pulse used in this study (Figure 1) was chosen from an oblique test (NHTSA test # 9476), which consists of an Oblique Moving Deformable Barrier (OMDB) traveling at a target speed of 90.1 kph into a stationary mid-size four door sedan (2015 Chevrolet Malibu) positioned at 15 degrees relative to the moving barrier and impacted 35% to the left front of the vehicle. Since the crash pulses for oblique impacts are usually more severe in terms of injury

risk compared to those for frontal impacts at the same Delta-V, the crash pulse was chosen from an oblique test. Figure 1 shows the resultant of the longitudinal and lateral acceleration components only (rotational acceleration components were not considered). This resultant pulse was used for all the simulations.

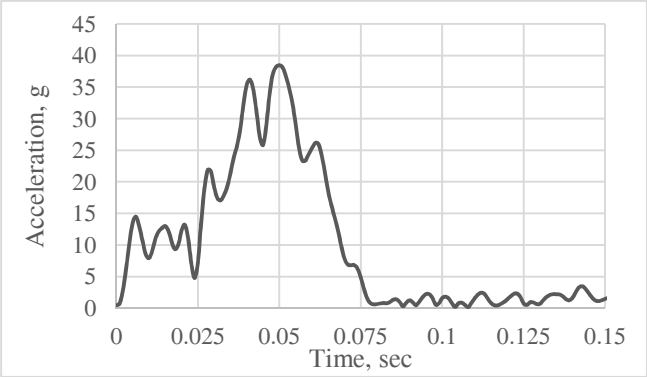

Figure 1. Crash pulse

Model Set-up

All simulations in this study were carried out in a sled type environment. Two different validated 50th percentile FE human models namely THUMS [7] and Simplified GHBMC (M50-OS) [8] along with two different generic FE deformable driver seat models of a 2010 Toyota Yaris [9] and 2014 Honda Accord [10] were used. A validated generic seatbelt system with retractor, pretensioner and load limiter was utilized. The pretensioner and load limiter were set to 1 kN and 3 kN, respectively. The floor was made rigid and no other vehicle structure was used. A sample simulation set-up is shown in Figure 2. All simulations were performed using the general-purpose finite element program, LS-DYNA Version 971 [11].

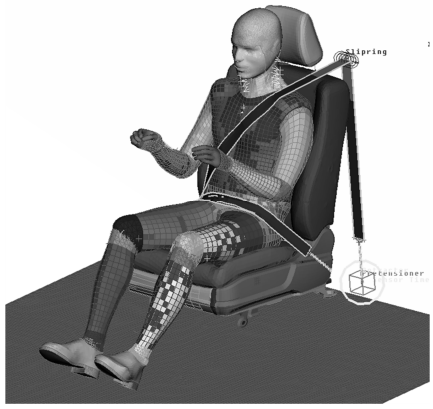

Figure 2. Sample simulation set-up

Analysis

Part 1: Preliminary investigation

This study was carried out to a) evaluate occupant kinematics and injury metrics in both low and high speed rear impacts, and b) explore ways to reduce these injury metrics values. A Toyota Yaris FE driver seat model with THUMS was used for this preliminary analysis. Since no sub system testing or validation was performed on this seat model in rear impacts, a few modifications were made. The bottom seat frame was stiffened and a seat hinge (revolute joint between the seatback and the bottom seat frame, missing in the original model) was created (Figure 3).

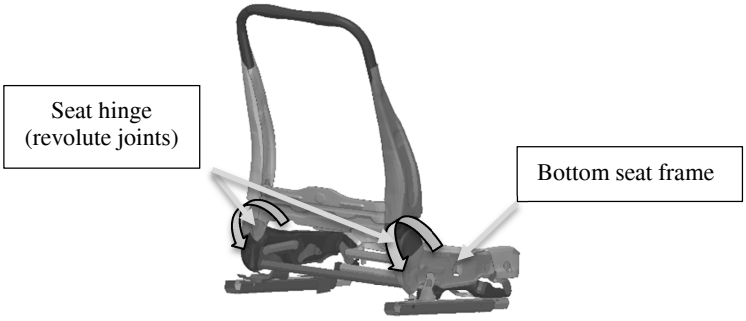

Figure 3. Toyota Yaris FE seat model (seat frame)

A baseline simulation was set up in accordance with a cadaver experiment [12], which consists of a cadaver placed in an experimental seat with non-integrated seatbelt (Figure 4a) and subjected to a rear impact using a 10g acceleration pulse (Delta-V of 15 mph, Figure 4b).

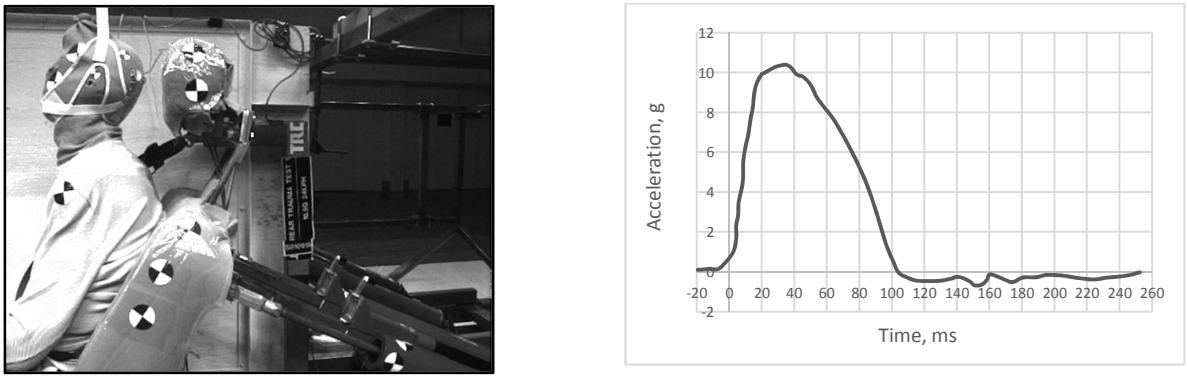

(a) (b)

Figure 4. a) Rear impact cadaver experiment; b) Experimental 10g pulse

THUMS model was positioned in the seat using gravity simulation following which belt creation and fitting was performed in ANSA [13]. Between the experiment and simulation, the seat back recline angle was the same (25^0) but there was slight difference in the seat pan angle (20^0 in experiment compared to 10^0 in simulation). The seat hinge stiffness in the simulations was set close to that of the experimental seat to ensure equivalent seatback rotation during impact. Both the 10g experimental acceleration pulse (Figure 4b, Delta-V=15 mph) and the crash pulse (Figure 1, Delta-V ~35 mph) were applied to the model to study low and high speed rear impacts. Potential injury modes were identified and corresponding values of HIC_{15}, BrIC and chest deflection were recorded. In addition to the simulations performed with a compliant seat hinge (seatback rotates), similar low and high speed rear impact simulations were performed with a rigid seat hinge (no/minimal seatback rotation) to evaluate its effect on the injury metrics (HIC_{15}, BrIC and chest deflection). Also, a head restraint study was conducted wherein the distance between the head and the head restraint was varied (1 mm, 45 mm) to evaluate its effect on the injury metrics. This head restraint study was conducted with a rigid seat hinge and using the crash pulse in Figure 1(Delta-V ~35 mph).

Part 2: Reclined positions and carriage style seating configurations

Compared to the preliminary investigation (Part1) that was performed using a Yaris FE driver seat model and THUMS human model, this part of the study was conducted using a Honda Accord FE driver seat model and simplified GHBMC FE human model (M50-OS). The Honda Accord FE driver seat model was not available to us during the preliminary investigation. Upon availability, the Honda Accord FE driver seat model was compared to the Yaris FE driver seat model. It was observed that the Honda Accord FE seat was modeled in more details especially the seatback compared to the Yaris FE seat, and was thus used for this part of the study. THUMS was replaced with M50-OS because of computational efficiency. M50-OS is computationally more efficient than THUMS (runs in 2.5 hours for a 150 ms event on 40 processors compared to 24 hours for THUMS). As this part of

the study involved time intensive tasks (evaluating multiple human models in the same set up under different impacts, running multiple pre-simulations for adjusting the extremities and positioning the human model in the seat in different recline positions), the switch was made from THUMS to M50-OS.

Based on the lessons learned from the preliminary investigation (Part1), the Honda Accord FE driver seat model was updated i.e. the seat hinge was made rigid, head restraint was moved slightly forward to reduce the distance between the head restraint and the head, and integrated seatbelt was created. This updated seat model along with the M50-OS human model was used to evaluate occupant kinematics and injury metrics in a) different seatback recline positions, and b) two different carriage style seating configurations.

Reclined positions

Two different seatback recline angles, 20^o (driving position) and 45^o (relaxed position), were evaluated in both frontal and rear impacts. The crash pulse as shown in Figure 1 was used for all the simulations. Gravity simulations were carried out to position the human model in the seat. For seatback recline angle of 20^0, gravity was applied in Z but for seatback recline angle of 45^0, gravity was applied at 45^0 to properly settle the human model in the seat. The final settled positions are shown in Figure 5. The upper extremities of M50-OS were not modified from their default driving position in these simulations. After gravity simulations, belt creation and fitting was performed in ANSA [13].

(a) (b)

Figure 5. Final settled positions for seatback recline angle of a) 20^0, and b) 45^0

A total of four simulations were run (front and rear impact for each recline angle). The injury metrics i.e. HIC_{15}, BrIC and chest deflections were recorded for each simulation to investigate their trend as function of seatback recline angle.

Carriage style seating configurations

For this study, positioning of the human model in the seat was performed in two steps (Figure 6): a) the upper and lower extremities of the human model were adjusted from driving position to relaxed position, and b) this relaxed model was then settled in the seat using gravity simulation. Along with the gravity simulation, the lower extremities were further adjusted to position them as close to the seat as possible to account for the limited legroom in carriage style seating when all seats are occupied.

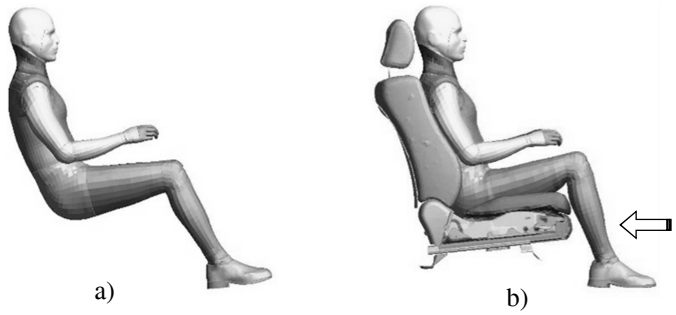

a) b)

Figure 6. a) Relaxed model, and b) Settled model with lower extremities positioned close to the seat

Carriage style seating was evaluated using two M50-OS human models. Two different configurations of the carriage style seating were investigated (Figure 7). In configuration 1, the occupants were positioned at 0^o (forward-facing, occupant-1) and 180^o (rear-facing, occupant-2) relative to the horizontal axis, whereas in configuration 2, the occupants were positioned at 0^o (forward-facing, occupant-1) and 200^o (rear-facing-oblique, occupant-2) relative to the horizontal axis. In both configurations, the seatback recline angle was 20^o.

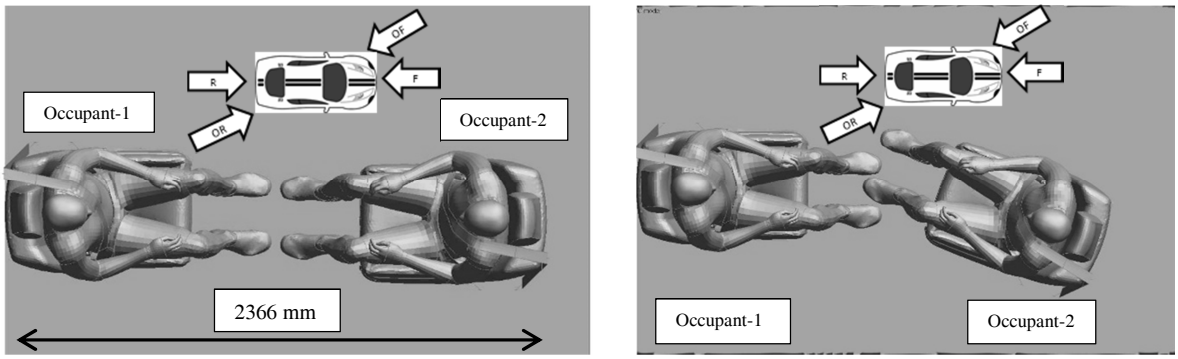

a) b)

Figure 7. Carriage style seating: a) configuration 1, and b) configuration 2

(*Impacts: **F**: Frontal, **OF**: Oblique-frontal, **R**: Rear, **OR**: Oblique-rear)

The two seats were positioned to keep the initial intersection between the feet of the occupants to a minimum. Such seat positioning resulted in the maximum distance of 2366 mm between the seatbacks (Figure 7a). Keeping no/minimal initial feet intersection between the occupants is reasonable since ADS equipped vehicles with carriage style seating are expected to have more legroom compared to the current mid-size sedans and intersection may not be required. For example, the wheelbase (which gives an idea about the size of the occupant compartment) for Mercedes-Benz F015 equipped with ADS [14] with carriage style seating is around 3610 mm compared to 2829 mm for 2018 Honda Accord [15]. This is almost 28% longer. The vehicle structure and its design might pose additional constraints on seating and will be considered in future studies. Four different impacts were simulated for each configuration (Figure 7) for a total of 8 simulations. Impacts simulated were a) frontal; b) oblique-frontal 20^o; c) rear, and d) oblique-rear 20^o. For all these simulations, the same crash pulse was used (Figure 1).

Part 3: Countermeasure Evaluation

The combination of seating orientation and impact direction that gave the highest BrIC value was identified from Part 2. The cause of high BrIC value was examined and a potential countermeasure was investigated. The high BrIC value was due to a high z-component of angular velocity. To counter this, the head restraint was redesigned. Morphing was performed using ANSA [13] to redesign the head restraint from a nearly flat to a curved shape as shown in Figure 8. This combination of seating orientation and impact direction was simulated again with the countermeasure in place, and the BrIC value was recorded.

Figure 8. Redesigned head restraint

RESULTS

Part 1: Preliminary investigation

The seatback rotation in the rear impact cadaver experiment that was performed using a 10g pulse (Delta-V of 15 mph) was between 30 - 35^{o}. The corresponding simulation showed similar seatback rotation of ~ 30^{o} as well (Figure 9).

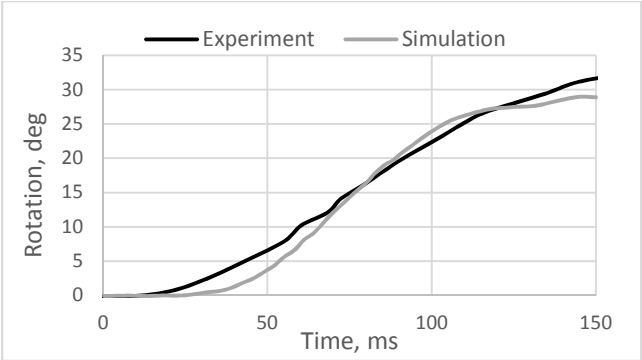

Figure 9. Seatback rotation comparison

The injury metrics observed in the 15 mph and 35 mph Delta-V simulations with a compliant and a rigid seat hinge are shown in Table 1. It can be observed that for both Delta-V's, injury metric values decreased considerably when seat hinge was made rigid. Chest deflection and BrIC were reduced by almost half whereas HIC_{15} was reduced by 15% for lower Delta-V (15 mph). At higher Delta-V (35 mph), the effect of a rigid seat hinge was more pronounced. Each injury metric was reduced at least in half.

Table 1. Injury metrics with compliant and rigid seat hinge

	Delta-V=15 mph			Delta-V=35 mph		
Seat hinge type	BrIC	HIC_{15}	Chest deflection (mm)	BrIC	HIC_{15}	Chest deflection (mm)
Compliant	0.58	92	28	1.85	3466	85
Rigid	0.28	78	15	0.93	490	36

Using a rigid seat hinge, the effect of changing the distance between the head restraint and the head was analyzed. The results are shown in Table 2. BrIC did not change much, however, chest deflection and HIC_{15} decreased by 14% and over 25% respectively.

Table 2. Injury metrics for various distances between head and head restraint

Distance between head-head restraint (mm)	BrIC	HIC_{15}	Chest deflection (mm)
45	0.93	490	36
1	0.90	357	31

Part 2

Reclined positions

The injury metrics for the two seatback recline angles of 20^{0} and 45^{0} in frontal and rear impacts are shown in Table 3. Chest deflection increased with increase in the seatback recline angle for frontal impacts but showed the opposite trend for rear impacts. However, the BrIC value increased with increase in the seatback recline angle for both rear and frontal impacts. HIC_{15} values were below 250 for all the cases except for the frontal impact in driving position (20^{0}), which had a very high HIC_{15} value (1106) due to the head contacting the knee.

Table 3. Injury metrics for various recline angles

	Frontal Impact			Rear Impact		
Recline angle	BrIC	HIC_{15}	Chest deflection (mm)	BrIC	HIC_{15}	Chest deflection (mm)
20^0	0.81	1106	38	0.22	145	21
45^0	0.88	236	44	0.42	166	18

Carriage style seating configurations

The injury metrics for each occupant in the two different seating configurations are presented in Figure 10. The arrows in Figure 10 show the direction of impact with respect to the vehicle (Figure 7). It can be observed that for each impact simulated in this study, the occupants in the carriage style seating experience completely different crash events. For example, an impact to the front of the vehicle causes the rear seat occupants (occupant 1) to experience frontal impact and front seat occupants (occupant 2) to experience rear impact. For clarity, the results are discussed in terms of the type of impact experienced by the occupant. The HIC_{15} value was below 300 for all the cases analyzed. In configuration 1, BrIC and chest deflection were the highest for both the occupants when experiencing oblique-frontal impact. In configuration 2, BrIC was highest for occupant 1 when experiencing frontal impact and for occupant 2 when experiencing oblique-rear impact, whereas chest deflection was highest for occupant 1 when experiencing frontal/oblique-frontal impacts and for occupant 2 when experiencing frontal impact.

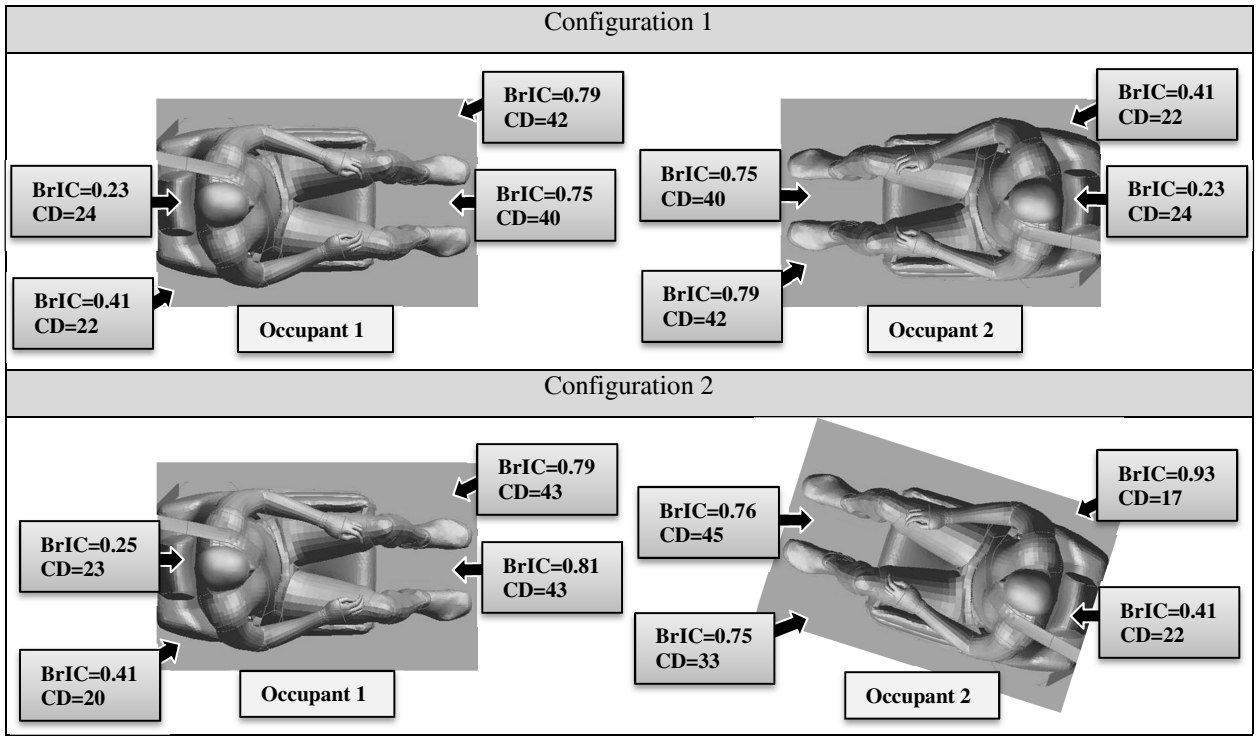

Figure 10. Injury metrics for carriage style seating

(*__CD__=Chest deflection (mm), *__Arrows__ shown indicate the direction of impact w.r.t the vehicle, Figure 7)

Part 3: Countermeasure Evaluation

Of all the seating orientations analyzed in the carriage style seating configurations, occupant 2 positioned at 200^o relative to the horizontal in configuration 2 demonstrated the highest BrIC value when experiencing oblique-rear impact (Figure 10). The BrIC values and angular velocities with and without the countermeasure (redesigned head restraint) are shown in Figure 11. It can be observed that the BrIC value reduced by a third with the redesigned head restraint. This reduction was obtained due to a significant decrease in the z-component of angular velocity.

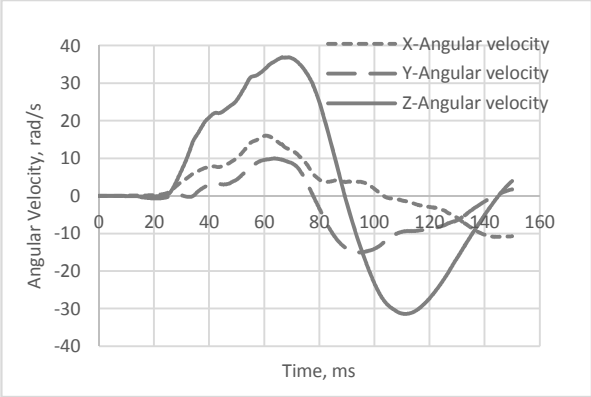

(a) BrIC=0.93

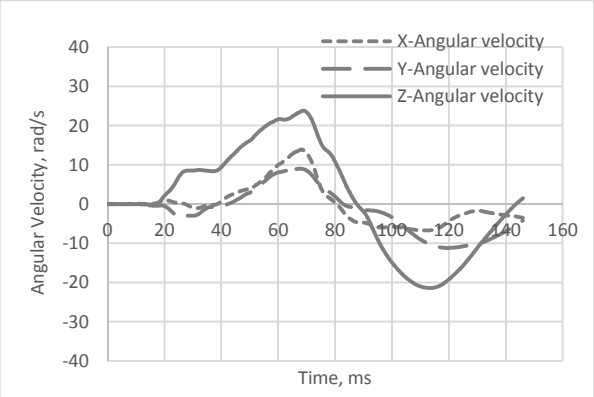

(b) BrIC =0.63

Figure 11. Angular velocities and BrIC with a) standard head restraint and b) redesigned head restraint

DISCUSSION

Rear impacts were evaluated using a Yaris FE driver seat model and the THUMS human model. Initially, only Yaris seat model was available to us and was thus used for this part of the study. Potential injury modes were identified from the low speed (Delta-V =15 mph) and high speed (Delta-V ~35 mph) rear impact simulations. It was observed that when the seat hinge was compliant, the rotation of the seatback allowed occupant ramping along the seatback. This ramping caused the head to whip back and hit/wrap around the head restraint (Figure A1 of Appendix A), which could cause serious head and neck injuries. Similar kinematics were observed in the low speed rear impact cadaver experiment as well where the compliant seat hinge allowed the cadaver to slide up the seatback causing the head to wrap around the head restraint. In this study, the vehicle structure was not considered but excessive ramping may cause the head to contact the car roof, which can also lead to serious head and neck injuries. In addition, the lower legs contacted the seat pan, which may cause tibia and fibula injuries. To mitigate the potential injury modes, the seat hinge was made rigid. It was observed that with a rigid seat hinge, the seat frame and cushion are forced to absorb more energy and as a result the occupant does not accumulate velocity and the ride down begins immediately (Figure A2 of Appendix A). All the injury metrics evaluated in his study were reduced when a rigid seat hinge was used (Table 1). It was also observed that a non-integrated seatbelt (coming from D-ring) does not provide much protection for the occupants in rear impacts. However, a seatbelt integrated with the seat can help mitigate potential injury risk by reducing the occupant ramping along the seatback by restraining the upper body with the shoulder belt. This is beneficial if the seat hinge is compliant. With a rigid seat hinge, the occupant ramping is not as much when the occupant is in the driving position (seatback recline angle of 20^0 to 25^0), however at higher seatback recline angles (45^0, 60^0), there may be significant ramping and integrated seatbelt can help reduce this ramping considerably. It was also observed that having an active head restraint (that can help minimize the distance between the head and the head restraint) in addition to a rigid seat hinge helps in reducing HIC (Table 2).

In this study, lower chest deflection was observed in rear impacts with a rigid seat hinge compared to a complaint seat hinge (Table 1). Yaris seat model was used for this study. Since this seat model was developed for frontal impacts, the seatback was not fully modeled. The seatback consists of just an outer frame on which the cushion is mounted with no supporting structure in the middle of the seatback (Figure 3). During simulations, it was observed that with a complaint seat hinge the upper body loaded the top of the seatback (due to occupant ramping) which is stiff due to the frame underneath whereas with a rigid seat hinge the upper body loaded the upper-middle to middle area of the seatback with no supporting structure behind it causing the seatback cushion to deform more. This may be the reason for lower chest deflections seen in this study with a rigid seat hinge. For rear impacts, stiffness of the seatback supporting structure is an important parameter that was not investigated in this study. This will be done as part of future work with newer FE seat models to better understand the relationship between seat hinge rigidity and chest deflection.

Simulations with higher seatback recline angle showed higher BrIC values for both frontal and rear impacts. It was observed that for frontal impacts, the x- and y-components of angular velocity were higher at higher seatback recline angles leading to higher values of BrIC, whereas for rear impacts, y- and z-components of angular velocity were

higher at higher seatback recline angles. The trend observed is based on limited number of simulations (two for each impact) and needs to be evaluated at more seatback recline angles.

For occupant 1, positioned at 0^o relative to the horizontal in both configurations 1 and 2 (Figure 10), there was a difference in the type of impact that had the highest BrIC value. Oblique-frontal impact had the highest BrIC value for occupant 1 in configuration 1 (0.79) compared to frontal impact for the same occupant in configuration 2 (0.81). This difference was due to the feet interaction between the occupants during impact. In configuration 1, since the occupants were positioned face to face with their feet aligned along the horizontal axis, there was feet interaction between them during impact where as in configuration 2 because of different seating orientations of the occupants, there was no feet interaction. The lack of interaction caused the feet of occupant 1 to contact the seat in front of it, thereby changing the kinematics. This change in kinematics caused the head to contact the knee during impact leading to higher BrIC value. The kinematics can be different for different set-ups.

Occupants, when experiencing frontal/oblique-frontal impacts (Figure 10), demonstrated BrIC values in the range from 0.75 to 0.81, and chest deflections in the range from 33 to 45 mm. The lowest chest deflection (33 mm) was for occupant 2 in configuration 2 because of high degree of obliqueness (40^o between the seating direction and impact direction). Occupants, when experiencing rear/oblique-rear impacts (Figure 10), demonstrated BrIC values in the range from 0.23 to 0.93 and chest deflections in the range from 17 to 24 mm. Again, occupant 2 in configuration 2 showed the lowest chest deflection (17 mm) because of high degree of obliqueness (40^o between the seating direction and impact direction). Chest deflection in frontal/oblique-frontal impacts is due to belt loading whereas in rear/oblique-rear impacts it is due to inertial loading. High degree of obliqueness between the seating direction and impact direction reduces the belt loading on the sternum in frontal impacts and the inertial loading on the seatback in rear impacts leading to lower chest deflection.

The BrIC and chest deflection values for occupants, when experiencing rear/oblique-rear impacts (Figure 10), are quite low. This is due to the rigid seat hinge used in the simulations. A complaint seat hinge would lead to much higher values for rear impacts (Table 1). The actual values here represent those measured by the simplified GHBMC model and are not directly translated to any ATD, i.e. if the chest deflection is about 45 mm, it doesn't mean that if a model of an ATD was used instead of the GHBMC, this value would've been the same.

It can be observed from Figure 10, that there are certain combinations of impact direction and seating orientation which are better than others in terms of BrIC. For occupant positioned at 0^0 or 180^0 relative to the horizontal and experiencing rear/oblique-rear impacts, the BrIC value is very low whereas for occupant positioned at 200^0 relative to the horizontal, the BrIC value is low when experiencing rear impact but very high when experiencing oblique-rear impact. The high degree of obliqueness between seating direction and impact direction causes substantial increase in the z-component of angular velocity, thus increasing the BrIC value. Similar results were observed in Kitagawa study [16], where higher degree of obliqueness gave higher BrIC values in rear impacts. Therefore, while high degree of obliqueness between the seating direction and impact direction reduces chest deflection, it increases BrIC.

Occupants seated in different orientation of the front seat (occupant 2 in configuration 1 and 2, Figure 10), when experiencing frontal/oblique-frontal impacts, did not show any clear trend for the chest deflections nor did they demonstrate any significant changes in the BrIC values. Thus, no seating orientation (180^0, 200^0) stood out as the safest in terms of injury metrics. However, when experiencing rear/oblique-rear impacts (Figure 10), occupant in seating orientation of 180^0 (occupant 2 in configuration 1) demonstrated substantially lower BrIC values compared to occupant in seating orientation of 200^0 (occupant 2 in configuration 2). Although the lowest chest deflection was observed for the occupant in seating orientation of 200^0, the considerable increase in BrIC value outweighs any advantages in terms of chest deflection for this seating orientation. In addition, the chest deflection values are relatively low for rear/oblique-rear impacts (17 to 24 mm) compared to the threshold of 63 mm [6] and may be irrelevant as a selection parameter when choosing safe seating orientation.

The highest value of BrIC obtained in this study was 0.93 for occupant 2 in configuration 2 experiencing oblique-rear impact (Figure 10). The potential countermeasure, modified head restraint, reduced the z- component of angular velocity by more than a third thereby reducing the BrIC value by almost a third as well to 0.63. Although the BrIC value reduced substantially with the countermeasure, occupants in seating orientations of 0^0 and 180^0 demonstrated lower BrIC value (0.41, Figure 10) when experiencing the same impact.

Limitations

- The results presented are limited to the occupant parameters (size, stature, gender) and restraint parameters (seatbelt) used in this study.
- Simulations were run in a sled type environment without any vehicle structure, which may pose additional constraints.
- Only head and chest injury metrics were considered.
- Crash pulse shape was not varied based on PDOF which may affect the results.
- The resultant crash pulse used in this study only considers the longitudinal and lateral components. The results may be different if rotational acceleration components are applied to the model.
- Results presented are based on limited number of simulations and impact types.
- Finally, any outcome from the models is only as good as the models themselves and experimental validation of the results is required, which may be carried out in the future.

Future work may also involve evaluating kinematics and injury metrics for the 50^{th} percentile male by changing the crash pulse, load limiter, occupant location relative to each other (move them closer); simulating carriage style seating configurations for 50^{th} percentile male at different seatback recline angles, and evaluating 5^{th} percentile female in similar scenarios.

CONCLUSIONS

The following observations were made from this study:

- Injury metrics for occupants in rear impacts sitting at various recline angles can be reduced by using:
  - Rigid seat hinge
  - Head restraint positioned close to the head
  - Integrated seatbelts
- Higher seatback recline angles lead to higher BrIC values for both frontal and rear impacts.
- For carriage style seating, occupant interaction during impact can affect the kinematics and hence the injury metrics.
- High degree of obliqueness between the seating direction and impact direction reduces chest deflection but increases BrIC.
- Seating orientations of 0^0 and 180^0 relative to horizontal may be safer for occupants in rear impacts.
- Redesigned head restraint (possible countermeasure) may be useful in reducing BrIC.

REFERENCES

[1] Taxonomy and Definitions for Terms Related to On-Road Motor Vehicle Automated Driving Systems. SAE Information Report (J3016)

[2] https://www.nhtsa.gov/sites/nhtsa.dot.gov/files/documents/13069a-ads2.0_090617_v9a_tag.pdf

[3] Jorlov, S., Bohman, K., Larsson, A. (2017). Seating Positions and Activities in Highly Automated Cars - A Qualitative Study of Future Automated Driving Scenarios. IRCOBI.

[4] The New Car Assessment Program Suggested Approaches for Future Program Enhancements (2007). DOT HS 810 698.

[5] Takhounts, E.G., Craig, M.J., Moorhouse, K., McFadden, J., Hasija, V. (2013) Development of brain injury criteria (BrIC). Stapp Car Crash Journal 57:243-66.

[6] Eppinger, R., Sun, E. et al. (1999) Development of Improved Injury Criteria for the Assessment of Advanced Automotive Restraint Systems – II, NHTSA, USA.

[7] Iwamoto, M., Nakahira, Y., Kimpara, H. (2015). Development and Validation of the Total HUman Model for Safety (THUMS) Toward Further Understanding of Occupant Injury Mechanisms in Precrash and During Crash. Traffic Injury Prevention, Volume16.

[8] Schwartz, D., Guleyupoglu, B., Koya, B., Stitzel, J.D., Gayzik, F.S. (2015) Development of a computationally efficient full human body finite element model. Traffic Injury Prevention.16 Suppl 1: S49-56.

[9] Reichert, R., Park, C-K., & Morgan, R. M. (2014). Development of integrated vehicle-occupant model for crashworthiness safety analysis (Report No. DOT HS 812 087). Washington, DC: National Highway Traffic Safety Administration.

[10] Singh, H., Ganesan, V., Davies, J., Paramasuwom, M., & Gradischnig. (2018). Vehicle interior and restraints modeling development of full vehicle finite element model including vehicle interior and occupant restraints

systems for occupant safety analysis using THOR dummies (Report No. DOT HS 812 545). Washington, DC: National Highway Traffic Safety Administration.
[11] LS-DYNA v.971. Livermore Software Technology Corporation.
[12] Kang, Y.S., Bolte, J.H., Moorhouse, K., Donnelly, B. (2012). Biomechanical Responses of PMHS in Moderate-Speed Rear Impacts and Development of Response Targets for Evaluating the Internal and External Biofidelity of ATDs. Stapp Car Crash Journal.
[13] ANSA, version 17.1.2, BETA CAE Systems.
[14] https://media.daimler.com/marsMediaSite/en/instance/ko/Overview-Mercedes-Benz-F-015-Luxury-in-Motion.xhtml?oid=9904624
[15] http://owners.honda.com/vehicles/information/2018/Accord-Sedan/specs#mid^CV2F5JJNW
[16] Kitagawa, Y., Hayashi, S., Yamada, K., Gotoh, M. (2017). Occupant Kinematics in Simulated Autonomous Driving Vehicle Collisions: Influence of Seating Position, Direction and Angle. Stapp Car Crash Journal.

APPENDIX A: OCCUPANT KINEMATICS

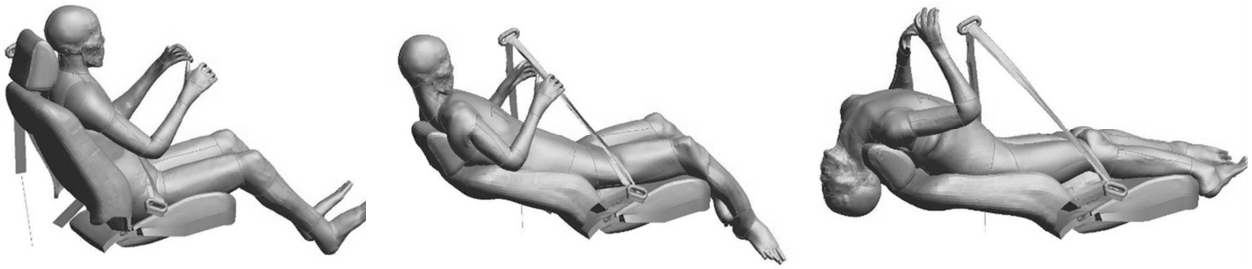

t=0 ms t=78ms t=135ms

Figure A1. Occupant kinematics in rear impact with a compliant seat hinge (Delta-V ~35 mph)

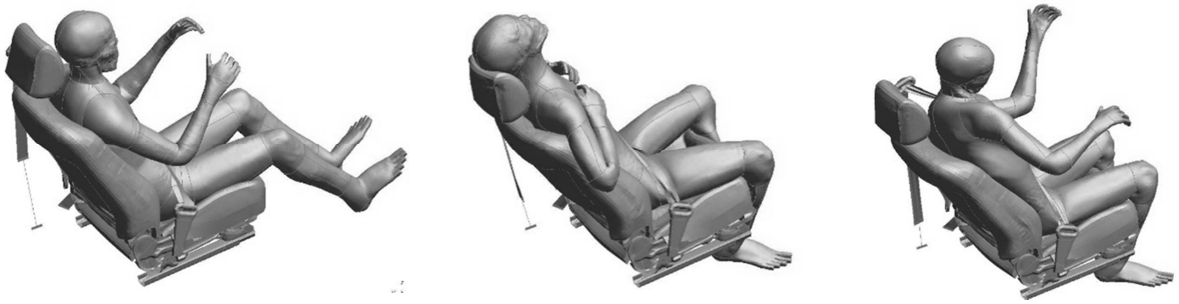

t=0 ms t=78ms t=135ms

Figure A2. Occupant kinematics in rear impact with a rigid seat hinge (Delta-V ~35 mph)

THE INFLUENCE OF RECLINED SEATING POSITIONS ON LUMBAR SPINE KINEMATICS AND LOADING IN FRONTAL IMPACT SCENARIOS

Dustin Draper
BMW AG, Ludwig-Maximilians-Universität, Germany
Andreas Huf
BMW AG, Germany
Philipp Wernicke
BMW AG, Germany
Steffen Peldschus
Ludwig-Maximilians-Universität, Germany

Paper Number 19-0062

ABSTRACT

With the advent of alternative seating positions in Highly Automated Vehicles, vehicle manufactures must take care to ensure the safety of new seating positions. The use of Human Body Models (HBMs) can aid in the use of analyzing these new concepts, as they closely represent a human being. HBMs are constructed with Finite Element (FE) modelled bones, muscles, and organs; whereas crash test dummies are made of foams, rubbers, and metallic structures. Due to these differences. HBMs show a different response compared to traditional crash test dummies. A sensitivity study on spinal posture using the THUMS v5 was performed using a BMW prototype reclined concept seat. By changing the initial of the posture of the lumbar spine, changes in spinal kinematics as well as varying force responses were observed during a frontal load case. This type of study could not be conducted with a crash test dummy as the spine of standard front crash dummies does not easily allow for postural changes. These variations suggest that initial spinal posture plays a role in the overall spinal kinematic response as well as the amount of force seen transmitted through the spine.

INTRODUCTION

As driver assistance systems become more advanced, the possibility that the occupants of vehicles will be able to focus on other tasks besides driving also is becoming more probable. Studies have shown that in cars with higher levels of automation passengers expect to be offered non-traditional seating arrangements [1]. In their *A Vision for Safety 2.0* document, NHSTA has stated that care should be taken to ensure that new non-traditional seating positions are safe for vehicle occupants, and that this evaluation might be made using simulation tools such as HBMs, in addition to the hardware tests which are the current standard [2]. In hardware tests all vehicles are tested according to a predefined protocol; in new seating positions this might not be possible. It is also likely that occupant kinematics in new seating positions will be sufficiently different to traditional seating positions that it would approach the limits of hardware dummy validity. Simulations using HBMs are a good candidate for this type of evaluation because their flexibility allows them to be used in many different configurations.

Traditional automotive safety standards have been adopted in accordance with what has been observed in the field, with the emphasis that predefined crash tests will cover a number of real world accident scenarios. This has been possible through the use of accident analysis which shows which kinds of crashes have a higher risk of injury and are the most prevalent [3].

Based on previous simulation studies of various future seating concepts a series of hardware tests were carried out at BMW to closer investigate a seat in a so called Zero-G reclined position [4]. From this study it was observed that the dummies exhibit a different kinematic chain in the reclined position than they do in the traditional upright position, which can be seen in Figure 1. Other studies have also shown non-standard kinematics in non-standard seating positions [5].

Figure 1: Dummy kinematics comparison: conventional seating configuration, above, and the prototype reclined configuration below, from [4].

The difference in kinematics was especially seen to have a large influence on the forces experienced by the lumbar spine sensors in the dummies. This is an indication that the lumbar spine should be more closely investigated. An investigation with a human body model was undertaken in an attempt to get the most realistic assessment of what happens to the spine during a frontal reclined crash, as the HBM spine more closely resembles that of an actual occupant than the spine of a crash test dummy, as seen in Figure 2.

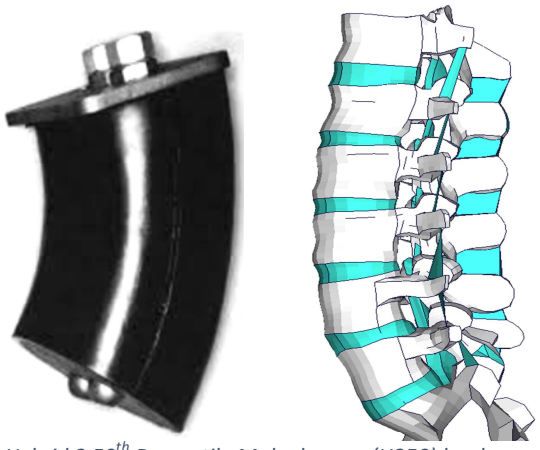

Figure 2: Comparison between a Hybrid 3 50th Percentile Male dummy (H350) lumbar spine [11] (left) and a HBM lumbar spine (right).

METHOD

The human body model chosen for this study was the THUMS v5 50th percentile Male. A preliminary simulation series was run in order to validate the simulation model of the seat with the hardware prototype seat using a H350 dummy.

The THUMS model was positioned first in a comparable manner to the H350 dummy which was used for the seat validation, but this position was ultimately found to be inadequate, because the H350 was not designed to be reclined. It is too stiff in some key areas relating to positioning, most notably resulting in a large gap between the head and the headrest. A second position was therefore derived combining two separate data sources. The first source of data is a set of anatomical landmarks found by probing a 50th percentile male occupant sitting in the seat using a Faro Arm. The second source was an Upright Magnetic Resonance Imaging (MRI) dataset from a different 50th

percentile male used to estimate the angles associated with the lumbar spine in a reclined seat. These two sets of data complement one another: one for the superficial surface and one for the internal spinal geometry. A comparison between the MRI data and the positioned human body model can be seen in Figure 3.

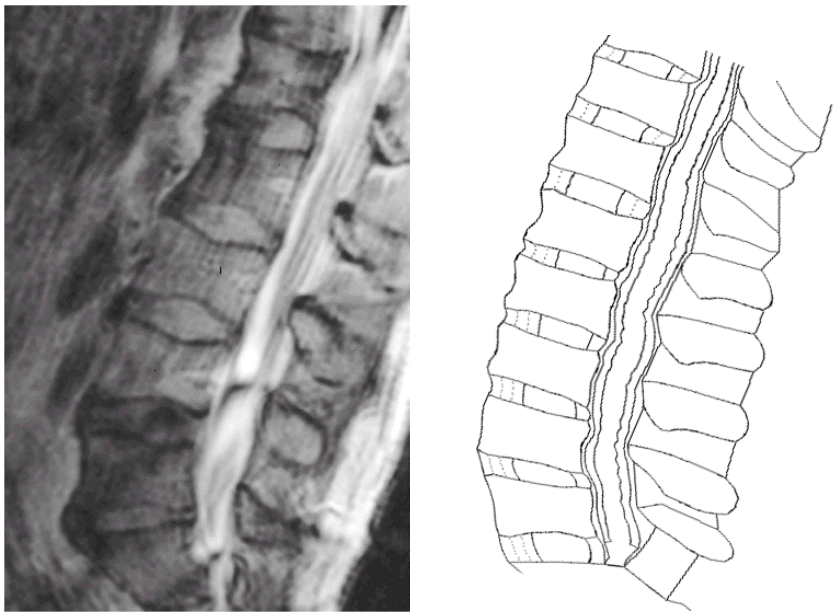

Figure 3: Lumbar spine position as measured using an Upright MRI, and the positioned THUMS 5 lumbar spine.

After the H350-based position was compared with the MRI based position it was found that there was a difference in peak lumbar spine forces, and that the models exhibited differing spinal and global kinematics, as well as different lumbar spine force responses. The differences between the H350-based and the MRI-based models can be seen in Figure 4.

A sensitivity study was then performed using the model with the MRI based seating position as a baseline. For the sensitivity study the pelvis angle and the lumbar spine curvature were varied to see how small changes in the lumbar spine posture affect the kinematics and force response in a frontal crash scenario. This positioning was performed using the Piper positioning tool [6]. Spinal rotation centers were defined in all of the intervertebral disks between the sacrum and T12. The pre-positioning module was then used to vary the spinal position with all bones being held fixed except for the pelvis, sacrum, and the lumbar spine. Then, a prescribed angle was given to all of the rotation centers and the lumbar spine was made to bend. After positioning in the pre-positioner module, the nodes were exported to a standard pre-processor, and smoothing operations were performed. The original position and the modified positions can be seen in Figure 4. Two positions were investigated, one where rotations were prescribed to make the initial geometry more lordodic, extended to be more like an s-curve, and one where the initial position was more kyphotic, or flexed like a c-curve. The more kyphotic state does not exhibit a pure kyphosis, but more so than the baseline position. This type of investigation could only be performed using a HBM: changing the spinal position of a dummy would either not be physically possible (i.e. H350 has no movable lumbar spine joints) or would result in a global change of position, with no possibility to isolate only the spine.

The new models were then run under the same boundary conditions as the MRI-based position model, with the same pulse, and the same restraint system.

RESULTS

Positioning

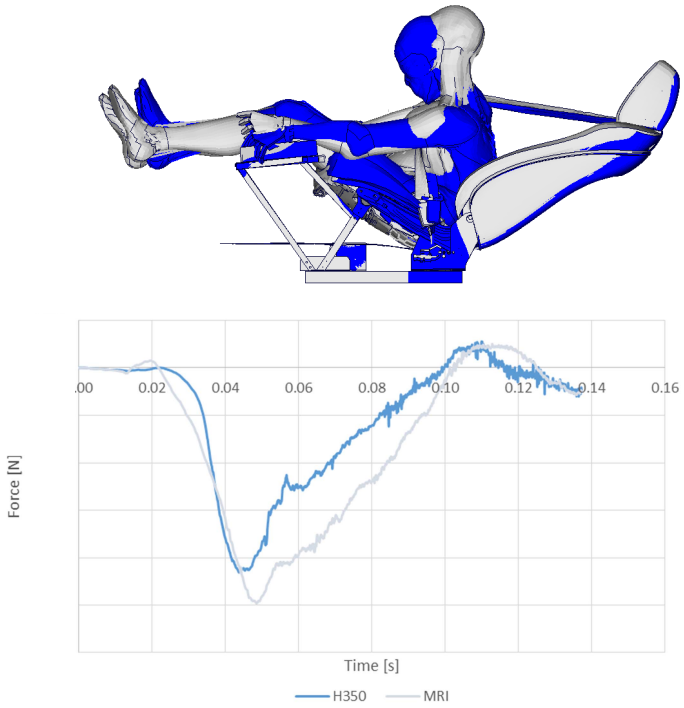

Figure 4: Differences between the H350-like positioned model, in blue, and the MRI-based positioned model, in grey. Forces are measured in the L5 vertebrae.

In Figure 4 large kinematic differences can be seen between the two original HBM positions, as well as a large difference in the peak force observed and the force development profile.

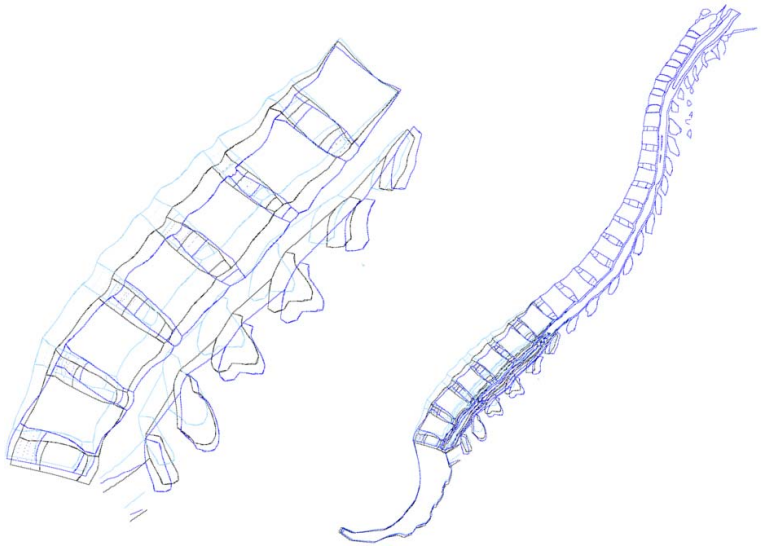

Figure 5: Model orientation after postural positioning, black is the original MRI based position, dark blue is the more kyphotic position, and light blue is the more lordotic position. Left is the lumbar spine where model differences can be easily identified. On the right hand side it can be seen that all the models have the same positioning in the cervical and thoracic spine.

After the postural positioning the two models had only minor differences. In Figure 5 one can see that the light blue and black colorations of the lordotic and baseline models, respectively, are only visible in the lumbar spine and

surrounding soft tissue, in the upper body and lower extremities the models exhibit no visible differences, as the dark blue of the kyphotic position is overlaid on the topmost layer in the graphic.

Force Response

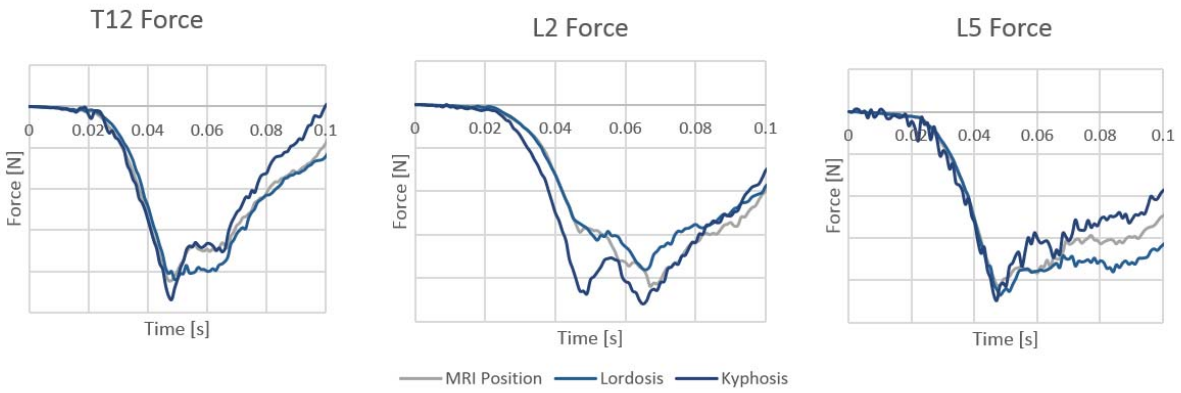

Figure 4: Force histories in selected thoracolumbar vertebra. MRI initial position seen in grey, the more lordodic position in light blue and the more kyphotic position in dark blue. Loading of the T12 and L5 vertebra are consistent across all configurations, whereas no trends hold true for unloading for of the states.

The first thing to note is that the peak force measured in the HBM is much lower than that measured in the dummy. In the HBM H350-like position, the forces are less than 60% of the peak force seen in the hardware tests. In the force time histories of the various postures as seen in Figure 6, one can see differences in the peak force values as well as in the general curve development, though the differences are not consistent across the spinal levels. In general the kyphotic case has the highest peak force, the lordotic case the lowest peak force, and the MRI-based position, a force level somewhere in between.

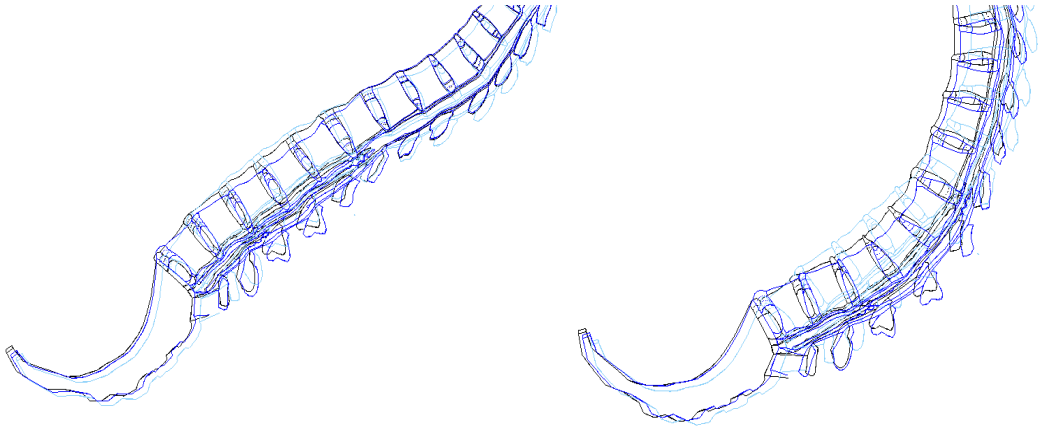

Figure 7: Spinal position at 50ms after the onset of the pulse left and 100ms after the onset of the pulse, right. Black is the original MRI based position, dark blue is the more lordotic initial position and light blue is the more kyphotic initial position.

Kinematics

The kinematics of the lumbar spine remain relatively consistent between the MRI-based and the more lordotic positions, but the kinematics of the more kyphotic position does not follow the same chain. The locations of the pelvis in each position are also quite divergent, and the position of the thoracic spine also shows a large disparity

between the positions especially for the more kyphotic position. All of these differences can be seen in Figure 7. Head kinematics appear to be relatively stable between positions, as seen in Figure 9.

DISCUSSION

Positioning

During the initial positioning using the Upright MRI and Faro arm data, a discrepancy between the model lumbar spine and the lumbar spine which was used to generate the MRI data was observed. It would have been impossible to position the model into alignment with all aspects seen from the MRI: either the positions of the vertebral bodies could be aligned by changing the pelvis rotation, or the observed disk angles could be made the same with the pelvis rotation being kept in the initial state. This is because the subject of the MRI has a different spinal geometry than that which is found in the THUMS HBM. The second approach was the one which was chosen: the pelvis was held fixed and the relative vertebral body angles were used as targets. In the MRI scan, the position was achieved using rigid foam blocks which were very dissimilar to the actual prototype seat. The Faro arm data on the other hand was taken using the prototype seat itself. Due to this it was decided that the pelvic angle should be used from the data were there was a higher confidence in its accuracy in the context of a real world setting. The MRI data was then incorporated in the form of the disk relative angles, starting from the sacrum. Another challenge associated with this position is that the MRI images, and what was measured in the ergonomics lab were two different subjects, whose spines are presumably different. But there is no way to know how different, as the MRI data was gathered as part of a different and separate study by the Ludwig-Maximilians-University in Munich. The study used a seating geometry designed to mimic a reclined position, but this geometry was different than the protype seat currently being studied, which means there are differences in the positioning. Any differences in positioning are also only part of the difference: differences in material properties, and age can also play a role, one which cannot be easily investigated with the present tools and methods.

The spinal rotation is achieved using the Piper positioning tool [6], using kinematic rotation centers defined at the disk center. The Piper approach is used because it allows for changes in the disk shape without causing any bulging that might result from a simulation based positioning process. Another added benefit of the Piper framework is that because the postural changes were localized, the soft tissue changes were also only seen the lumbar region, making the subsequent simulation more stable. The positioning resulted two separate initial postures, each chosen to be on either side of the baseline position. For the lordosis case the lumbar lordosis angle as measured from the top of L1 to the bottom of L5 as defined by Sato [7] was increased by 10°. The Pelvic angle as measured from the vertical to the line between the ASIS and the pubic symphysis [8] was decreased by 1.5°. Both of these changes fall within the range of normal physiological variation according to studies performed by Izumiyama [9], although the authors note that subjects fell into groups of spinal posture and so it can be assumed that the transfer from one posture to the other is likely not physiologically feasible. The kyphotic position saw a change in the lumbar lordosis of -15°, which is a large amount of variation, but yields a position, which is close to the mean values reported by Izumiyama [9]. The pelvic angle for the more kyphotic posture is almost the same as that of the lordodic posture: and both are lower than the pelvic angle of the baseline. This is likely an artifact of the positioning process, where artificial forces are applied to move the spine which resists with an artificial stiffness. It is likely that the kyphotic spine generated enough force to overcompensate the motion of the pelvis, pulling it the opposite way of what was prescribed.

Force Response

It was noted that the in HBM H350-like position, the forces are less than 60% of the peak force seen in the hardware tests. This is in part due to the positioning used to bring the HBM to match some of the H350 landmarks, does not match the reality of how an occupant would sit in the reclined seat. With the head lifted off of the headrest less axial forces are generated in the spine from the inertia of the head moving forward. This difference of position accounts for less than 10% of the difference in the peak force: the MRI based force response as seen in Figure 4 has a higher peak force than the H350-like position, but is still substantially lower to the forces seen in the dummies. Comparing forces measured in the dummies to forces measured in the HBM should also be done cautiously. The models have different geometries, so forces cannot be measured at exactly the same locations across models. These differences in geometry, as well as the use of materials with different stiffness moduli across models, also has an effect on the magnitude of these forces.

Comparing the forces across postures for the same HBM, as seen in Figure 6, the maximum force occurs when the pelvis is fully coupled with the seat. All configurations are seen to have a similar response for forces measured in the

T12 and L5 vertebrae. The kyphotic configuration for the force measured in the L2 vertebra shows a different response than the others with a faster ramp up to peak force, a higher peak force overall, and a double peaked curve behavior. The kinematics in the thoracic spine, as seen by comparing Figures 5 & 7, no longer have any overlap, which holds for all positions. The initial differences in pelvic position propagate, and causes similar changes in displacement and rotation then goes up the kinematic chain into the lumbar spine and the thoracic spine. Head position remains fairly consistent, as seen in Figure 9, likely due to inertial effects and the low relative stiffness in the cervical spine.

It can be seen for all of the various levels in Figure 6, that the peak force is influenced by the initial posture. At the L2, which experienced the largest influence due to the positions; the more lordotic posture had an 8% smaller peak force as compared to the MRI positioned posture, and the more kyphotic posture had a 9% larger peak force. Also at the L2 level, but not for the other levels plotted, the loading curve is significantly different for the more kyphotic posture: it experiences a double peak. The MRI position and more lordotic position both also have a small quasi peak at the same time, but they are more of a slight plateauing than a fully defined peak. At the time of the first peak the pelvis experiences maximum forward excursion before it begins to rotate. The more kyphotic posture experiences a larger force at this point because it has almost no curvature and can therefore maintain its position without deforming. The MRI position and the more lordotic position both have some curvature at this time, so they deform more easily, which doesn't allow the force peak to develop. Given this spread in forces, it is conceivable that there is a posture which exhibits the highest force for a given seating configuration. If future injury criteria are based on the force transmitted, then this posture should be the one which is always evaluated.

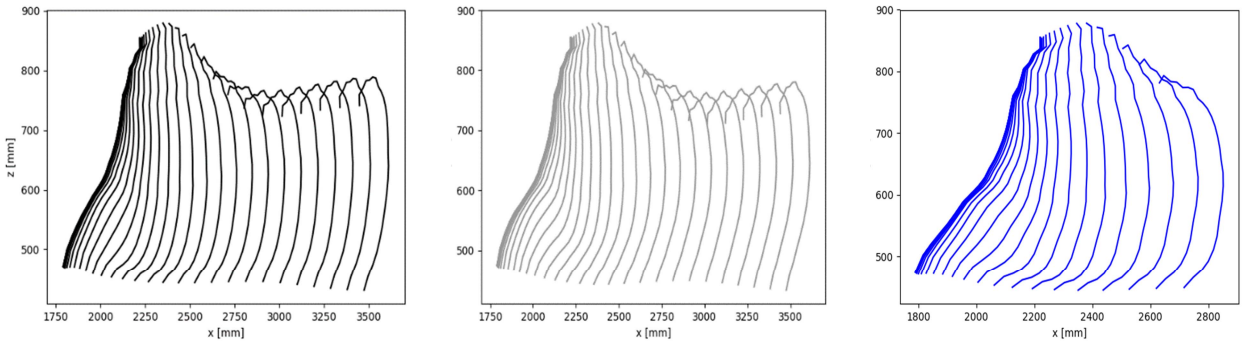

Figure 7: Global spinal kinematic time histories, black is the MRI position, grey is the more lordotic position, and blue is the more kyphotic position.

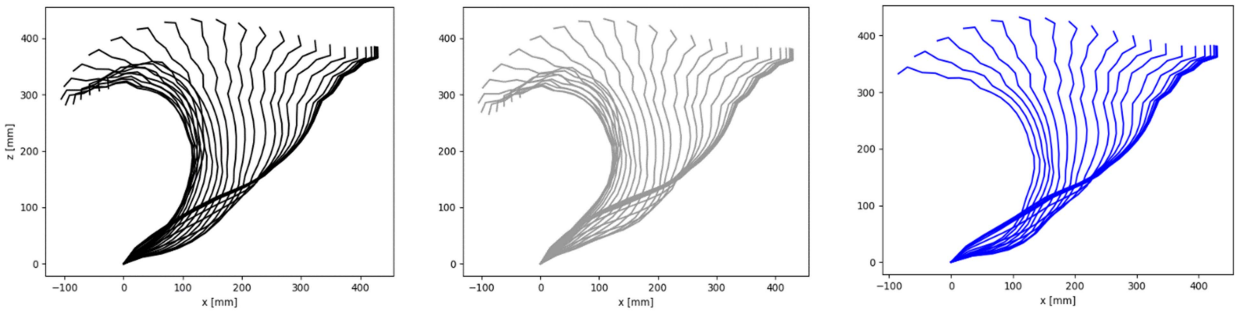

Figure 8: Relative spinal kinematics with the view fixed about the sacrum, black is MRI position, grey is the more lordotic position and blue is the more kyphotic position.

Kinematics

During the loading phase initial posture effects can be seen in the kinematic development of spinal motion. The MRI based position shows an initial instability during the early phase of the crash where the spine goes quickly into flexion around the L3 level. This can be seen in Figure 7, where the black plot can be seen to develop a curvature in the lower left corner. The lordodic initial position on the other hand, shown in grey in Figure 7, exhibits no such instabilities. In Figure 8 this can be seen in the location of inflection in the lower right of the respective subfigures: for the lordotic case the inflection is milder and occurs higher up the spine than is the case for the baseline. This instability immunity is because the lordotic case has more room to deform before it reaches the bifurcation point. One might think of this as a pendulum, where the MRI case is closer to the middle of the pendulum, and ends of crossing to the other side, and the lordosis case is further from the middle, and so never reaches the other side.

The more kyphotic case shows a different response. Towards the bottom of the blue subplot in Figure 8 one can see that the curves run almost horizontally. This leads eventually to an inflection point which is further left than the MRI position shown in black. This tighter, further forward inflection might be due to straighter spinal alignment, which is also seen in the higher force response and steeper ramp up that the kyphotic variant has in the L2 plot in Figure 6.

Also of note is that this local instability has very little effect on the global behavior. This can be seen in the overlay plot in Figure 9: all three models are visible, meaning there is some difference, but the composite result still looks like a coherent model, showing the differences to be small. This means that the head and other global kinematics are insulated from lumbar spine effects. One cannot speculate if this will hold for more pronounced lumbar spine positions, and this should be further investigated.

What can also be seen in Figure 9 is the differences realized between a traditional dummy and the HBM in the reclined seating position. The dummy sits much more upright at the point of maximum excursion as its spine does not allow for bending in the thoracolumbar region. This can be clearly seen in the dummy's very straight back as seen in the figure. Also related to the HBM's more flexible spine changes in the lateral position of the HBM, but not in the dummy. Being less flexible means that the dummy torso bends forward as a complete unit, whereas the HBM wraps around the belt causing a difference between the left and right sides of its torso.

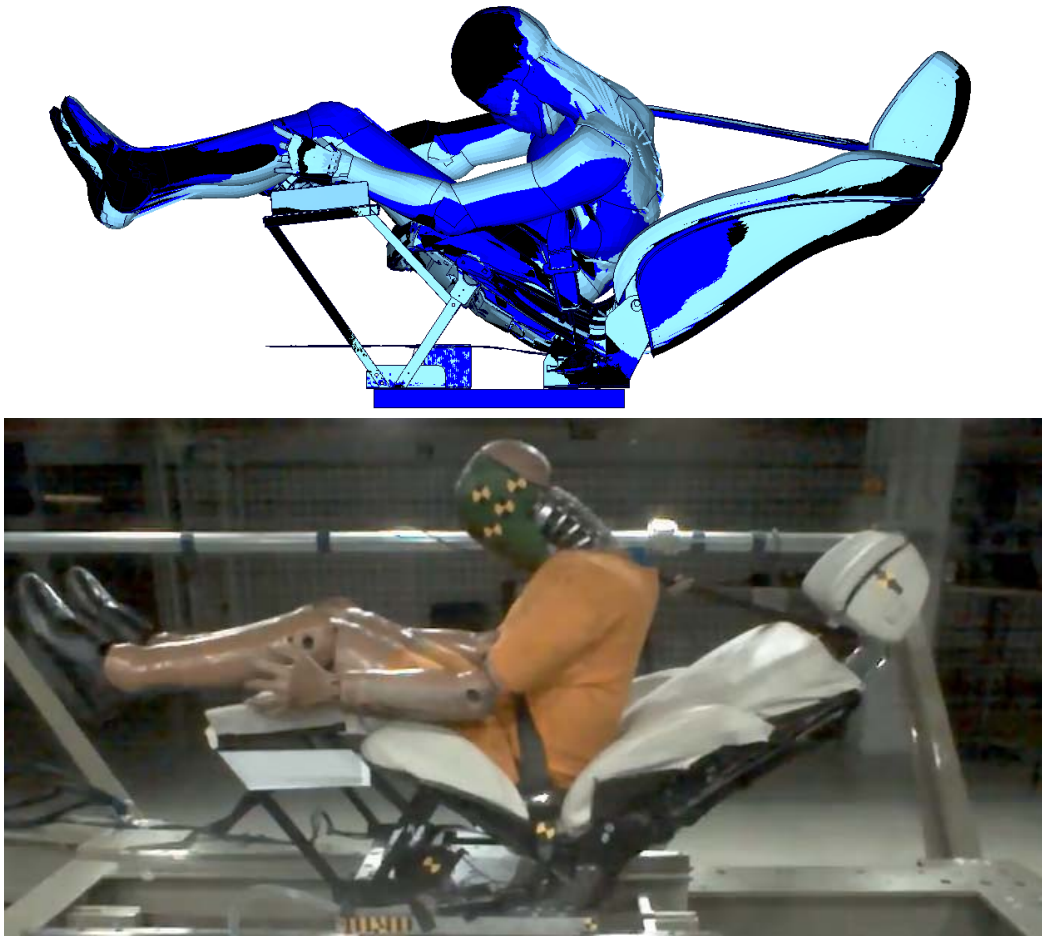

Figure 9: Comparison of global kinematics 100ms after the onset of the pulse. In the upper image are the FE simulations, with the MRI positioned model in black, the more lordotic model in dark blue and the more kyphotic model in light blue. In the lower image is the hardware test of a H350 dummy at 100ms after the onset of the pulse from [4].

Validity

These various results beg the question, what happens in actual humans who have varying spinal geometries? This is a difficult question to answer. The validity of human body models have been improving, but there are still large gaps of validity. One such gap has to do with the spine. As of now, no published studies exist with which to explicitly validate human body models in a reclined seating configuration, with respect to their spines. The spine is difficult to validate as tracking it is difficult. It is also difficult to measure the forces transmitted through the spine. In this simulation series the disks were compressed beyond the physiological levels observed in non-injurious tests [10], but there is a lack of data to say where the level of injury starts. The human body models themselves are also not validated in these regions and in these modes of excitement. Even with newly defined allowable safe levels of force, experiments are still needed to see if what the models predict matches the reality fot actual occupants. This study also shows that posture has an influence in HBM simulations, but the actual range of postures in a reclined seating concepts is currently unknown, and there is no best practice for measuring the spinal position to the accuracy needed to validate HBM simulations. There is a similar story for any sort of safety criteria. More research is required from governing bodies and original equipment manufacturers in order to define and harmonize safety standards.

CONCLUSIONS

The kinematic response of the Human Body Model simulation is very different to the response of the dummies in the reclined position. The HBM kinematic looks more realistic than the crash test dummies, as can be seen in how its spinal curvature develops in the HBM, as opposed to the permanently straight-backed dummy. However, there is no way to objectively evaluate how realistic current HBMs are in this kind of positions. The HBMs also experienced notably smaller forces in the lumbar than the dummies, of which only a small part can be attributed to difference in position. By making small changes to the initial spinal posture of an HBM sitting in a reclined seating configuration, changes of up to 9% were observed in the subsequent spinal kinematics and peak force response. As these changes were small, it is possible that larger changes will have larger effects. These postural changes have no analog in dummy testing, due to how dummies are constructed, and as such can only be investigated using HBMs.

Further work

The next steps to be undertaken should involve looking into larger changes in posture, as larger changes could result in still further divergent kinematics as to what has already been observed. Another area of exploration would be to investigate if one posture or group of postures experiences higher forces, or divergent kinematics, which might require special attention, i.e. the definition of a worst case scenario posture. As changes in posture were shown to have effects on kinematics and force response, validation experiments in the future should also consider and, if at all possible, measure and document initial spinal posture. In order to establish how accurate the HBM models are, more validation experiments are needed. The overall validity of HBMs in reclined positions should also be more closely investigated, which would require that more experiments designed to improve HBM validity in these new seating positions.

1. Sofia Jorlöv, et al. 2017. "Seating Positions and Activities in Highly Automated Cars– A Qualitative Study of Future Automated Driving Scenarios." Proceedings of IRCOBI

2. National Highway Traffic Safety Administration. 2017 "Automated Driving Systems 2.0: A Vision for Safety."

   <https://www.nhtsa.gov/sites/nhtsa.dot.gov/files/documents/13069a-ads2.0_090617_v9a_tag.pdf>

3. Sherwood, C. et al. 2009. “Characteristics of Small Overlap Crashes” Proceedings of the 21st ESV Conference,

4. Huf, A. et al. 2018. “Development of Occupant Restraint Systems for Future Seating Positions in Fully of Semi Autonomous Vehicles.” Proceedings of Airbag Conference

5. Östling, M. et al. 2018. “Driver Behaviour in Automated Vehicles and Effects on Safety – A Swedish and Chinese Perspective: How do we Save More Lives in the Future?” Proceedings of VDI Safety Systems

6. Beillas, Philippe, et al. 2015. "Specifications of a Software Framework to Position and Personalise Human Body Models." Proceedings of IRCOBI

7. Sato, F. et al. 2015. “Analysis of the alignment of whole spine in automotive seated and supine posture using an upright open MRI system.” Proceedings of JSAE Annual Congress

8. Kyo, T. et al. 2013. “Factors predicting change in pelvic posterior tilt after THA.” Orthopedics

9. Izumiyama, T. et al. 2018. “The Analysis of an Individual Difference in Human Skeletal Alignment in in Seated Posture and Occupant Behavior Using HBMs ” Proceedings of IRCOBI

10. Newell, Nicolas, et al. 2017. "Strain Rate Dependence of Internal Pressure and External Bulge in Human Intervertebral Discs during Axial Compression." Proceedings of IRCOBI

11. Foster, J. et al. 1977. "Hybrid III—A Biomechanically-based Crash Test Dummy." SAE Transactions,